NUMERICAL MODEL OF A TENSIONER SYSTEM AND FLEX JOINT

A Thesis

by

HAN HUANG

Submitted to the Office of Graduate Studies of
Texas A&M University
in partial fulfillment of the requirements for the degree of

MASTER OF SCIENCE

Chair of Committee,	Jun Zhang
Committee Members,	Scott Socolofsky
	Joseph E. Pasciak
Head of Department,	Robin Authenrieth

May 2013

Major Subject: Ocean Engineering

ABSTRACT

Top Tensioned Riser (TTR) and Steel Catenary Riser (SCR) are often used in a floating oil/gas production system deployed in deep water for oil transport. This study focuses on the improvements to the existing numerical code, known as CABLE3D, to allow for static and dynamic simulation of a TTR connected to a floating structure through a tensioner system or buoyancy can, and a SCR connected to a floating structure through a flex joint. A tensioner system usually consists of three to four cylindrical tensioners. Although the stiffness of individual tensioner is assumed to be linear, the resultant stiffness of a tensioner system may be nonlinear. The vertical friction at a riser guide is neglected assuming a roller is installed there. Near the water surface, a TTR is forced to move due to the motion of the upper deck of a floating structure as well as related riser guides. Using the up-dated CABLE3D, the dynamic simulation of TTRs will be made to reveal their motion, tension, and bending moment, which is important for the design. A flex joint is approximated by a rotational spring with linear stiffness, which is used as a connection between a SCR and a floating structure or a connection between a TTR and the sea floor. The improved CABLE3D will be integrated into a numerical code, known as COUPLE, for the simulation of the dynamic interaction among the hull of a floating structure, such as SPAR or TLP, its mooring system and riser system under the impact of wind, current and waves. To demonstrate the application of the improved CABLE3D and its integration with COUPLE, the related simulation is made for ‘Constitution’ SPAR under the met-ocean conditions of hurricane ‘Ike’. The mooring system of the Spar consists of nine mooring lines and the riser system consists of six TTRs and two SCRs.

ACKNOWLEDGEMENTS

I would like thank my committee chair, Prof. Jun Zhang, for his guidance and kindly support throughout my research. I would as well like to thank my committee members, Prof. Scott Socolofsky and Prof. Joseph E. Pasciak for their help during my research. I would also like to express my thanks to Dr. Shan Shi who also provided kind help to me about industry experience. I also want to extend my gratitude to Liyun Zhu and Tiancong Hou for providing details of 'Constitution' Spar and flex joint models.

Thanks to my friends and colleagues and the department faculty and staff for making my time at Texas A&M University a great experience.

Finally, thanks to my mother and father for their encouragements and supports through my study in United States.

TABLE OF CONTENTS

Page

LIST OF FIGURES

LIST OF TABLES

TABLE Page

1. INTRODUCTION

1. 1 Background and Significance

Many platforms have been designed and used for production of oil and gas in the Gulf of Mexico (GoM) since 1940s. The tremendous fast development of offshore construction can be observed for a large variety of activities at sea. Different types of offshore platforms are being proposed for better performance as oil and gas exploration is pushed into deeper and deeper water (Murray *et al.* 2007).

On floating host platforms, dry-tree system is constructed to facilitate tieback of the subsea manifolds, via TTRs, to a dry environment on the vessel to minimize the construction and production costs (Murray *et al.* 2006). The top tension of a TTR is provided by either a buoyancy can or a deck mounted tensioner systems, such as hydropneumatic tensioner (Yang and Kim 2010). Both types of TTR are used in various kinds of platforms, including tension leg platforms (TLPs), semi-submersible and Spars.

On a TLP, TTR with a tensioner system is more widely utilized. Whilst on a Spar deployed in moderate-depth water, a TTR with a buoyancy can is more popular. In this case, buoyancy cans are to provide tension at the top of production and drilling risers. A TTR with a buoyancy can does not impose vertical loads on the Spar hull and its vertical movements is independent of the hull motion (Chen *et al.* 2008). However for Spars that are constructed at ultra-deep water depth, which is more than 1500 meters, disadvantages of TTR of this kind begin to emerge to form many practical problems. As water depth goes deeper, the volume of a buoyancy can will become larger due to the increasing net weight of the TTR. Due to the limitations of center well space and Spar hull volume, the buoyancy cans might not be feasible choice under the ultra-deep water circumstance (Chen *et al.* 2008).

Since technology in tensioners has advanced significantly these years, tensioners show greater advantages compared to buoyancy cans especially for ultra-deep water conditions. Though tensioners do not have negative effects on the center well and Spar hull size, they will exert tension loads on the entire floating structure and may have a functional constraint since all tensioner systems have stroke limitations (Chen *et al.* 2008). Despite of these challenges, it has been demonstrated that the cost implication of Spars from tensioners due to extra tension loads and stroke limitations would be far less than that from buoyancy cans in ultra-deep water situations. Advances in tensioner technology enable larger stroke requirements, hence TTRs with tensioner system are gaining increasingly popularity in real-world applications these years. Above all, the global performance analysis of TTRs of such type is of great significance to both fundamental research and industry applications.

Turning to the steel catenary riser (SCR), it is always connected to the hull through the connection of flex joint (See Fig. 1.1). The flex joint will exert bending moment on the upper end of SCR. However, in most previous researches, the connection point between SCR and hull was assumed to be a hinge. The calculations can be simplified following this approach, but there will be some discrepancy with the actual conditions if the connection point is assumed to be a hinge. Therefore, the specific model of flex joint is of great significance for a comprehensive analysis of SCR.

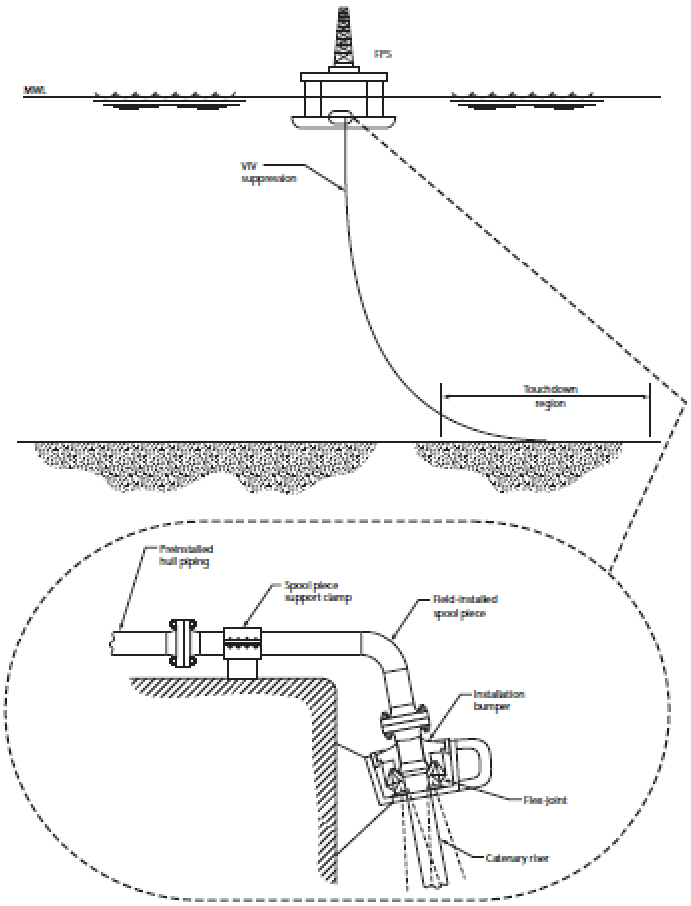

Fig. 1.1 Configuration of flex joint (API RP 2RD)

Therefore, several improvements will be made to the existing numerical code, known as CABLE3D, to allow for static and dynamic simulation of a TTR connected to a floating structure through a tensioner system or buoyancy can, and a SCR connected to a floating structure through a flex joint. The improved CABLE3D will be integrated into a numerical code, known as COUPLE, for the simulation of the dynamic interaction among the hull of a floating structure, such as SPAR or TLP, its mooring system and riser system under the impact of wind, current and waves.

1. 2 Review of Previous Work

Chen and Nurtjahyo (2004) introduced a “Linearized P-Delta” model to account for the effects of buoyancy can TTR on the Spar motions. The predicted motions using the proposed model were compared with the model test results for a production truss Spar in the Gulf of Mexico. There are two types of tensioner system: tension style and compression style respectively (See Fig. 1.2). In most compression style tensioner system, cylinders are parallel with each other and the compressed air inside cylinders provides the top tension needed by risers, therefore the whole compression style tensioner system could be modeled as one individual linear or nonlinear spring (Chen *et al.* 2008).

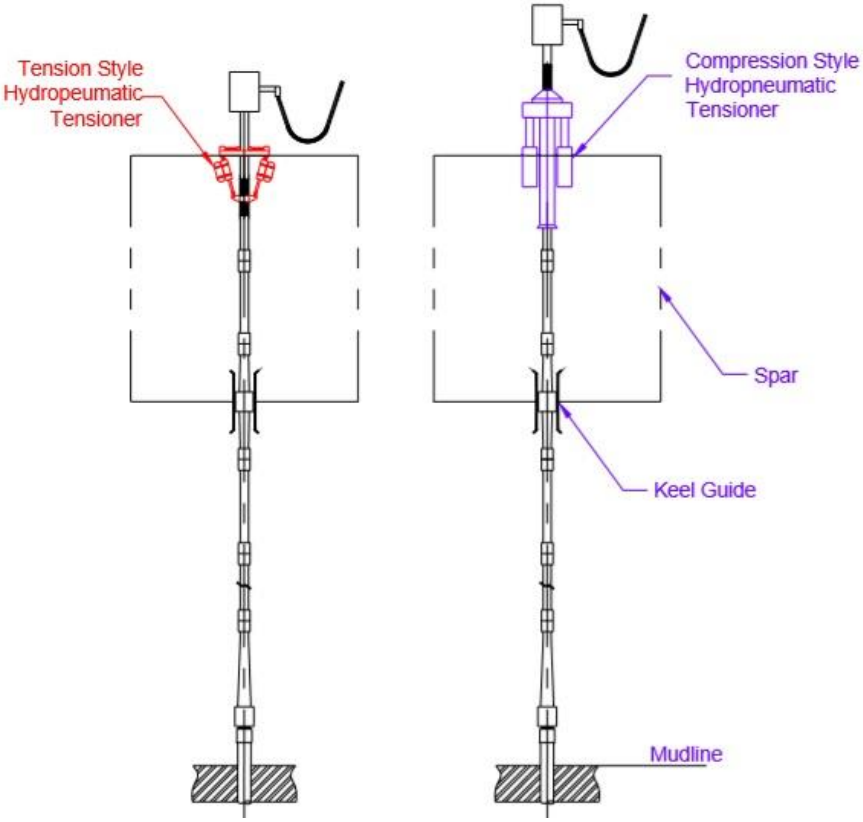

Fig. 1.2 Tension vs compression style tensioner system (Perryman *et al.* 2005)

The tensioner system with parallel configuration of cylinders is called RAM type tensioners. The RAM type tensioner is a hydro-pneumatic passive tensioner system utilizing ram cylinders mounted parallel to the risers (Perryman *et al.* 2005). Perryman *et al.* (2005) studied RAM type tensioners, which were implemented on “Holstein Spar” to support drilling/production risers. Yang and Kim (2010) introduced a linear and nonlinear approach to model TTRs on the Spar. The relationship between tensions and strokes for hydro-pneumatic tensioner is based on the ideal gas equation where the isotropic gas constant can be varied to achieve an optimum stroke design based on tensioner stiffness.

Due to parallel cylinders of compression style tensioner system, the model can be simplified as a single spring without considering the detailed configuration of tensioner cylinders. As presented in Fig. 1.2, in tension style tensioner system, individual cylindrical tensioner bears an angle with a TTR, thus nonlinearity of the system has to be taken into account. Not many finite element (FE) programs currently are applicable of modeling this type of tensioner system considering the detailed configuration of each cylinder, which induces the nonlinearity of the system. Specific models of a tension style tensioner system will be discussed in Section 2.

Previously, the connection point between SCR and hull is assumed to be a hinge in CABLE3D. Yet in real applications, a flex joint will be inserted at the porch and hence bending moments are applied on the upper end of a SCR. For instance, Chen (2002) pointed out that when the moments applied at the porch are neglected, it means flex joints are not modeled. In this study, related improvements will be made to the original CABLE3D program for the analysis of TTR and SCR with a flex joint at its porch.

The up-dated Cable3D will then be integrated into COUPLE. Various coupled analyses of integrated floating structure were performed before. For a typical deep-water Spar such as the 'Constitution' simulated in this study, the ratio of the structure dimension to the characteristic design wavelength is usually small (less than 0.2). Therefore according to slender body approximation (Kim and Chen 1994), the diffraction and radiation effects are neglected and it is assumed that the wave field is not disturbed by the structure, so that the modified Morison equation (Morison *et al.* 1950) is adequate to calculate the first and second-order wave exciting forces (Cao and Zhang 1997). Li (2012) conducted the fully-coupled time-domain analysis for 'Constitution' Spar by utilizing the slender-body approximation without the consideration of diffraction and radiation effects. However, simulation of TTRs and flex joints are not achieved in Li's analysis. In this study, coupled effects caused by tension style tensioner system, buoyancy can, riser guides and flex joints are further investigated by using the up-dated COUPLE for the simulation of 'Constitution'.

2. METHODS AND MODELS

2.1 Simulation of Riser

Both TTRs and SCRs could be modeled as small extensible slender rods with certain bending stiffness. The 1-D Galerkin's method was used to discretize the governing equations, which will be discussed in this section. As what Chen (2002) pointed out, the Newton's method and the Newmark-β method were introduced to solve the static problem and dynamic problem, respectively.

The equations for motion of slender rods are presented below, mainly following the work by Love (1944), Nordgren (1974), Garrett (1982), Paulling and Webster (1986), Ma and Webster (1994) and Chen (2002). The internal state of stress at a point on the rod is described fully by the resultant force **F** and the resultant moment $\tilde{\mathbf{M}}$ acting at the centerline of the rod. Based on the law of conservation of linear momentum and moment of momentum, the governing equations could be obtained:

$$\mathbf{F}' + \mathbf{q} = \rho \ddot{\mathbf{r}}(s,t) \tag{2.1}$$

$$\tilde{\mathbf{M}}' + \mathbf{r}' \times \mathbf{F} + \mathbf{m} = 0 \tag{2.2}$$

where **q** is the distributed external force per unit length, ρ is the mass per unit length, **m** is the external moment per unit length, and a superposed dot denotes differentiation with respect to time. The prime denotes the derivatives with respect to *s*, and *s* means the arc length along the rod. The effects of rotary inertia and shear deformations are neglected.

The resultant moment $\tilde{\mathbf{M}}$ can be written as:

$$\tilde{\mathbf{M}} = \mathbf{r}' \times (B\mathbf{r}'') + H\mathbf{r}' \tag{2.3}$$

$$\tilde{\mathbf{M}}' = \mathbf{r}' \times (B\mathbf{r}'')' + H'\mathbf{r}' + H\mathbf{r}'' \tag{2.4}$$

Where H is the torque and B is the bending stiffness. The torque effects are neglected here, thus $H=0$. Letting $\mathbf{m}=0$ means no external bending moment along the risers except at their ends. Substitute $\tilde{\mathbf{M}}'$ into equation (2.2), we have the follwoing expression for **F**:

$$\mathbf{F} = \lambda\mathbf{r}' - (B\mathbf{r}'')' \tag{2.5}$$

$$\lambda = T - B\kappa^2 \tag{2.6}$$

where $\kappa^2 = -\mathbf{r}' \cdot \mathbf{r}'''$, and κ is the local curvature of the rod, and $T(s,t) = \mathbf{r}' \cdot \mathbf{F}$ is the local tension. According to the inextensibility assumption:

$$\mathbf{r}' \cdot \mathbf{r}' = 1 \tag{2.7}$$

The equation of motion is finally formed by plugging the expression for **F** into (2.1):

$$-(B\mathbf{r}'')'' + (\lambda\mathbf{r}')' + \mathbf{q} = \rho\ddot{\mathbf{r}} \tag{2.8}$$

Equation (2.7) can be expanded to allow for small extension by:

$$\mathbf{r}' \cdot \mathbf{r}' = (1+\varepsilon)^2 \tag{2.9}$$

where $\varepsilon = \dfrac{T}{EA}$, EA is the elastic stiffness of the riser. When ε is very small, equation of motion (2.8) and equation of Lagrange multiplier λ (2.6) are valid.

The external forces $\mathbf{q}$ applied on the riser include gravity forces, hydrostatic and hydrodynamic forces. The gravity force gives rise to a distributed load on the riser:

$$\mathbf{q}_t(s,t) = -\rho_t g A_t \mathbf{e}_y \tag{2.10}$$

The hydrodynamic forces consist of added-mass force, drag force, and Froude-Krylov force. The first two terms are predicted by Morrison equation:

$$\mathbf{q}_f^I(s,t) = \rho_f A_f C_{Mn} \mathbf{N}(\mathbf{a}_f - \ddot{\mathbf{r}}) + \rho_f A_f C_{Mt} \mathbf{T}(\mathbf{a}_f - \ddot{\mathbf{r}}) \tag{2.11}$$

$$\begin{aligned} \mathbf{q}_f^D(s,t) &= \frac{1}{2}\rho_f D_f C_{Dn} \mathbf{N}(\mathbf{v}_f - \dot{\mathbf{r}})\left|\mathbf{N}(\mathbf{v}_f - \dot{\mathbf{r}})\right| \\ &+ \frac{1}{2}\rho_f D_f C_{Dt} \mathbf{T}(\mathbf{v}_f - \dot{\mathbf{r}})\left|\mathbf{T}(\mathbf{v}_f - \dot{\mathbf{r}})\right| \end{aligned} \tag{2.12}$$

where C_{Mn}, C_{Mt}, C_{Dn} and C_{Dt} are the normal added-mass coefficient, tangential added-mass coefficient, normal drag coefficient and tangential drag coefficient, respectively.

Froude - Krylov force due to sea water outside the riser is:

$$\mathbf{q}_f^{F-K}(s,t) = \rho_f (g\mathbf{e}_y + \mathbf{a}_f) A_f + (P_f A_f \mathbf{r}')' \tag{2.13}$$

Froude-Krylov force (pressure forces) due to the fluid inside the rod is:

$$\mathbf{q}_i^{F-K}(s,t) = -\rho_i g A_i \mathbf{e}_y - (P_i A_i \mathbf{r}')' \tag{2.14}$$

Where:

$\rho = \rho_t A_t + \rho_i A_i$, the mass per unit rod (including the internal fluid),

$\rho_f(s)$ = the mass density of the sea water,

$\rho_i(s)$ = the mass density of the inside fluid,

ρ_t (s) = the mass density of the tube,

$A_f(s)$ = the outer cross-section area of the rod,

$D_f(s)$ = the diameter of the rod,

$A_i(s)$ = the inner cross-section area of the rod,

$A_t(s)$ = the structural cross-section area of the rod,

$\mathbf{v}_f$ = the velocity of the sea water (current and wave),

$\mathbf{a}_f$ = the acceleration of the sea water (current and wave),

P_f = pressure of the sea water,

P_i = pressure of the internal fluid,

T, **N** = transfer matrices,

I = identity matrix,

where the subscripts *f*, *i* and *t* denote the sea water, the fluid inside the riser and the riser itself. **T** and **N** are defined by:

$$\mathbf{T} = \mathbf{r}'^T \mathbf{r}' \tag{2.15}$$

$$\mathbf{N} = \mathbf{I} - \mathbf{T} \tag{2.16}$$

The governing equation is:

$$\mathbf{M}\ddot{\mathbf{r}} + (B\mathbf{r}'')'' - (\tilde{\lambda}\mathbf{r}')' = \mathbf{q} \tag{2.17}$$

where

$$\begin{aligned}\mathbf{q} = (\rho_f A_f - \rho_i A_i - \rho_t A_t) g \mathbf{e}_y + \rho_f A_f (\mathbf{I} + C_{Mn}\mathbf{N} + C_{Mt}\mathbf{T})\mathbf{a}_f \\ + \frac{1}{2}\rho_f D_f C_{Dn} \mathbf{N}(\mathbf{v}_f - \dot{\mathbf{r}})\left|\mathbf{N}(\mathbf{v}_f - \dot{\mathbf{r}})\right| \\ + \frac{1}{2}\rho_f D_f C_{Dt} \mathbf{T}(\mathbf{v}_f - \dot{\mathbf{r}})\left|\mathbf{T}(\mathbf{v}_f - \dot{\mathbf{r}})\right|\end{aligned} \tag{2.18}$$

$$\mathbf{M} = (\rho_t A_t + \rho_i A_i)\mathbf{I} + \rho_f A_f C_{Mn}\mathbf{N} + \rho_f A_f C_{Mt}\mathbf{T} \tag{2.19}$$

$$\tilde{\lambda} = (T + P_f A_f - P_i A_i) - B\kappa^2 \tag{2.20}$$

and assume curvature κ is small, then ε can be expressed as:

$$\varepsilon = \frac{T}{EA} \approx \frac{\tilde{\lambda} - P_f A_f + P_i A_i}{EA} \tag{2.21}$$

The Galerkin's method is adopted to discretize the partial differential equations of motion from (2.17), and the constraints equations (2.9) and (2.21) in space, resulting in a set of nonlinear 2nd-order ordinary differential equations in the time domain. This is a 1-D problem. The discretization is performed on a 1-D rod.

Equation (2.17) may be reduced to a set of ordinary differential equations using Galerkin's method. Multiplying both side of the equation by $a_i(s)$ and integrating it with respect to s from 0 to L for an element of the length of L:

$$\int_0^L \left\{ \mathbf{M}\ddot{\mathbf{r}} + (B\mathbf{r}'')'' - (\tilde{\lambda}\mathbf{r}')' - \mathbf{q} \right\} a_i(s)\, ds = 0 \tag{2.22}$$

where the Hermite cubic shape function $a(s)$ are:

$$\begin{aligned} a_1(\xi) &= 1 - 3\xi^2 + 2\xi^3 \\ a_2(\xi) &= \xi - 2\xi^2 + \xi^3 \\ a_3(\xi) &= 3\xi^2 - 2\xi^3 \\ a_4(\xi) &= -\xi^2 + \xi^3 \end{aligned} \tag{2.23}$$

Integrating the above equation by parts results in equation (2.24):

$$\begin{aligned}&\int_0^L \left\{\mathbf{M}\ddot{\mathbf{r}}a_i(s) + B\mathbf{r}''a_i''(s) + \tilde{\lambda}\mathbf{r}'a_i'(s) - \mathbf{q}\,a_i(s)\right\}ds \\ &= B\mathbf{r}''a_i'(s)\Big|_o^L + \left\{\tilde{\lambda}\mathbf{r}' - (B\mathbf{r}'')'\right\}a_i(s)\Big|_0^L\end{aligned} \tag{2.24}$$

The first term on the right-hand side of the equation is related to the moments at the ends of the element, and the second term (in curly brackets) is the forces at the ends of the element. The right-hand side terms are called generalized forces $\mathbf{f}_i$, which can be expressed as:

$$\mathbf{f}_i = B\mathbf{r}''a'_i\Big|_o^L + \left\{\tilde{\lambda}\mathbf{r}' - (B\mathbf{r}'')'\right\}a_i\Big|_0^L\text{, for } i = 1,2,3,4 \tag{2.25}$$

$$\mathbf{f}_1 = -\left\{\tilde{\lambda}\mathbf{r}'(0) - (B\mathbf{r}'')'(0)\right\} = -\mathbf{F}(0) \tag{2.26}$$

$$\mathbf{f}_2 = -\frac{1}{L}B\mathbf{r}''(0) = \frac{1}{L}\mathbf{r}'(0)\times\tilde{\mathbf{M}}(0) \tag{2.27}$$

$$\mathbf{f}_3 = \left\{\tilde{\lambda}\mathbf{r}'(L) - (B\mathbf{r}'')'(L)\right\} = \mathbf{F}(L) \tag{2.28}$$

$$\mathbf{f}_4 = \frac{1}{L}B\mathbf{r}''(0) = -\frac{1}{L}\mathbf{r}'(L)\times\tilde{\mathbf{M}}(L) \tag{2.29}$$

The details of adopting shape functions to discretize the motion equation and constraints equation could be found in work by Chen *et al* (2002). At free ends of the first and last elements, it is necessary to supply the boundary conditions. If N elements are used to describe a line in three dimensions, then the procedure results in $15+8(N\text{-}1)$ independent equations and coefficients. After the formation of the global system of equations $\mathbf{A}\delta\mathbf{X}=\mathbf{B}$, different boundary conditions will be added into the global equation for different types of risers, which will be discussed in later subsections.

2.2 Numerical Model of TTR

2.2.1 Numerical Model of Tensioner System

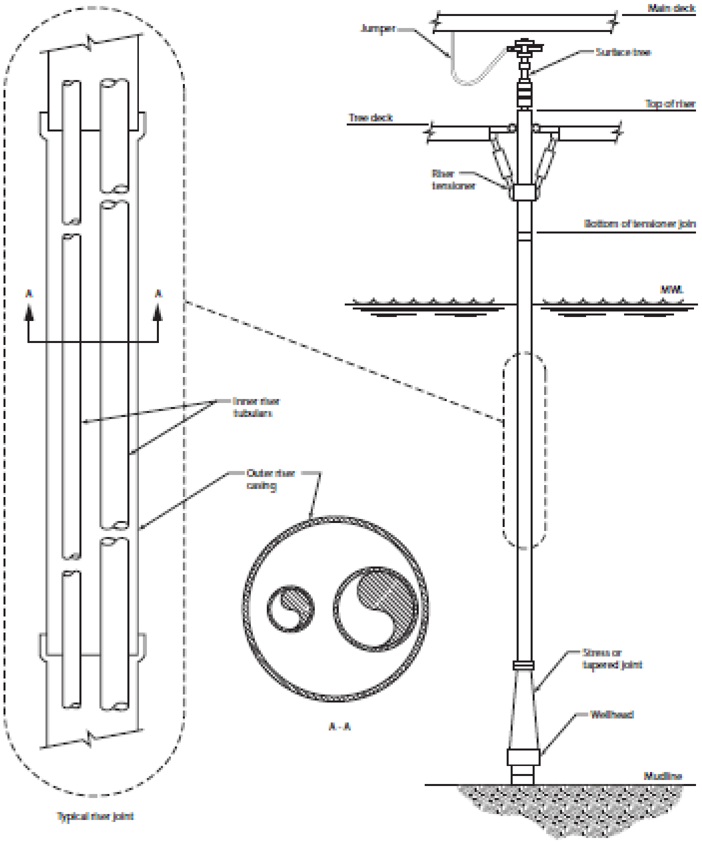

Fig. 2.1 Configuration of top-tensioned riser (API RP 2RD)

The configuration of top-tensioned riser is shown in Fig. 2.1 (API RP 2RD). When a concentrated force ($\tilde{\mathbf{f}}$) is applied at s_0 along a slender rod, say a TTR (top tensioned riser), the corresponding forces can be added to the dynamic equations by introducing a δ function as follows (Chen 2002):

$$\mathbf{M}\ddot{\mathbf{r}} + (B\mathbf{r}'')'' - (\tilde{\lambda}\mathbf{r}')' - \mathbf{q} + \delta(s - s_0)\left\{-\tilde{\mathbf{f}}\right\} = 0 \tag{2.30}$$

In the use of the finite element analysis, the locations of concentrated forces are often defined at certain nodes. In modeling a TTR, beam elements with bending stiffness are selected. For such elements, the boundary conditions between two adjacent elements are (Chen 2002):

$$\begin{gathered} {}^{(n)}u_{3n} = {}^{(n+1)}u_{1n} \\ {}^{(n)}u_{4n} / L^{(n)} = {}^{(n+1)}u_{2n} / L^{(n+1)} \\ {}^{(n)}\tilde{\lambda}_3 = {}^{(n+1)}\tilde{\lambda}_1 \end{gathered} \tag{2.31}$$

$$\begin{aligned} {}^{(n)}\mathbf{f}_3 + {}^{(n+1)}\mathbf{f}_1 &= \tilde{\mathbf{f}} \\ {}^{(n)}\mathbf{f}_4 L^{(n)} + {}^{(n+1)}\mathbf{f}_2 L^{(n+1)} &= 0 \end{aligned} \tag{2.32}$$

The three formulas in (2.31) represent continuity of displacement, continuity of slope and continuity of tension, respectively. The first formula in (2.32) shows that the difference between action and reaction force at a node is equal to the concentrated force applied at this node, and the second formula in (2.32) illustrates the continuity of bending moment applied at the node. The concentrated force ($\tilde{\mathbf{f}}$) will be denoted as a function of relevant parameters, including stiffness, pretension of and configuration of tensioners, coordinates of the node where the tensioner system applies, etc.

A tensioner system may consist of three to four individual cylindrical tensioners. The tension of an individual tensioner cylinder is approximated by a linear spring. Although the tension provided by an individual tensioner is linear, the stiffness of the whole tensioner system is likely to be nonlinear. The initial pretension of each tensioner is denoted by $\vec{f}_{0i}$ and its initial length is denoted by L_{0i}. The length of a tensioner at a given time step is L_i, where *i* specifies an individual tensioner, *i*. For instance, if there are four tensioners, *i* ranges from 1 to 4. The corresponding spring stiffness is given by k_i. Hence, the tension at each time step is given by:

$$\left|\vec{f}_i\right| = \left|\vec{f}_{0i}\right| + k_i(L_i - L_{0i}) \tag{2.33}$$

where $\left|\vec{f}_i\right|$ represents the tension of the *i*th tensioner, which is a function of time and a scalar denoting the magnitude of the tension. L_i and L_{0i} are given below.

$$L_i = \left|\vec{D}_i - (\vec{r}_i + \delta\vec{r}_i)\right|$$

$$L_{0i} = \left|\vec{D}_{0i} - \vec{r}_{0i}\right| \tag{2.34}$$

where $\vec{D}_i$ represents the coordinates of upper end of a tensioner, which is its connection point to the upper deck, $\vec{r}_i$ is the coordinate of the lower end of the tensioner, which is the connection between tensioner and riser, at a time step. $\vec{D}_{0i}$ is the initial position of the upper end of *i*th tensioner while $\vec{r}_{0i}$ represents the initial position of the lower end of the tensioner.

The three components of $\vec{f}_i$ in the *x*, *y*, *z* directions can be obtained by introducing a unit direction vector $\vec{d}_i$. $\vec{d}_i$ is defined by the following formula.

$$\vec{d}_i = \frac{\vec{D}_i - (\vec{r}_i + \delta\vec{r}_i)}{\left|\vec{D}_i - (\vec{r}_i + \delta\vec{r}_i)\right|} \tag{2.35}$$

All tensioners in the same tensioner system are attached to a TTR through a load ring. Hence $\vec{r}_i$ is calculated based on the coordinates of the center point of riser where the load ring is attached. $\delta\vec{r}_i$ is the unknown increment of $\vec{r}_i$ at each iterative step and it will be calculated in solving the global matrix. Thus $\vec{r}_i + \delta\vec{r}$ is the predictive coordinates at each time step. It is noted that $\delta\vec{r}_i$ is the same for all tensioner cylinders because the load ring is considered to be rigid.

Using the Taylor expansion and discarding the high-order terms $O\left(\frac{\delta r_i^{\,2}}{l_i^{\,2}}\right)$, we obtain the expression for L_i:

$$L_i = \left|\vec{D}_i - (\vec{r}_i + \delta\vec{r}_i)\right| = l_i\left[1 + \frac{-2(D_{i1} - r_{i1})}{l_i^{\,2}}\delta r_{i1} + \frac{-2(D_{i2} - r_{i2})}{l_i^{\,2}}\delta r_{i2} + \frac{-2(D_{i3} - r_{i3})}{l_i^{\,2}}\delta r_{i3}\right]^{1/2}$$

(2.36)

where $l_i = \left[(D_{i1} - r_{i1})^2 + (D_{i2} - r_{i2})^2 + (D_{i3} - r_{i3})^2\right]^{1/2}$.

By introducing the approximation $(1+x)^{-\frac{1}{2}} \cong 1 - \frac{1}{2}x$ when $x <<1$, the equation can be linearized to:

$$L_i = l_i\left[1 - \frac{(D_{i1} - r_{i1})}{l_i^{\,2}}\delta r_{i1} - \frac{(D_{i2} - r_{i2})}{l_i^{\,2}}\delta r_{i2} - \frac{(D_{i3} - r_{i3})}{l_i^{\,2}}\delta r_{i3}\right] \qquad (2.37)$$

Similarly, the expression for $\frac{1}{L_i}$, which will be used in the computation of $\vec{d}_i$, can be obtained.

$$\frac{1}{L_i} = \frac{1}{l_i}\left[1 + \frac{(D_{i1} - r_{i1})}{l_i^{\,2}}\delta r_{i1} + \frac{(D_{i2} - r_{i2})}{l_i^{\,2}}\delta r_{i2} + \frac{(D_{i3} - r_{i3})}{l_i^{\,2}}\delta r_{i3}\right]$$

(2.38)

Then substituting the above expression into formula (2.35) for $\vec{d}_i$, the following formulas can be acquired:

$$d_{i1} = \left(\frac{D_{i1}-r_{i1}}{l_i}\right)\left[1-\frac{1}{D_{i1}-r_{i1}}\delta r_{i1}+\frac{(D_{i1}-r_{i1})}{l_i^{\;2}}\delta r_{i1}+\frac{(D_{i2}-r_{i2})}{l_i^{\;2}}\delta r_{i2}+\frac{(D_{i3}-r_{i3})}{l_i^{\;2}}\delta r_{i3}\right]$$
$$d_{i2} = \left(\frac{D_{i2}-r_{i2}}{l_i}\right)\left[1-\frac{1}{D_{i2}-r_{i2}}\delta r_{i2}+\frac{(D_{i1}-r_{i1})}{l_i^{\;2}}\delta r_{i1}+\frac{(D_{i2}-r_{i2})}{l_i^{\;2}}\delta r_{i2}+\frac{(D_{i3}-r_{i3})}{l_i^{\;2}}\delta r_{i3}\right]$$
$$d_{i3} = \left(\frac{D_{i3}-r_{i3}}{l_i}\right)\left[1-\frac{1}{D_{i3}-r_{i3}}\delta r_{i3}+\frac{(D_{i1}-r_{i1})}{l_i^{\;2}}\delta r_{i1}+\frac{(D_{i2}-r_{i2})}{l_i^{\;2}}\delta r_{i2}+\frac{(D_{i3}-r_{i3})}{l_i^{\;2}}\delta r_{i3}\right]$$

(2.39)

Finally the three components of $\vec{f}_i$ are obtained by $f_{ij} = |f_i| d_{ij}$,

$$f_{i1} = T_i\,\frac{D_{i1}-r_{i1}}{l_i}\left\{\begin{array}{l} 1+\left[\dfrac{D_{i1}-r_{i1}}{l_i^{\;2}}-\dfrac{k_i\left(D_{i1}-r_{i1}\right)}{T_i l_i}-\dfrac{1}{D_{i1}-r_{i1}}\right]\delta r_{i1}+ \\ \left[\dfrac{D_{i2}-r_{i2}}{l_i^{\;2}}-\dfrac{k_i\left(D_{i2}-r_{i2}\right)}{T_i l_i}\right]\delta r_{i2}+\left[\dfrac{D_{i3}-r_{i3}}{l_i^{\;2}}-\dfrac{k_i\left(D_{i3}-r_{i3}\right)}{T_i l_i}\right]\delta r_{i3} \end{array}\right\}$$

(2.40)

$$f_{i2} = T_i\,\frac{D_{i2}-r_{i2}}{l_i}\left\{\begin{array}{l} 1+\left[\dfrac{D_{i1}-r_{i1}}{l_i^{\;2}}-\dfrac{k_i\left(D_{i1}-r_{i1}\right)}{T_i l_i}\right]\delta r_{i1}+ \\ \left[\dfrac{D_{i2}-r_{i2}}{l_i^{\;2}}-\dfrac{k_i\left(D_{i2}-r_{i2}\right)}{T_i l_i}-\dfrac{1}{D_{i2}-r_{i2}}\right]\delta r_{i2}+\left[\dfrac{D_{i3}-r_{i3}}{l_i^{\;2}}-\dfrac{k_i\left(D_{i3}-r_{i3}\right)}{T_i l_i}\right]\delta r_{i3} \end{array}\right\}$$

(2.41)

$$f_{i3} = T_i \frac{D_{i3} - r_{i3}}{l_i} \left\{ \begin{array}{l} 1 + \left[\dfrac{D_{i1} - r_{i1}}{l_i{}^2} - \dfrac{k_i \left(D_{i1} - r_{i1} \right)}{T_i l_i} \right] \delta r_{i1} + \\ \left[\dfrac{D_{i2} - r_{i2}}{l_i{}^2} - \dfrac{k_i \left(D_{i2} - r_{i2} \right)}{T_i l_i} \right] \delta r_{i2} + \left[\dfrac{D_{i3} - r_{i3}}{l_i{}^2} - \dfrac{k_i \left(D_{i3} - r_{i3} \right)}{T_i l_i} - \dfrac{1}{D_{i3} - r_{i3}} \right] \delta r_{i3} \end{array} \right\} \tag{2.42}$$

where $T_i = \left| \vec{f}_{0i} \right| + k_i \left(l_i - \left| \vec{D}_{0i} - \vec{r}_{0i} \right| \right)$.

Substituting the expression for f_{ij} into the governing equation (2.30) and moving the terms related to $\delta \vec{r}_i$ to the left side of the global equations **A**δ**X**=**B**, we allow the effects of a tensioner system in the dynamic analysis of a TTR.

2.2.2 A Simplified Approach of Modeling TTRs with Buoyancy Can

For TTRs tensioned by buoyancy cans, the top tension of a TTR is provided by buoyancy cans attached at its top. TTRs are designed to be laterally constrained by the riser guides at several Spar elevations but are allowed to move independently in the vertical direction (Chen and Nurtjahyo 2004). The buoyancy is constant due to the constant volume of can. There are two approaches of modeling this TTR type. The first is to introduce different element types while discretizing the riser. For elements within the buoyancy can area, the buoyancy of cans is integrated into the element properties, which are the input of CABLE3D. In this way the buoyancy is distributed evenly onto the corresponding riser segment. The second approach is to model the buoyancy can as concentrated force acting on the upper end of the riser, following equation (2.30). The first approach is selected in this study.

2.3 Numerical Model of Upper Deck and Riser Guide

In modeling TTRs, the effects of upper deck and riser guides will be taken into account. The motion of offshore structures is transmitted to TTRs through upper deck and riser guides. The vertical friction between TTRs and upper deck or riser guides is neglected, since rollers are placed here to minimize the friction. As shown in Fig. 1.2, upper deck locates on top of tensioner system. Riser guides are often below the sea surface and the lowest among them at the bottom is called keel guide (See Fig. 2.2). More riser guides are likely to be constructed at various elevations of the Spar due to its deep draft and long length of TTR within the moon pool or truss.

The locations of connection points between TTRs and upper deck or riser guides at each time step are crucial to TTR motion. Translation and rotation motions of a floating platform are considered to determine the instant location of the riser guides. The relationship between space-fixed coordinates $\hat{\mathbf{x}} = (\hat{x}, \hat{y}, \hat{z})^t$ and body-fixed coordinates $\mathbf{x} = (x, y, z)^t$ is given by Chen (2002)

$$\hat{\mathbf{x}} = \boldsymbol{\xi} + \mathbf{T}^t \mathbf{x} \tag{2.43}$$

where

$\boldsymbol{\xi} = (\xi_1, \xi_2, \xi_3)^t$, is the translation displacement of the body expressed in the space fixed coordinate system $\hat{o}\hat{x}\hat{y}\hat{z}$,

T is a transfer matrix between body-fixed coordinate system and the space-fixed coordinate system, superscript *t* represents transpose of a matrix.

$$\mathbf{T} = \begin{bmatrix} \cos\alpha_3\cos\alpha_2 & \sin\alpha_3\cos\alpha_1 + \cos\alpha_3\sin\alpha_2\sin\alpha_1 & \sin\alpha_3\sin\alpha_1 - \cos\alpha_3\sin\alpha_2\cos\alpha_1 \\ -\sin\alpha_3\cos\alpha_2 & \cos\alpha_3\cos\alpha_1 - \sin\alpha_3\sin\alpha_2\sin\alpha_1 & \cos\alpha_3\sin\alpha_1 + \sin\alpha_3\sin\alpha_2\cos\alpha_1 \\ \sin\alpha_2 & -\cos\alpha_2\sin\alpha_1 & \cos\alpha_2\cos\alpha_1 \end{bmatrix}$$

T is an orthogonal matrix with the property that $\mathbf{T}^t = \mathbf{T}^{-1}$

$\boldsymbol{\alpha} = (\alpha_1, \alpha_2\ \alpha_3)^t$ are the Euler angles in the sequence of the roll-pitch-yaw motion

Since the body-fixed coordinates of upper deck and riser guides are known in advance, their instant location can be calculated using the above formulas.

Because the vertical relative motion between TTR and upper deck/riser guide is not constrained, the instant contacting locations of the upper deck and riser guides will move along TTR. The related transient positions are determined at each time step and lateral support from riser guides is acting on the node closest to their transient positions. To ensure high accuracy, small elements with short lengths are recommended to better approximate the precise locations of connection points.

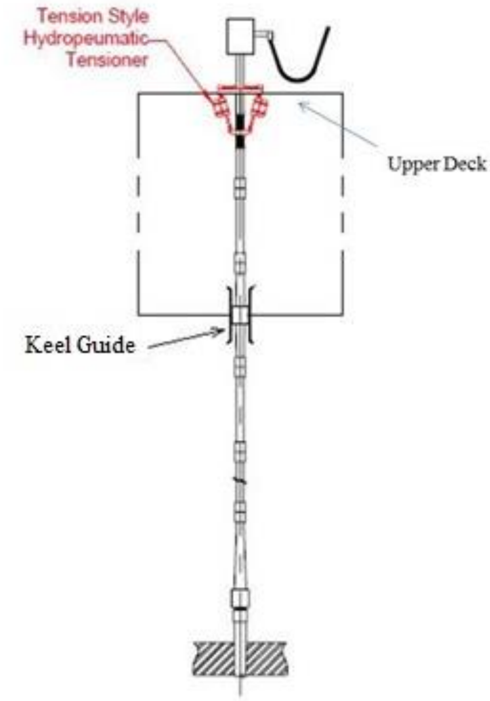

Fig. 2.2 Configuration of tensioner system and riser guides (Perryman *et al.* 2005)

2.4 Numerical Model of Flex Joint

The bending moment at a flex joint is denoted by $\tilde{\mathbf{M}}(\vec{\boldsymbol{r}}'(t)+\boldsymbol{\delta}\vec{\boldsymbol{r}}'(t))$. It is induced by the angle θ between $\vec{\boldsymbol{r}}'(t)+\boldsymbol{\delta}\vec{\boldsymbol{r}}'(t)$ and $\vec{\boldsymbol{r}}'_0$, where $\vec{\boldsymbol{r}}'(t)+\boldsymbol{\delta}\vec{\boldsymbol{r}}'(t)$ represents the direction vector at the upper end of riser at time step *(t)* and $\vec{\boldsymbol{r}}'_0$ the direction vector when no moment is applied at the flex joint (equilibrium position for most cases). θ can be calculated if $\vec{\boldsymbol{r}}'(t)+\boldsymbol{\delta}\vec{\boldsymbol{r}}'(t)$ and $\vec{\boldsymbol{r}}'_0$ are known. The direction of $\tilde{\mathbf{M}}$ can also be determined by $(\vec{r}\,'(t)+\delta\vec{r}\,'(t))\times\vec{r}\,'_0$ (See Fig. 2.3).

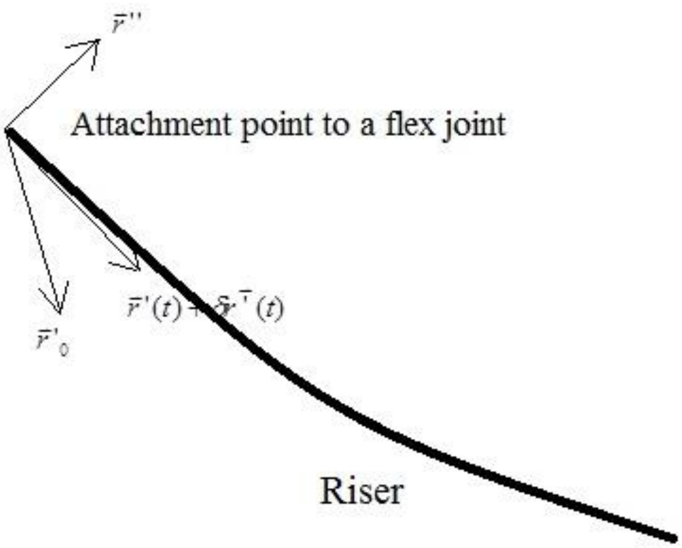

Fig. 2.3 Directions of related vectors $\vec{r}'(t)+\delta\vec{r}'(t)$, $\vec{r}'_0$, and $\vec{r}''$

At first, the magnitude of the moment is calculated by,

$$\tilde{\mathbf{M}} = M_0\boldsymbol{\theta} \tag{2.44}$$

where M_0 represents the linear rotational stiffness of the flex joint, which should be provided by the user based on the types of the flex joint used in the design. The magnitude of $\boldsymbol{\theta}$ is given by

$$\theta = \arcsin\left[1-\left(\frac{(\vec{\boldsymbol{r}}'+\delta\vec{\mathbf{r}}')\cdot\vec{\boldsymbol{r}}'_0}{\left|\vec{\boldsymbol{r}}'+\delta\vec{\mathbf{r}}'\right|\left|\vec{\boldsymbol{r}}'_{\boldsymbol{0}}\right|}\right)^2\right]^{\frac{1}{2}} \tag{2.45}$$

Assuming that the elongation of the riser can be ignored, both $\left|\vec{\boldsymbol{r}}'+\delta\vec{\boldsymbol{r}}'\right|$ and $\left|\vec{\boldsymbol{r}}'_{0}\right|$ are equal to 1. The Taylor expansion of $\arcsin\left[1-\left(\frac{(\vec{\boldsymbol{r}}'+\delta\vec{\boldsymbol{r}}')\cdot\vec{\boldsymbol{r}}'_0}{\left|\vec{\boldsymbol{r}}'+\delta\vec{\boldsymbol{r}}'\right|\left|\vec{\boldsymbol{r}}'_0\right|}\right)^2\right]^{\frac{1}{2}}$ is given by:

$$\theta=\sum_{n=0}^{+\infty}\frac{(2n)!}{4^n(n!)^2(2n+1)}x^{2n+1}\ \text{ and }\ x=\left[1-\left(\frac{(\vec{\boldsymbol{r}}'+\delta\vec{\boldsymbol{r}}')\cdot\vec{\boldsymbol{r}}'_0}{\left|\vec{\boldsymbol{r}}'+\delta\vec{\boldsymbol{r}}'\right|\left|\vec{\boldsymbol{r}}'_0\right|}\right)^2\right]^{\frac{1}{2}} \tag{2.46}$$

From Chen (2002),

$$\tilde{\mathbf{M}}=\bar{\mathbf{r}}'\times(B\bar{\mathbf{r}}'')+H\bar{\mathbf{r}}' \tag{2.47}$$

where H is the torque and B is the bending stiffness. $H=0$ is assumed in this case. According to headings of $\vec{\boldsymbol{r}}'(t)+\boldsymbol{\delta}\vec{\boldsymbol{r}}'(t)$, $\vec{r}'_0$ and $\vec{r}''$ (See Fig. 2.4), it could be shown that the direction of $\tilde{\mathbf{M}}$ can be obtained by $\vec{r}_0'\times(\vec{r}'+\delta\vec{r}')$, which is denoted as vector $\vec{t}$:

$$\vec{t}=\left[r_{02}'(r_3'+\delta r_3')-r_{03}'(r_2'+\delta r_2')\right]\vec{i}+\left[r_{03}'(r_1'+\delta r_1')-r_{01}'(r_3'+\delta r_3')\right]\vec{j}+\left[r_{01}'(r_2'+\delta r_2')-r_{02}'(r_1'+\delta r_1')\right]\vec{k} \tag{2.48}$$

where $\vec{i}$, $\vec{j}$, $\vec{k}$ represent the unit vector in x, y, and z direction. And, assuming $\left|\vec{t}\right|=\left|\vec{r}_0'\right|\left|\vec{r}'+\delta\vec{r}'\right|\sin\theta=\sin\theta$, hence

$$\frac{1}{\left|\vec{t}\right|}=\left[1-(\vec{r}'\cdot\vec{r}_0'+r_{01}'\delta r_1'+r_{02}'\delta r_2'+r_{03}'\delta r_3')^2\right]^{-1/2}=\frac{1}{\sqrt{1-(\vec{r}'\cdot\vec{r}_0')^2}\left[1-\frac{2\vec{r}'\cdot\vec{r}_0'}{1-(\vec{r}'\cdot\vec{r}_0')^2}(r_{01}'\delta r_1'+r_{02}'\delta r_2'+r_{03}'\delta r_3')\right]^{\frac{1}{2}}} \tag{2.49}$$

So the total moment $\tilde{\mathbf{M}}=(M_x,M_y,M_z)$ can be obtained as the following.

$$M_x = M_0 \theta \frac{r_{02}'(r_3' + \delta r_3') - r_{03}'(r_2' + \delta r_2')}{|\vec{t}|}, \tag{2.50}$$

$$M_y = M_0 \theta \frac{r_{03}'(r_1' + \delta r_1') - r_{01}'(r_3' + \delta r_3')}{|\vec{t}|} \tag{2.51}$$

$$M_z = M_0 \theta \frac{r_{01}'(r_2' + \delta r_2') - r_{02}'(r_1' + \delta r_1')}{|\vec{t}|} \tag{2.52}$$

After Galerkin Method is used to get a series of ordinary differential equations, the generalized force is calculated by,

$$\mathbf{f}_2 = -\frac{1}{L} B \mathbf{r}''(0) = \frac{1}{L} (\boldsymbol{r}' + \delta \boldsymbol{r}') \times \tilde{\mathbf{M}}(0) \tag{2.53}$$

At the upper end of SCR, $\mathbf{f}_2$ represents the moment exerted by the flex joint on the riser at the porch. Substituting the expression for $\boldsymbol{r}' + \delta \boldsymbol{r}'$ and (M_x, M_y, M_z), the expressions for f_{21}, f_{22}, f_{23} could be obtained. Adding this boundary condition to the global system of equations **A**δ**X**=**B,** the analysis considering the effects of flex joint could be performed.

$$\begin{aligned} f_{21} &= \frac{1}{L}(M_{z0} r_2' - M_{y0} r_3') \\ &+ \frac{1}{L}\left(T_1 r_2' - Q_1 r_3'\right)\delta r_1' + \frac{1}{L}\left(T_2 r_2' - Q_2 r_3' + M_{z0}\right)\delta r_2' + \frac{1}{L}(T_3 r_2' - Q_3 r_3' - M_{y0})\delta r_3' \end{aligned} \tag{2.54}$$

$$\begin{aligned} f_{22} &= \frac{1}{L}(M_{x0} r_3' - M_{z0} r_1') \\ &+ \frac{1}{L}\left(P_1 r_3' - T_1 r_1' - M_{z0}\right)\delta r_1' + \frac{1}{L}\left(P_2 r_3' - T_2 r_1'\right)\delta r_2' + \frac{1}{L}(P_3 r_3' - T_3 r_1' + M_{x0})\delta r_3' \end{aligned} \tag{2.55}$$

$$
\begin{aligned}
f_{23} &= \frac{1}{L}(M_{y0}r_1' - M_{x0}r_2') \\
&+ \frac{1}{L}\left(Q_1 r_1' - P_1 r_2' + M_{y0}\right)\delta r_1' + \frac{1}{L}\left(Q_2 r_1' - P_2 r_2' - M_{x0}\right)\delta r_2' + \frac{1}{L}(Q_3 r_1' - P_3 r_2')\delta r_3'
\end{aligned}
\tag{2.56}
$$

Add the first term of f_{21}, f_{22}, f_{23} onto the right hand side of vector **B,** while other terms are moved to the left hand side of the global system of equation. Necessary changes are to be made on corresponding entries of left matrix **A.**

2.5 Boundary Conditions of Coupled Analysis

2.5.1 Coupled Effects at Riser Guide and Porch

In using 'COUPLE', TTRs and SCRs are modeled by a subroutine, which is similar to CABLE 3D. This subroutine used inside COUPLE includes the interface between risers and hull. Motions of a Spar are transmitted from main program to CABLE3D subroutine and forces and moments will be transmitted to the main program COUPLE after calculation in CABLE3D subroutine. How the translation and rotation motions of offshore structures are transmitted to TTR through upper deck and riser guides were explained in Section 2.3. When the flex joint is considered, the boundary condition at a porch is no longer assumed to be a hinge. This section will discuss how the force and moment induced by the upper deck, riser guides and porches are calculated, mainly following Chen (2002).

O'X'Y'Z' is a space-fixed coordinate system for TTRs and SCRs. Its origin locates at the still water surface and Y' axis directs positive upward. *OXYZ* is a space-fixed coordinate system for the hull, with origin at the still water surface and *Z* axis positive upward. *O'* and *O* are coincident. *oxyz* is a body-fixed coordinate system moving with the body (see Fig. 2.4). At initial position, *o* is as well coincident with *O'* and *O*.

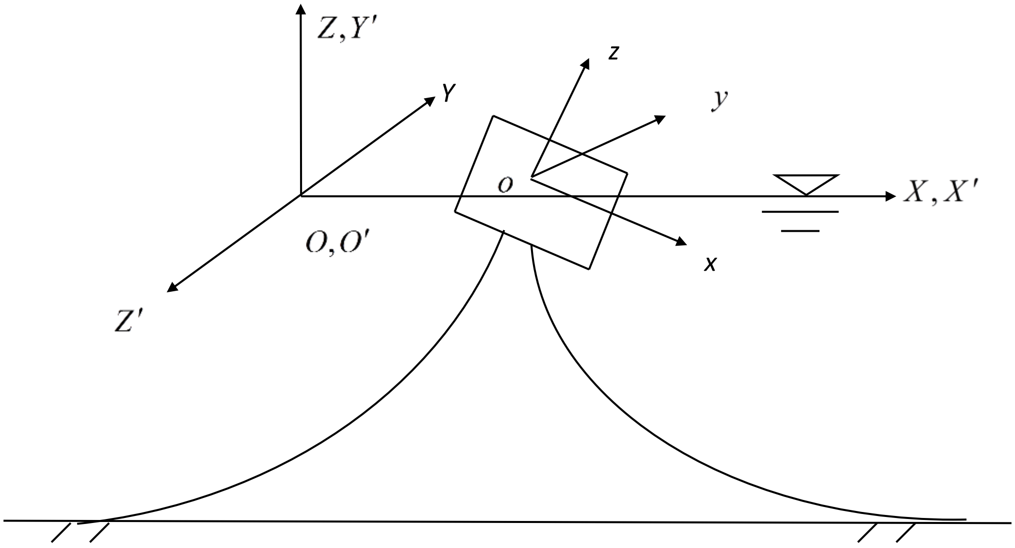

Fig. 2.4 Coordinate system for structure and mooring system

A transfer matrix ***L*** between *OXYZ* and *O'X'Y'Z'* is introduced:

$$\boldsymbol{L} = \begin{Bmatrix} 1 & 0 & 0 \\ 0 & 0 & -1 \\ 0 & 1 & 0 \end{Bmatrix} \tag{2.57}$$

And the coordinates in *O'X'Y'Z'* can be transformed to coordinates in *OXYZ* system by applying the matrix ***L*:**

$$\begin{Bmatrix} \boldsymbol{X} \\ \boldsymbol{Y} \\ \boldsymbol{Z} \end{Bmatrix} = \boldsymbol{L} \begin{Bmatrix} \boldsymbol{X}' \\ \boldsymbol{Y}' \\ \boldsymbol{Z}' \end{Bmatrix} \tag{2.58}$$

Forces and moments applied on the hull at riser guides and porches are the reaction force from TTRs and SCRs,

$$\mathbf{F} = -\mathbf{f}_1 = -(f_{11}, f_{12}, f_{13}) \tag{2.59}$$

$$\tilde{\mathbf{M}}(0) = -\mathbf{r}'(0) \times L\mathbf{f}_2 \tag{2.60}$$

where $\mathbf{f}_1$ refers to generalized forces acting at TTRs through upper deck, riser guide, tensioner system and porch, $\mathbf{f}_2$ refers to generalized moments applied at the upper end of SCR by flex joint at porch and L is element length. $\mathbf{F}$ represents force exerted on the hull, which has opposite direction with $\mathbf{f}_1$. $\tilde{\mathbf{M}}(0)$ denotes the moments applied on the hull via flex joint at the porch and could be obtained from $\mathbf{f}_2$.

If the total number of upper deck, riser guides, tensioner systems, and porches of the whole riser system is M, and the total number of flex joint is N, the forces of the riser system applied on the hull are the summation of forces and moments of each individual riser acting on the structure, which can be expressed as:

$$\mathbf{F}_R = \sum_{m=1}^{M} (\mathbf{LF}_m) \tag{2.61}$$

$$\mathbf{M}_{R1} = \sum_{m=1}^{M} \left[\mathbf{r}_m \times (\mathbf{TLF}_m) \right] \tag{2.62}$$

$$\mathbf{M}_{R2} = \sum_{n=1}^{N} \left[\mathbf{TL}\tilde{\mathbf{M}}_n \right] \tag{2.63}$$

where $\mathbf{F}_R$ refers to the forces applied by TTRs and SCRs, $\mathbf{r}_m$ represents the coordinates of the point of corresponding force component in the body fixed coordinate system *oxy,* and $\mathbf{M}_{R1}$ is the moment induced by $\mathbf{F}_R$. $\mathbf{M}_{R2}$ is the moment applied by flex joints only. $\mathbf{F}_R$ is expressed in the space-fixed coordinate system $\hat{o}\hat{x}\hat{y}\hat{z}$ while both $\mathbf{M}_{R1}$ and $\mathbf{M}_{R2}$ are expressed in the body-fixed coordinate system *oxyz*.

2.5.2 Effects of Structure Rotation on Neutral Angle of A Flex Joint

If the floating structure is experiencing rotation motions, the neutral angle of flex joint will be changed considering that a flex joint is rigidly fixed on the hull. In subsection 2.4, it is determined that $\vec{r}'_0$ represents the direction of vector when no moment is applied at the flex joint and the angle between $\vec{r}'_0$ and the vertical line is the neutral angle. $\vec{r}'_0$ is expressed in the *O'X'Y'Z'*, which is a space-fixed coordinate system for TTRs and SCRs. The formula for the rotation of $\vec{r}'_0$ is presented below,

$$\vec{r}'_{0n} = \mathbf{L}^t\mathbf{T}^t\mathbf{L}\vec{r}_0' \tag{2.64}$$

where $\vec{r}'_{0n}$ is the up-dated direction of vector after considering the rotation of the hull, and $\mathbf{T}$ is a transfer matrix between body-fixed coordinate system and the space-fixed coordinate system, superscript *t* represents transpose of a matrix. By multiplying with $\mathbf{L}$ (defined in Eq.(2.60)), $\vec{r}'_0$ is transformed into *OXYZ*, the space-fixed coordinate system for the hull. After applying matrix $\mathbf{T}^t$, $\vec{r}'_0$ is rotated to a new position due to the roll-pitch-yaw motion. $\mathbf{L}^t$ is used for transforming the direction vector back to the *O'X'Y'Z'* system.

In order to consider the rotation effects on neutral angle, $\bar{\boldsymbol{r}}'_{\boldsymbol{0}}$ is to be replaced by $\bar{r}'_{0n}$ in all formulas related to $\bar{\boldsymbol{r}}'_{\boldsymbol{0}}$ presented in 2.4.

3. CASES USED IN NUMERICAL COMPUTATION

3.1 Top Tension Riser

The TTR selected for the simulation is used in an Ultra Deepwater Dry Tree System for Drilling and Production in the Gulf of Mexico (GoM). All data presented in this section is cited from an online report of FloaTEC, (*RPSEA CTR 1402,* 2009*)*. The depth of water is about 2,400m and the upper end of the riser is 40m above the sea surface. The TTR was used in a SPAR for drilling. The riser sizing is shown in Fig.3.1. Detailed information of this double casing riser is listed in Table 3.1.

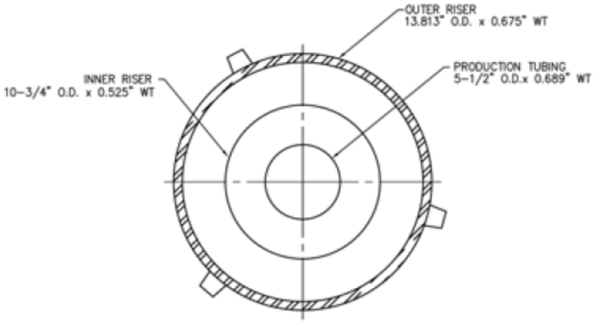

Fig. 3.1 Riser sizing of TTR case (cited from report from FloaTEC, 2009)

It is assumed that riser's top tension is provided by a hydro-pneumatic tensioner system. The total nominal top tension is about 1,800 kips (about 8,000kN). The tensioner system consisted of four tensioner cylinders, each of which has a stiffness of 91.2 kN/m. The stroke-tension relationship of an individual tensioner is assumed to be linear; however, the tensioner system stiffness may be nonlinear. The total stroke of a tensioner is 8 meters. The up limit for stroke is 4 meters and its down limit is 4 meters as well. The tensioner becomes rigid and the stiffness will be very large when the up and down limits are exceeded. According to Yang and Kim (2010), 1.5×10^8 kN/m is to be used when the tensioner system becomes rigid at extreme sea conditions. Within the up and down limits, the tensioner is modeled as a linear spring.

Table 3.1 Physical properties of TTR and parameters needed for analysis.

Physical Properties of TTR	
Length of TTR	2438m
Young's Modulos	206850MPa
Moment of Inertia	3.56E-04 m^4
Mass of Riser Per Unit Length	2.85E+02kg/m
Buoyancy Per Unit Length	9.76E+02N/m
Normal Drag Coefficient	1.2
Tangential Drag Coefficient	0.0
Normal Added-mass Coefficient	1.0
Tangential Added-mass Coefficient	0.0

At the equilibrium position, the upper deck was at about 25 meters above the sea level. Lateral support from the upper deck is considered in our simulation. The elements are divided into two types. The first type of element is above the sea level and the other below the sea level considering the difference between with or without the buoyancy. The first type of elements is used at the top portion of the riser, which is 40 meters above sea level. The second type of element is used for the rest portion of the riser. The density of sea water is $1.03\times10^3\, {kg}/{m^3}$ and the density of inner fluid is $0.90\times10^3\, {kg}/{m^3}$.

Afterwards three riser guides are considered. The vertical distance from each riser guide to the upper deck was 110 meters, 137 meters and 165 meters respectively. The bottom riser guide is known as the keel guide.

3.2 SCR with a Flex Joint at its Porch

The Oil Export SCR studied by Deka *et al.* (2010) is selected for our simulation. The water depth is 5,200ft (1585m) and the porch height is assumed to be at the sea surface. As presented in Fig. 3.2, the outer diameter of riser is 20” (50.8 cm) and its wall thickness is 1.25 inch (3.175 cm). The density of the steel is $7{,}900\, kg/m^3$. Detailed information of the SCR is given in Table.3.2. The SCR top neutral angle was 15 degree from the vertical line, and the 20 inch SCR flexjoint rotational stiffness was 63 kip-ft/degree (4.894×10^6 N-m/rad). The density of the inside fluid is $913\, kg/m^3$ and the seawater density is $1{,}030\, kg/m^3$. The drag coefficient and added mass-coefficient of the risers are taken as 1.6 and 2.0, respectively (Deka *et al.* 2010).

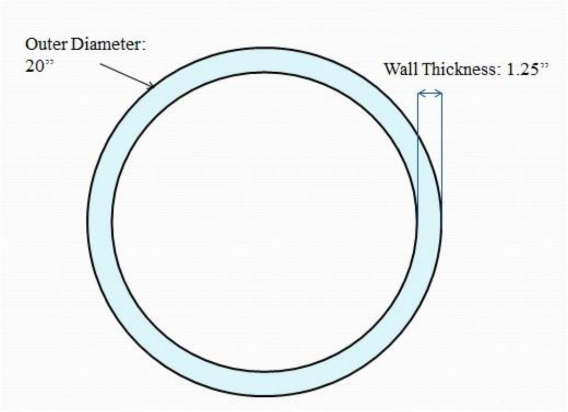

Fig. 3.2 Riser sizing of SCR case

Table 3.2 Physical properties for SCR

Physical Properties of SCR	
Length of SCR	2500m
Young's Modulos	206850MPa
Moment of Inertia	1.40E-03 m^4
Cross Section Area	2.03E-01 m^2
Internal Cavity Area	1.55E-01 m^2
Mass of Riser Per Unit Length	3.75E+02Kg/m
Buoyancy Per Unit Length	2.05E+03N/m
Normal Drag Coefficient	1.6
Tangential Drag Coefficient	0.0
Normal Added-mass Coefficient	2.0
Tangential Added-mass Coefficient	0.0

At equilibrium position, the top neutral angle of SCR is about 15 degree and no moment is exerted by the flex joint. Through trail-and-error of different horizontal excursions, the equilibrium position will be determined when the top angle is closest to 15 degree. Further analysis will be made based on this equilibrium position.

4. RESULTS AND DISCUSSION

4.1 Analysis of TTR

4.1.1 Static Analysis of TTR

For the case stated in 3.1, static analysis is performed by using different offset values at the upper deck as the input. Fig. 4.1 shows the TTR configuration when offset value equals to -100m, -50m, 0m, 50m, 100m respectively. While performing static analysis, the lower end is rigidly fixed. Riser guides are not supplied here, thus the riser segment inside the moon pool bears an angle with the vertical line when the offset is not zero (See Fig. 4.1).

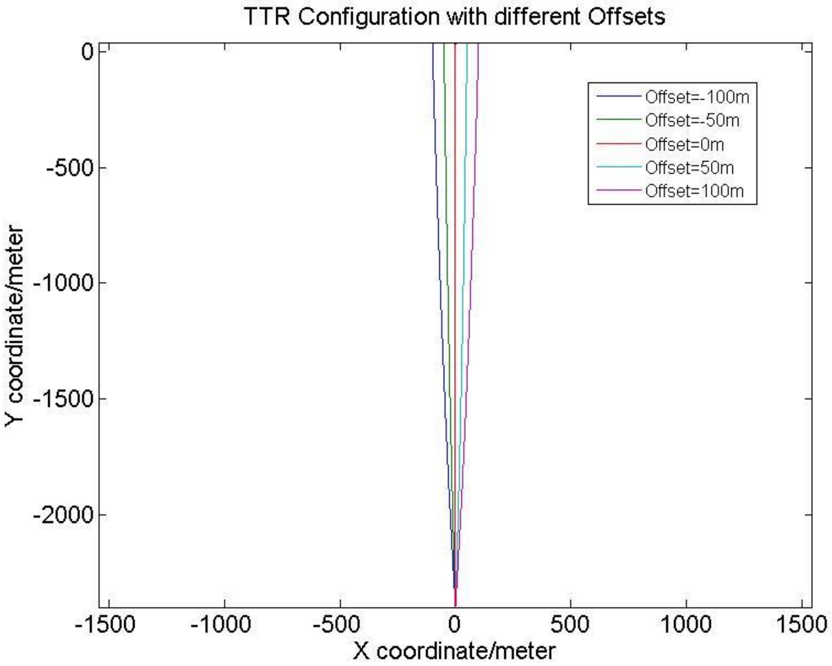

Fig. 4.1 TTR configuration of different offsets at its upper deck

Fig. 4.2 demonstrates the tension distribution from the TTR top to its bottom. At all situations, a sharp increase is observed at the node where the tensioner system is attached. The larger the offset is, the larger the tension will be. In the elements above the tensioner system, negative values of tension are observed due to the compression caused by the weight of the top portion of TTR above the tensioner ring. This compression is tiny and will not result in buckling of the riser.

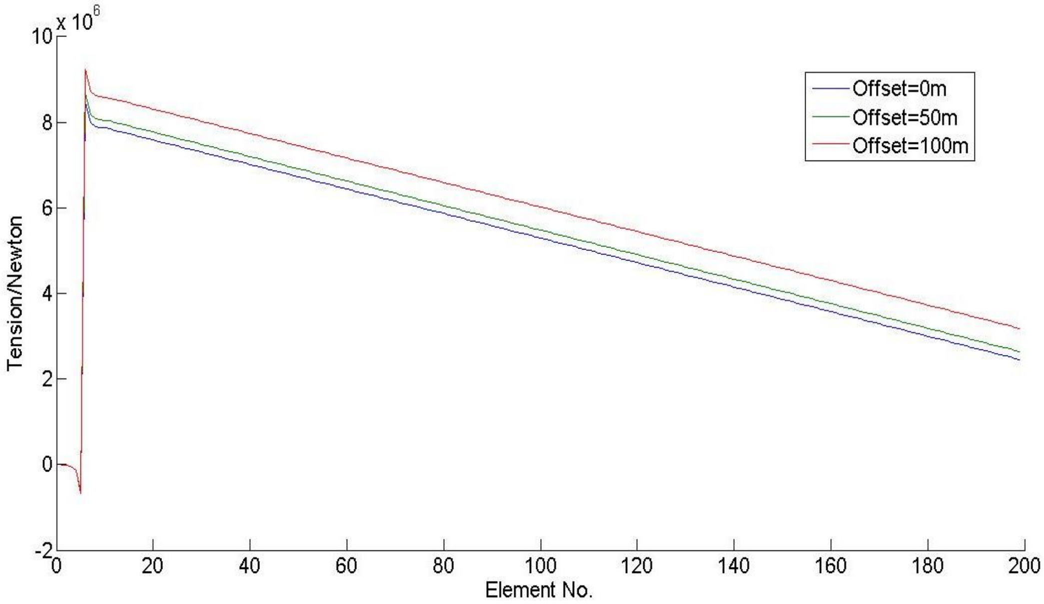

Fig. 4.2 Tension distribution along the TTR

4.1.2 Dynamic Analysis of TTR

Various cases were performed to analyze TTR responses under different harmonic excitations. To ensure stability of the numerical codes, the ramp function lasting for 50 seconds is added onto the very beginning at each simulation. Using the ramp function, the motion gradually reaches fully sinusoidal oscillation without sudden jumps.

4.1.2.1 Results Using Different Sizes of Time Steps

In this subsection, different time steps are used to examine the consistency and stability of the program. Two cases are studied here.

The first case describes the TTR experiencing a heave motion with the amplitude of 2m and period of 15s. In the simulation, the time steps of 0.5s and 0.2s were adopted, respectively. The y coordinate (vertical direction) of the 6th node was traced, where the tensioner system is attached and is 10 meters above the sea surface. The results obtained using different time steps are almost identical (See Fig. 4.3). The amplitude of y-direction motion is very small because this results from the elongation of riser, which is very tiny.

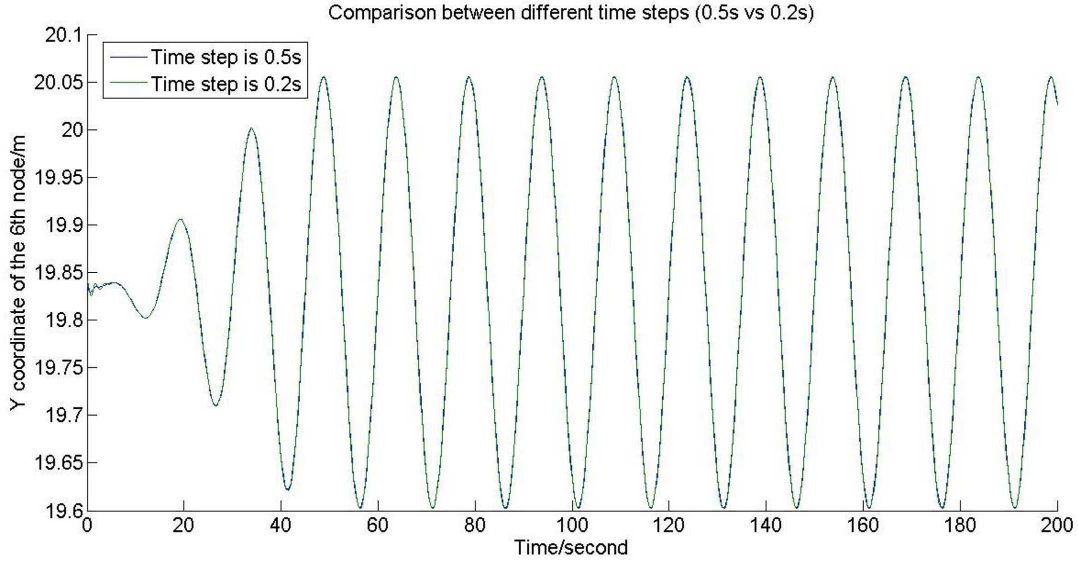

Fig. 4.3 Y-direction of the 6th node with times steps of 0.2s and 0.5s in heave motion

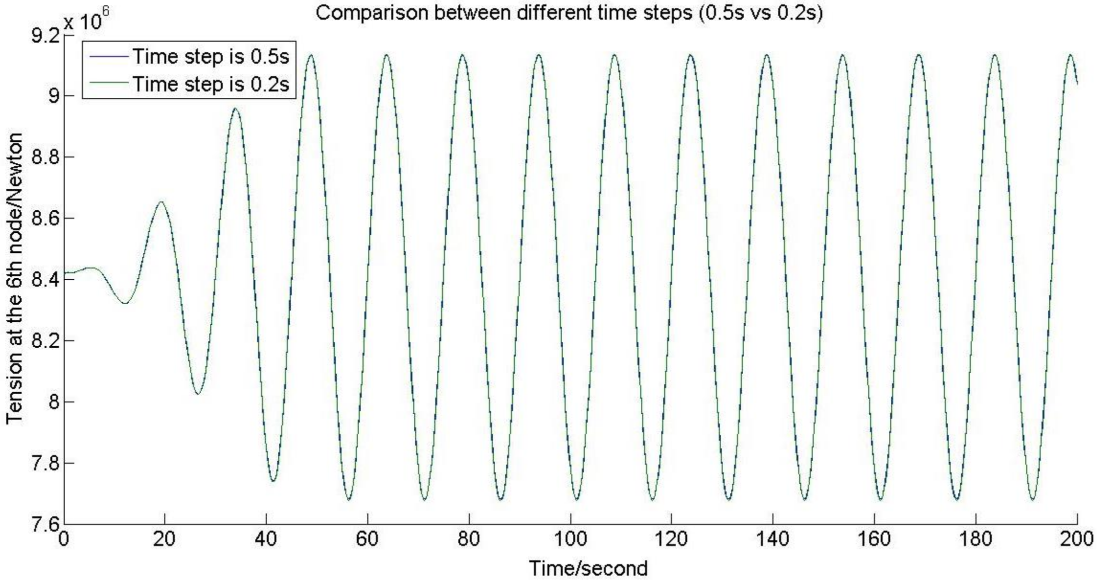

Fig. 4.4 Tension of the 6th node with times steps of 0.2s and 0.5s, in heave motion.

Fig. 4.4 shows the tension time history at the 6th node. It is observed that the two simulations of different time steps are virtually identical. The amplitude of the tension reaches about 700 kN, which is consistent with the tension-stroke relationship of the tensioner system. The tensioner system stiffness is about 365 kN/m and the stroke is about 2 meters in this case, which is approximately the heave motion amplitude, therefore it can be easily estimated that the force caused by the stroke of tensioner agrees reasonably well with the amplitude of tension time series.

The second case is involved with a harmonic excitation at the upper deck in surge direction with the amplitude of 40m and period of 200s. Again, two different time steps 0.5s and 0.2s were used, respectively. The tension at the 6th node was traced. The results obtained using the two different time steps are the same (See Fig. 4.5). The simulation shown in this figure only lasts for 200 seconds for the purpose of comparison. Simulation lasting 1000 seconds will be presented in subsection 4.1.2.2.

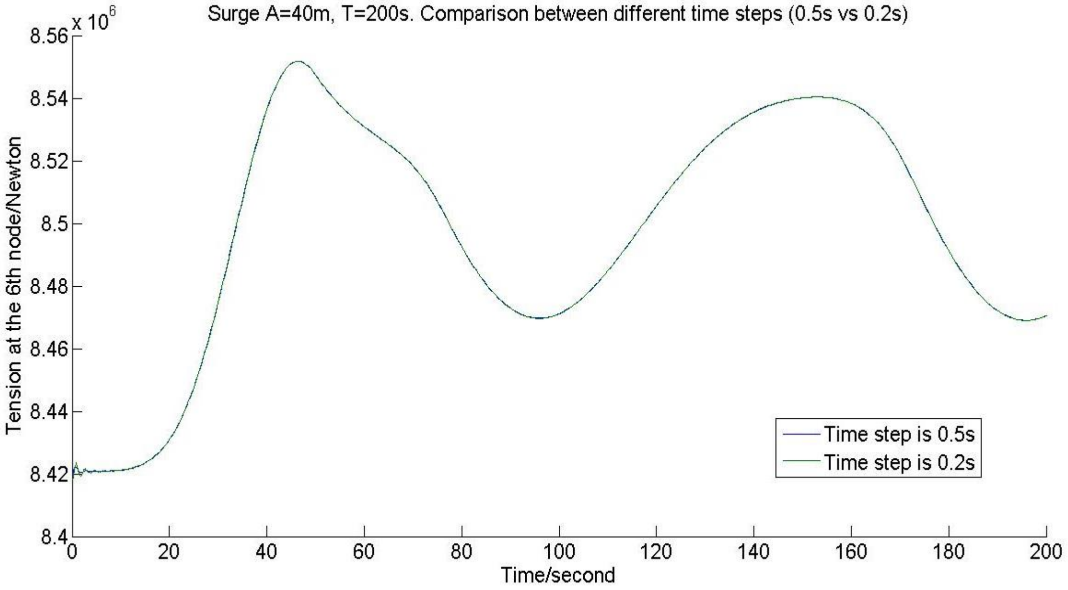

Fig. 4.5 Tension of the 6th node with times steps of 0.2s and 0.5s, in surge motion

4.1.2.2 Analysis of Motion in Surge/Sway/Heave Direction

Several cases are tested to demonstrate the resilience and robustness of the updated CABLE3D. The case for the TTR experiencing a harmonic excitation in surge direction, with the amplitude of 40m and period of 200 seconds, which represents a slow drift motion, is simulated (See Fig. 4.6). The top graph of Fig. 4.6 shows the x-coordinate (horizontal direction) of the 6th node as a function of time. As discussed before, the 6th node is the node where the tensioner system is attached. The middle graph reveals the time series of y-coordinate of that node. Though the amplitude of surge motion reaches 40 meters, the amplitude of y coordinate is merely about 0.1 meter. The bottom graph presents the time series of tension at the 6th node and the amplitude is approximately 40 kN, which is much smaller than the tension amplitude of heave motion shown in last subsection.

Also, it is found that the tension at the 6th node is closely related to its y-coordinate. However, both the tension and y-direction motion have almost the double frequency as the x-direction motion. When the horizontal offset reaches the maximum, its y-coordinate becomes the lowest; when the x-coordinate reaches the equilibrium position, the y-coordinate becomes the highest; when the horizontal offset reaches maximum at the other side, its y-coordinate again becomes the lowest. Thus one period motion in the x-direction corresponds to two periods in the y-direction motion. Ramp function lasting for 50 seconds is used in the simulation, and it is noted that the motion in the first 50 seconds is not in the harmonic state.

The harmonic excitation in surge direction with the amplitude of 3m and period of 15s is also examined (See Fig. 4.7). Similar observation as in the previous case are made here and both amplitudes of y-coordinate and tension are much smaller than those in the last case of slow drift motion. The major period of the y-direction motion is one half of that of the x direction motion. After ramp function the oscillation of y-coordinate becomes fully developed and the mean value at this stage is smaller than the initial y-coordinate. This is due to the lateral hydrodynamic force caused by the translation of the riser. What's more, when the riser passes through the mean position, the translation velocity reaches the highest and induces the largest hydrodynamic loads within one cycle. This force makes the riser bending and lowers the y-coordinate of the 6th node. The y-coordinate is related to tension, thus correspondingly the mean tension at the fully-developed stage is larger than the initial tension.

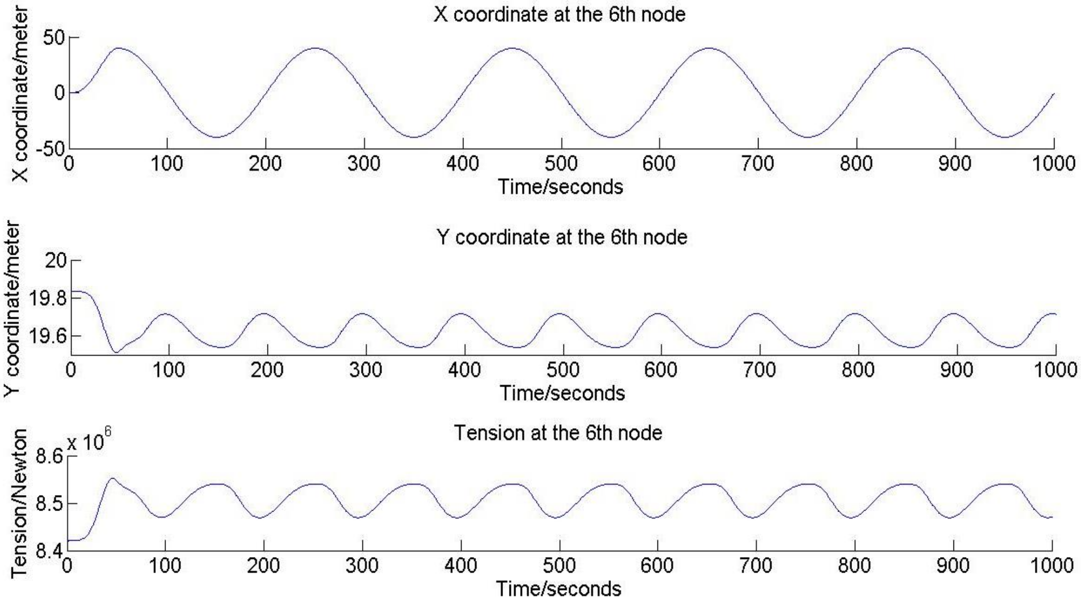

Fig. 4.6 Surge excitation with amplitude of 40m and period of 200s

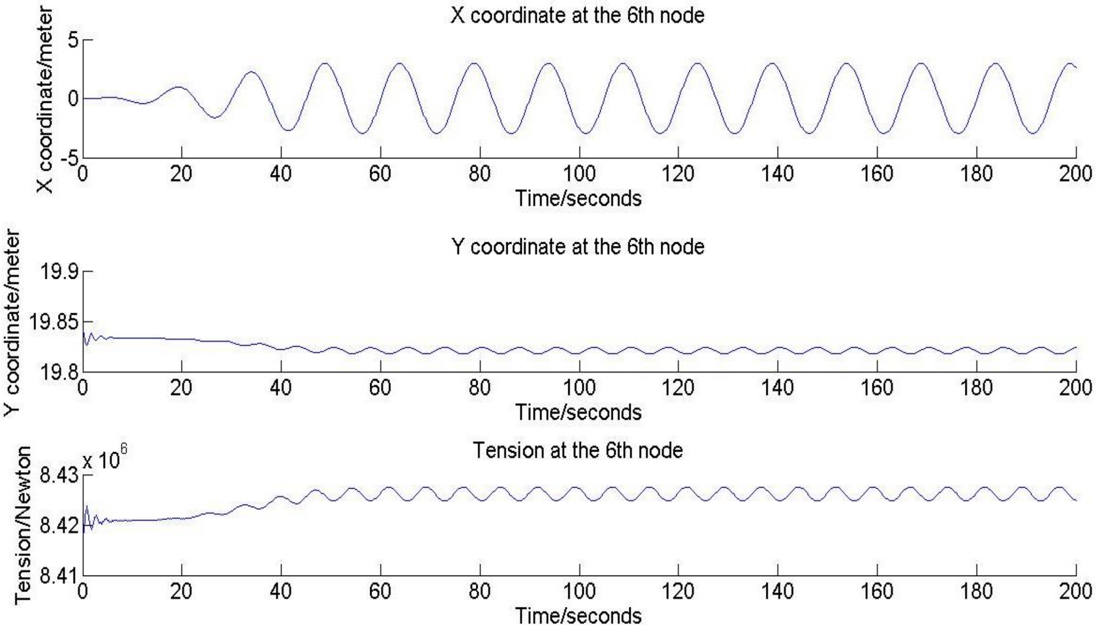

Fig. 4.7 Surge excitation with amplitude of 3m and period of 15s

As shown in Fig. 4.8, the case of the harmonic excitation at the upper end of the TTR in heave direction with the amplitude of 2m and period of 15s is presented. The top graph represents the trend of the y coordinate of the upper end. The middle one shows the y coordinate of the 6th node. The bottom one shows the time series of tension at the 6th node. The tension amplitude reaches as high as 700 kN, which is much larger than the tension amplitude in the case of large-amplitude slow drift surge motion. It indicates that the heave motion is the most critical to the tensioner system. If the heave amplitude is large, the tensioner system will experience large stroke, which is dangerous to the safe operations of TTRs.

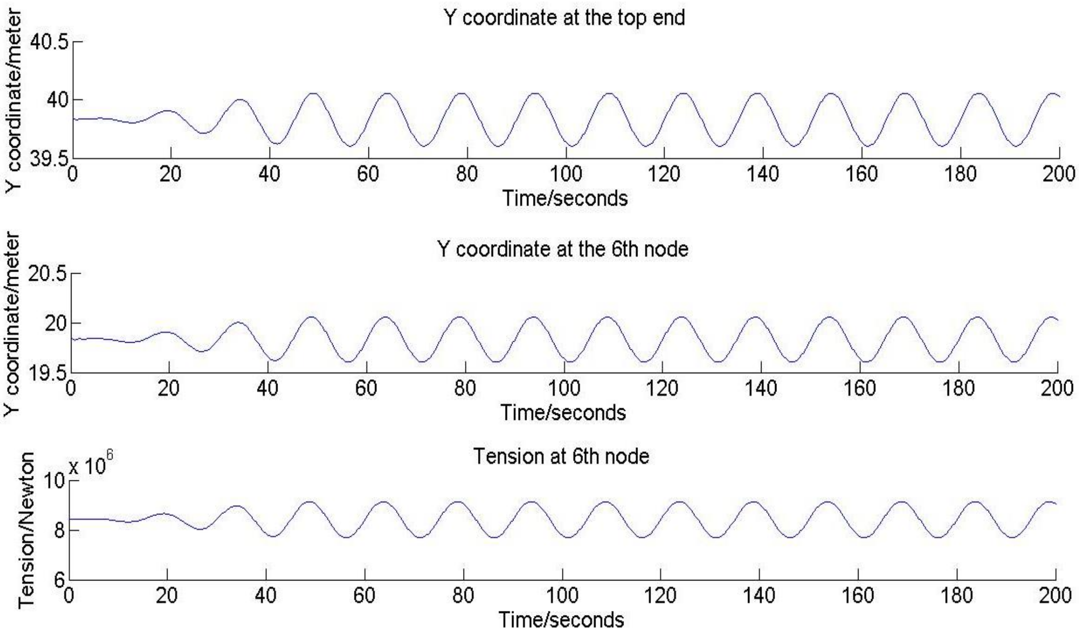

Fig. 4.8 Heave excitation with amplitude of 2m and period of 15s.

Fig. 4.9 presents the case of the harmonic excitation in sway direction with the amplitude of 40m and period of 200s, which represents the transverse slow drift motion (in z-direction). The top graph shows how the y-coordinate of the 6th node is changing with time. The middle graph shows the z-coordinate of the 6th node, and the bottom graph shows the tension at the 6th node. The trends observed in Fig. 4.9 are similar to those observed in the excitation in surge direction (Fig. 4.6).

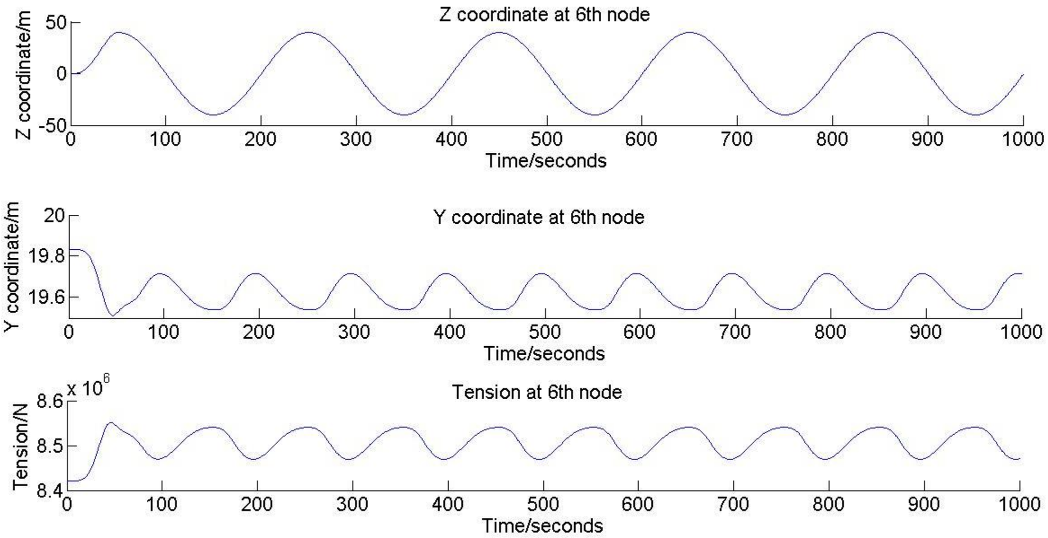

Fig. 4.9 Sway excitation with amplitude of 40m and period of 200s

4.1.2.3 Specific Analysis of Tension and Bending Moment

To observe the tension and bending moment distribution along a TTR, the results of the excitation with the amplitude of 40 m and period of 200s in surge direction are presented. The motion was simulated for duration of 1000 seconds. The motion, tension and bending moment at two different nodes (6^{th} and 15^{th} node) were analyzed, which could be found in Fig. 4.6 and Fig. 4.10, respectively. The two nodes show similar trends in both motion and tension. At the 15^{th} node which is 51 meters below the water surface, the y coordinate amplitude is 0.1 meter and tension amplitude is about 40 kN. The amplitude values are almost the same with those at the 6^{th} node.

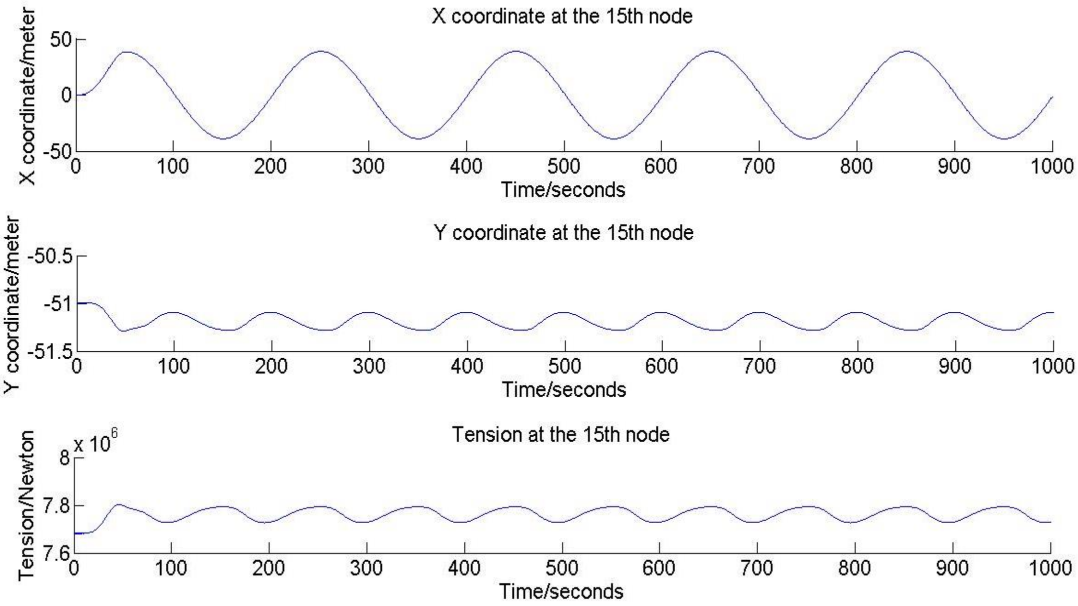

Fig. 4.10 Surge excitation with amplitude of 40m and period of 200s at 15^{th} node

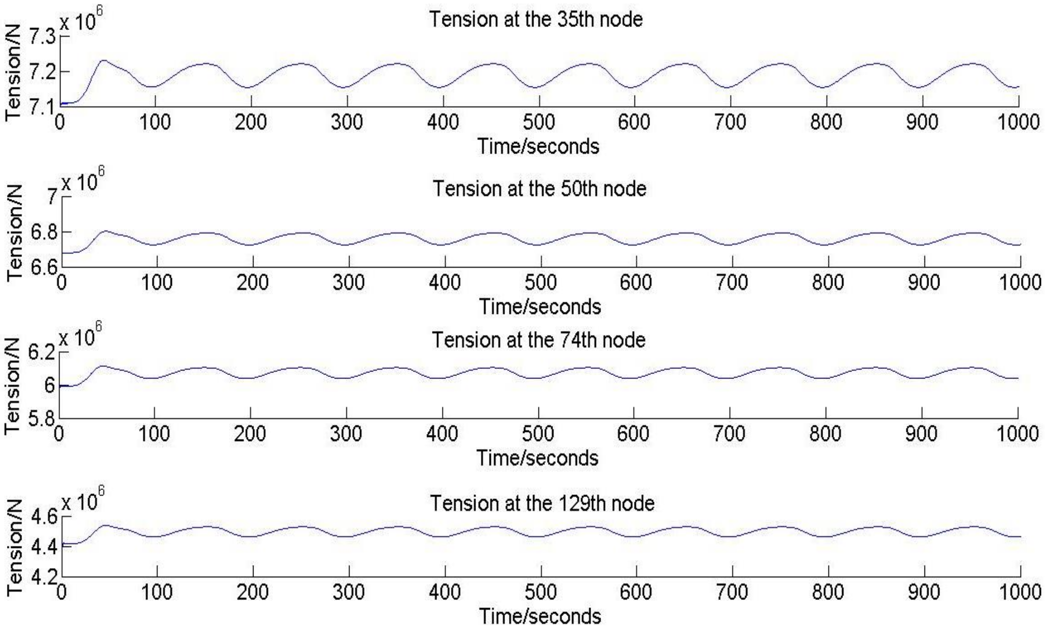
Tension at the 35th node

Tension at the 50th node

Tension at the 74th node

Tension at the 129th node

Fig. 4.11 Tension at nodes 300m, 495m, 800m, and 1498m below the sea surface

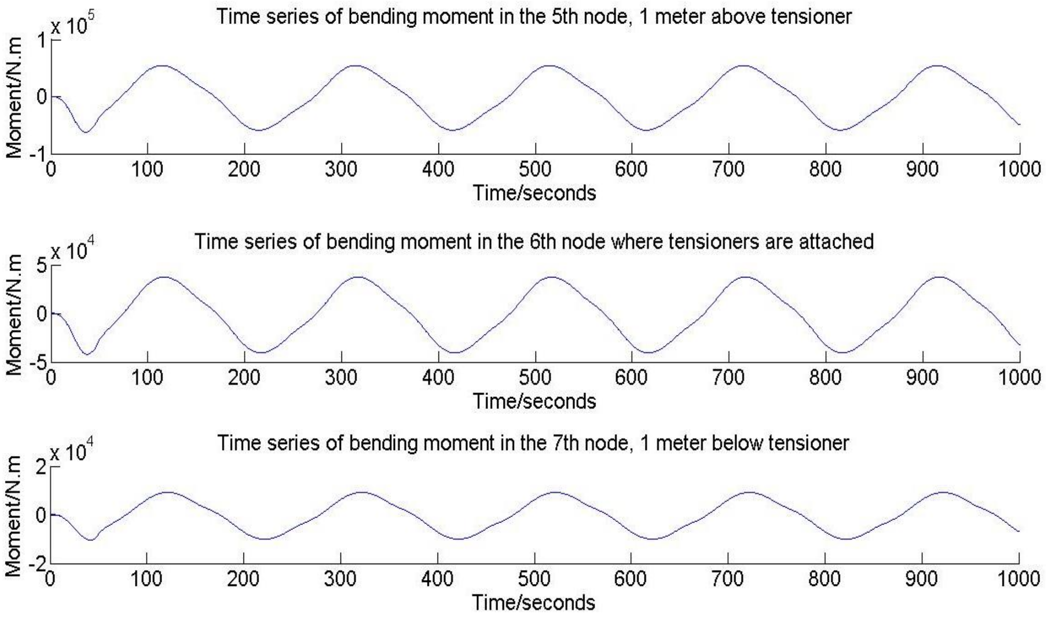
Time series of bending moment in the 5th node, 1 meter above tensioner

Time series of bending moment in the 6th node where tensioners are attached

Time series of bending moment in the 7th node, 1 meter below tensioner

Fig. 4.12 Time series of bending moment of nodes near upper deck and tensioner

The time series of the tensions at four different nodes (35th, 50th, 74th and 129th node) are presented in Fig. 4.11. The four nodes are at the depth of 300m, 495m, 800m and 1498m, respectively. The phases of the tension are quite synchronized at different depths. The tension amplitude which is related to dynamic tension is also almost the same.

Fig. 4.12 shows the bending moment at the 5th, 6th and 7th node, respectively, which located at the vicinity of the upper deck and the tensioner system. It is revealed that the bending moment in the elements near the upper deck (5th node) reaches the highest level. Since the bending moment corresponds to the magnitude of curvature, it is known that the largest curvature happens near the tensioner system. Riser guide has not been considered in this case. After adding the constraints of riser guides, the peak value of dynamic bending moment will appear at the lowest riser guide according to further study considering riser guides that will be included in the subsection 4.1.2.4.

4.1.2.4 Effects of Riser Guide

To restrict relative motion between TTRs and the hull, the riser guides are required such as in the cases of TLP or SPAR. To quantify the effects of riser guides, three riser guides are modeled in the case illustrated in subsection 3.1. The vertical distances from the three riser guides to the upper deck are 110 meters, 137 meters and 165 meters, respectively.

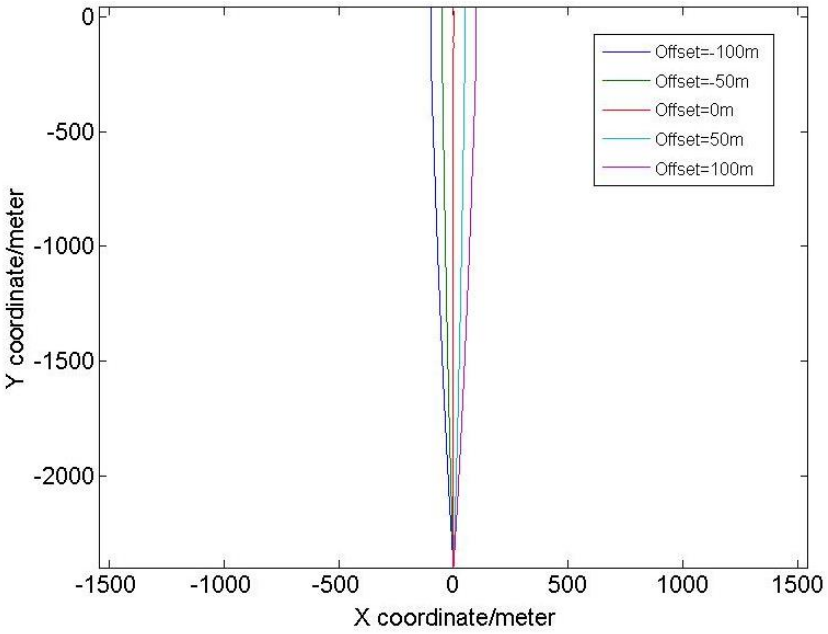

Fig. 4.13 TTR configuration with different offsets when riser guide is considered

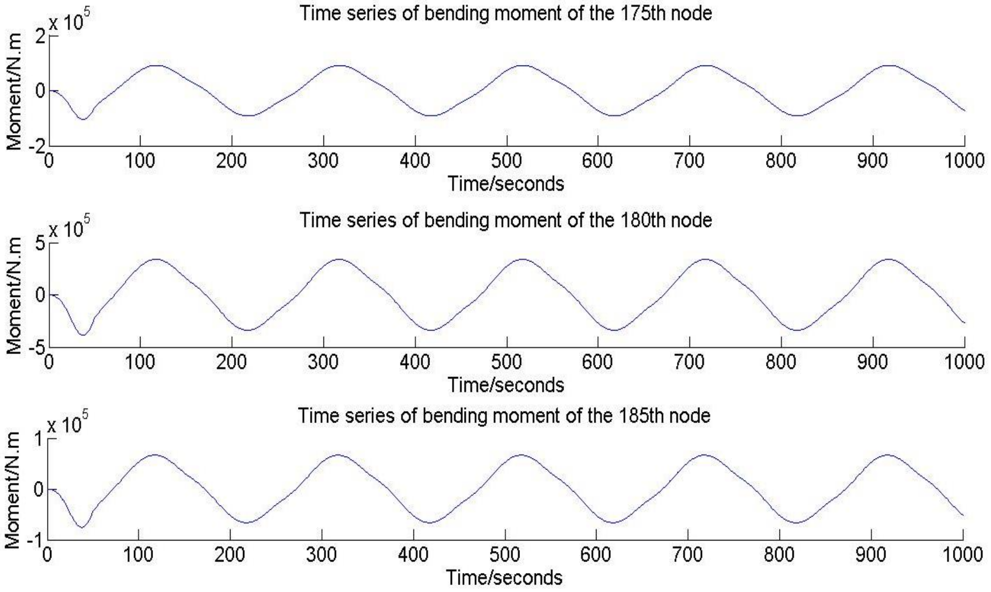

Fig. 4.14 Dynamic bending moment time series at the 175th, 180th, 185th node

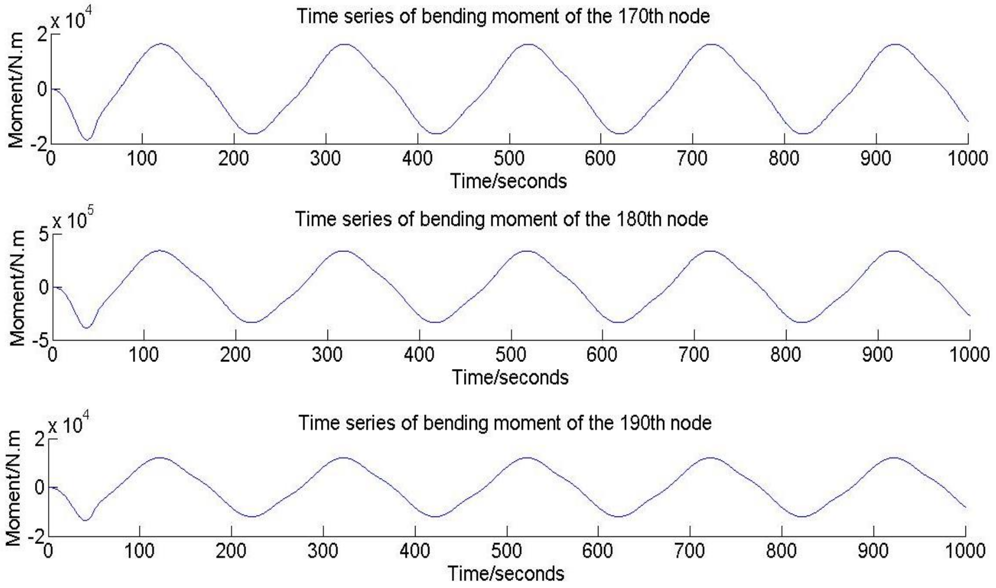

Fig. 4.15 Dynamic bending moment time series at the 170th, 180th, 190th node

The surge motion of the Spar experiencing the offset of -100 meters, -50 meters, 0 meter, 50 meters and 100 meters are studied. As shown in Fig.4.13, the TTR section above the keel guide (about 140m below the sea surface) inside the moon pool remains vertical due to the restrictions of the three riser guides. The maximum curvature takes place in the vicinity of the keel guide, which means the maximum bending moment is likely to occur at this place. Further analysis reveals the dynamic bending moment in the neighborhood of the keel guide.

To quantify the dynamic bending moment, the Spar is assumed to experience a slow drift motion with amplitude of 40 meters and period of 200 seconds. To ensure high accuracy, fine elements are adopted in this case. The keel guide locates at the 180th node, which is about 139 meters below the sea surface. The bending moments at 160th node, 165th node, 170th node, 175th node, 180th node, 185th node, 190th node, 195th node, 200th node, and 205th node are computed. These nodes locate at 119 meters, 124 meters, 129 meters, 134 meters, 139 meters, 144 meters, 149 meters, 154 meters, 159 meters, 164 meters below the sea surface, respectively. These ten nodes chosen here are in the vicinity of keel guide.

Fig. 4.14 indicates that the maximum dynamic bending moment amplitude occurs at the 180th node, where the keel guide locates. The amplitude reaches as high as 400 kN.m. However, at the 175th node and the 185th node, which locate at 5 meters above and below the keel guide, respectively, the peak bending moment diminishes to below 100 kN.m, which is far less than the dynamic bending moment at the keel guide. Although the magnitude is different, the phases of the bending moment are quite synchronized along nodes at different depths.

The amplitude of the dynamic bending moment further decreases to below 20 kN.m at 170th node and 190th node, which are 10 meters above and below keel guide, respectively (See Fig. 4.15). The further away from the keel guide the location is, the smaller the dynamic bending moment at that point will be. At 205th node, which is 25 meters below the keel guide, the maximum dynamic bending moment is only 3 kN.m, which is negligible compared to that at the keel guide. Thus the vicinity of keel guide is more likely to experience high dynamic bending moment, and fatigue analysis within this area is of great significance to the design.

4.2 Analysis of SCR

4.2.1 Static Analysis of A SCR with A Flex Joint at its Porch

At first, the computation of the equilibrium position of a static SCR is attempted through iterations. During the iteration, the horizontal excursion of the SCR varies until the top angle of the riser with respect to the vertical line is close to the 15 degrees, which is the neutral angle of the flex joint used in the study. In our simulation, the riser top angle is obtained at 14.85 degrees with respect to the vertical line when the horizontal excursion is 635m. After the equilibrium position is obtained, several cases with different offset values are calculated using the static subroutine in CABLE3D. The results related to the offsets of -100m, -80m, -60m, -40m, -20m, 20m, 40m, 60m, 80m, 100m are depicted in Fig.4.16. The touch-down point varies with different fairlead offset values.

Fig.4.17 illustrates the relationship between the offsets and bending moment provided by the flex joint. When the offset is zero, which is the equilibrium position, the bending moment at the porch is almost zero. When the offset to the right gets larger, it is expected that the bending moment becomes larger, which reaches about 300 $kN \cdot m$ as the offset value is 100 meters.

The larger the right-going offset is, the larger the top angle with respect to the vertical line will be (See Fig. 4.18). The comparison between a hinged riser and the same riser but with a flex joint at the porch qualitatively validates the numerical scheme developed in this study. Since the flex joint exerts a moment on the upper end of the riser, the top angle of the riser is restricted and becomes smaller as indicated in Fig. 4.18. However, the reduction of top angle is very limited. When the offset reaches as large as 100m, which could only occur in extremely harsh sea conditions, the reduction of top angle with respect to the hinged boundary condition is 0.5 degree, which is not significant. The reduction merely accounts for 10 percent of the angle between riser top end and neutral angle. The effects of flex joint on bending moment along the SCR will be discussed in the later subsection.

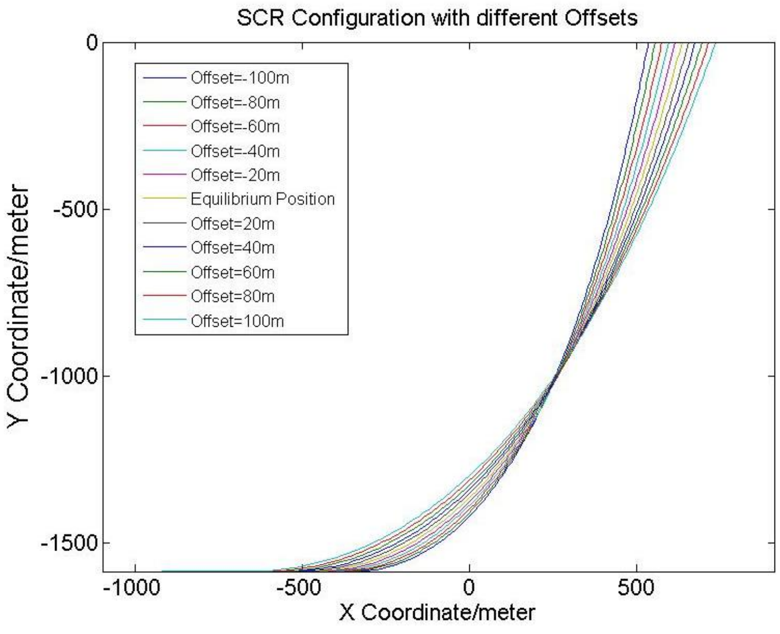

Fig. 4.16 SCR with flex joint installed at its porch under different offsets

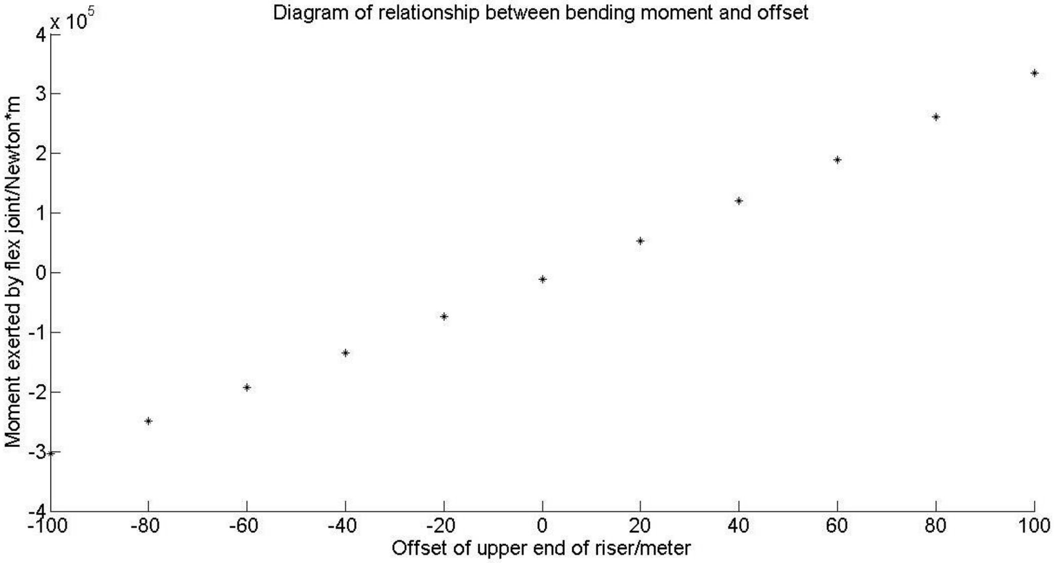

Fig. 4.17 Relationship between bending moment and offset

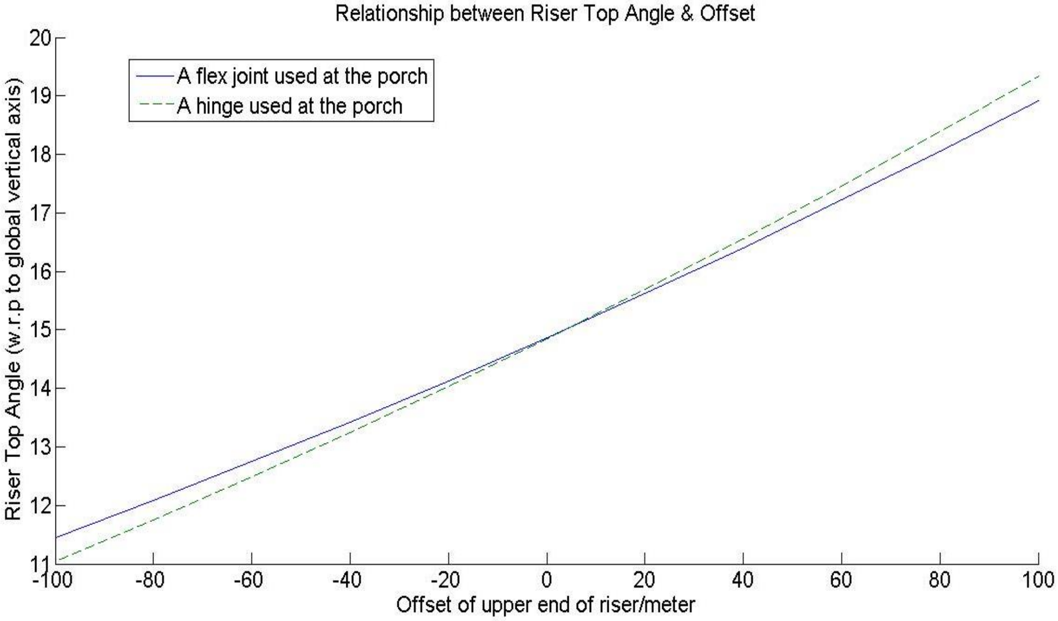

Fig. 4.18 Relationship between the SCR top angle and offsets with/without the flex joint

4.2.2 Dynamic Analysis of Design Case in GoM

Various dynamic analysis cases were performed to analyze a SCR with flex joints under different harmonic excitations at its porch. As cases of TTRs, the ramp function is applied at the beginning of each simulation. The duration of ramp function varies with the period of excitation from 5s to 200s.

4.2.2.1 Results Using Different Sizes of Time Steps

In this subsection, different sizes of time steps are used to explore the resilience and robustness of the program. Two cases are examined here. The first is a harmonic excitation with period of 5s and amplitude of 1m in the surge direction. The second is the harmonic excitation of a period of 15s and amplitude of 3m also in surge direction. The surge motion is forced at the upper end of the riser and the time series of its top angle with respect to the vertical line is the output. Three time steps 1.0s, 0.5s and 0.2s are tested. As shown in Fig.4.19, the results of two time steps (0.2 s and 0.5 s) are almost identical. In the top panel of Fig. 4.19, when the period is short (5 s), the largest time step (1 s) results in relatively large error. Therefore, in later simulations, the time step of 0.25 s is chosen to ensure accuracy.

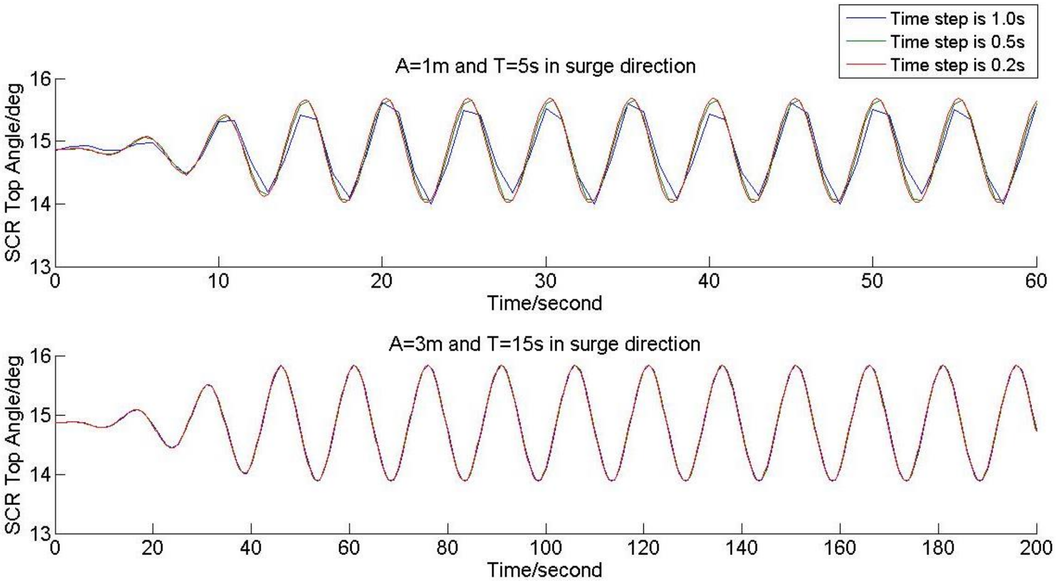

Fig. 4.19 Verification of different time steps under two harmonic excitations at upper end.

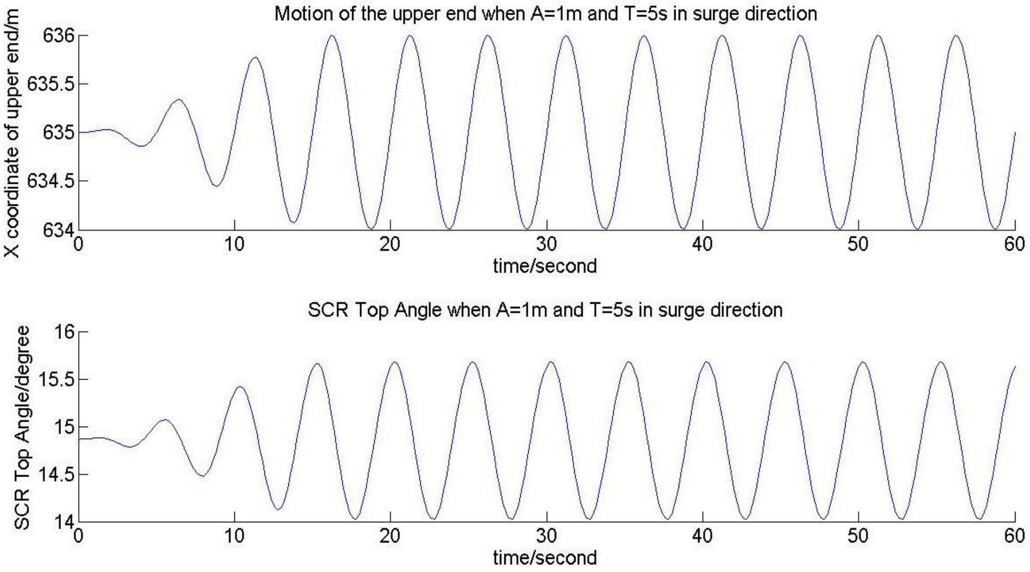

Fig. 4.20 Surge excitation with amplitude of 1m and period of 5s.

4.2.2.2 Analysis of Motion due to Different Direction Excitations

The Fig.4.20 shows the top angle of the riser when its upper end is forced to move in the surge direction with the amplitude of 1m and period of 5s. The top angle has the same period with the forced motion, which is expected. However, there is a phase difference between the top angle and the related excitation. The top angle has a phase advance compared to forced motion. Fig.4.21 depicts the similar plots but the forced surge motion has the amplitude of 3m and period of 15s. Yet while the upper end of riser experiences a slow drift motion with the amplitude of 40m and period of 200s, it is observed that the top angle time series is not exactly in harmonic with the forced motion (See Fig. 4.22).

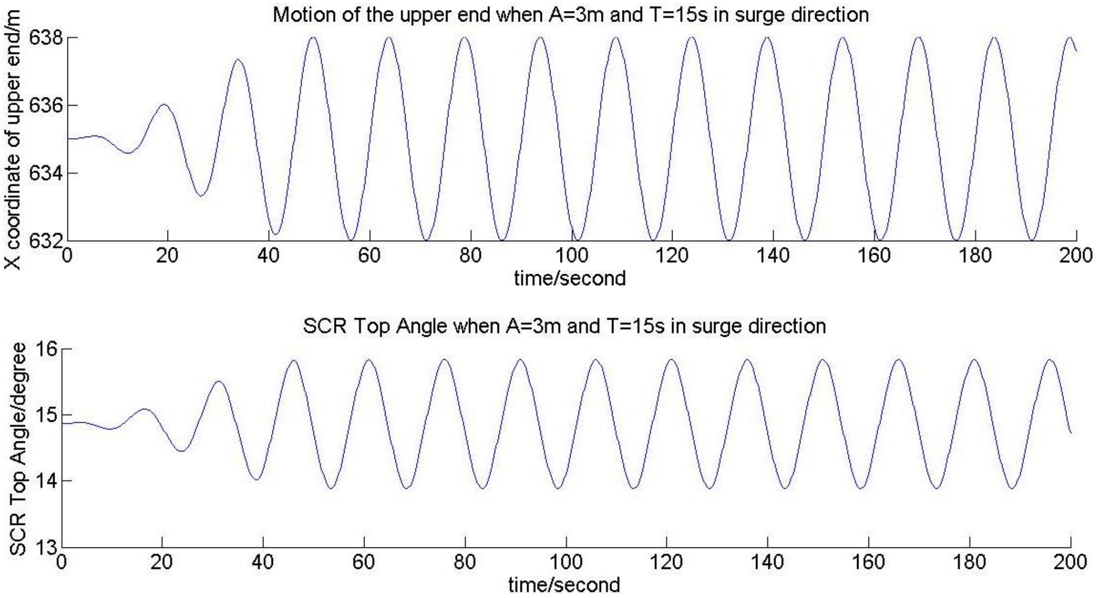

Fig. 4.21 Surge excitation with amplitude of 3m and period of 15s.

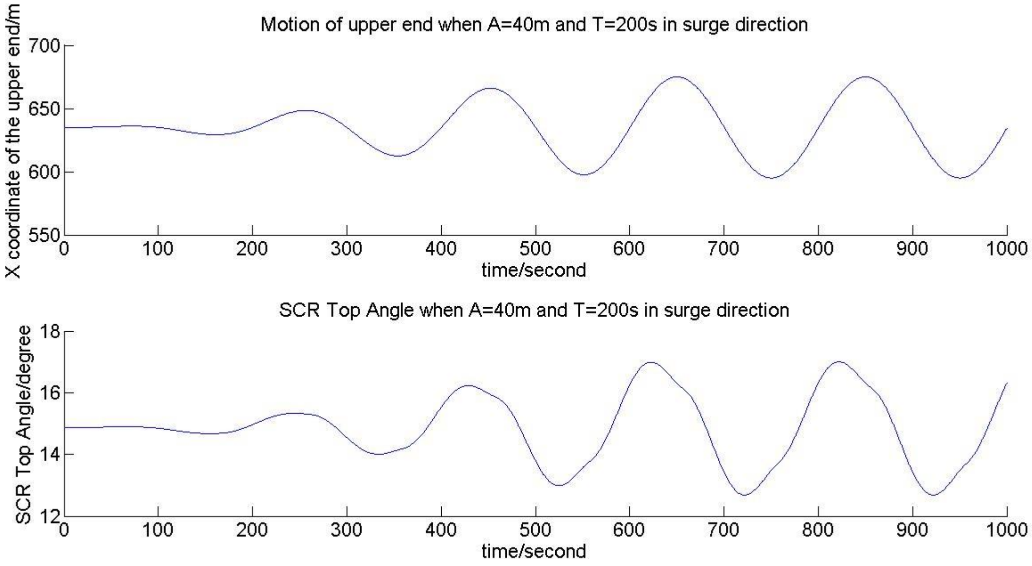

Motion of upper end when A=40m and T=200s in surge direction

SCR Top Angle when A=40m and T=200s in surge direction

Fig. 4.22 Surge excitation with amplitude of 40m and period of 200s.

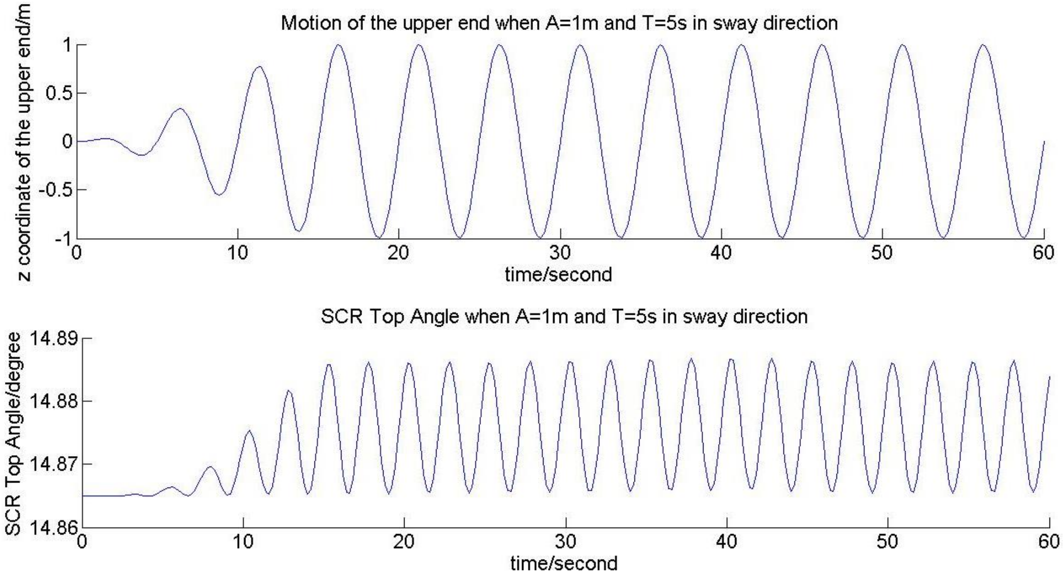

Motion of the upper end when A=1m and T=5s in sway direction

SCR Top Angle when A=1m and T=5s in sway direction

Fig. 4.23 Sway excitation with the amplitude of 1m and period of 5s

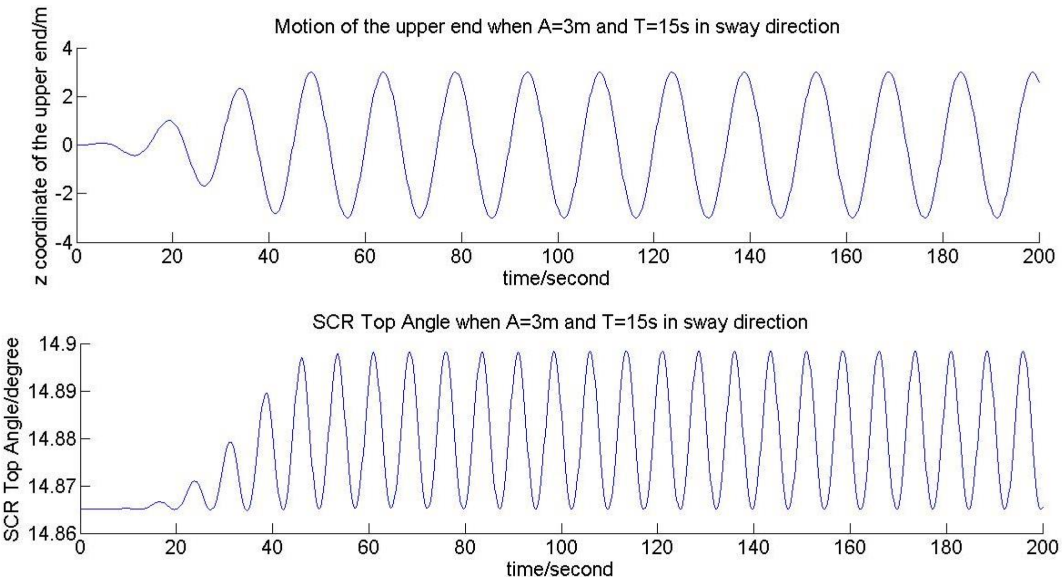

Fig. 4.24 Sway excitation with the amplitude of 3m and period of 15s

Fig.4.23 depicts the top angle of the riser when its upper end is excited in the sway direction with the amplitude of 1m and period of 5s. It is observed that the frequency of the change in the top angle is doubled in comparison with that of the related excitation. The same trend is also observed in Fig.4.24, which reveals the results due to the excitation in sway direction with the amplitude of 3m and period of 15s. When the sway offset reaches the maximum, the top angle becomes the maximum. After one quarter of the period of the sway excitation, the upper end of the riser returns to its equilibrium position (zero offset at the upper end), the top angle reaches its minimum. After a half of the sway period, the sway offset at the upper end reaches the maximum when it sways to the opposite side and the top angle again reaches the maximum. This is why one period of the sway motion corresponds to two periods of the change in the top angle.

4.2.2.3 Effects of Flex Joints

Fig.4.25 and Fig. 4.26 reveal the tension and bending moment at the upper end when the two different surge excitations are forced at the upper end, respectively. In Fig. 4.25, the excitation is of the amplitude of 1m and period of 5s, while in Fig. 4.26 it is of the amplitude of 3m and period of 15s. The moment is dominated by the magnitude of the top angle thus their phases are quite synchronized. The phase of tension series is even more advanced than phase of moment. The response of risers under irregular excitations is to be analyzed in subsection 5.2.5 after integrating CABLE3D into COUPLE.

Then the comparison of the top angle between a hinge used at the porch and a flex joint used there is conducted (See Fig. 4.27). The comparison reveals that the flex joint reduces the magnitude of the changes in the top angle, which is expected based on our intuition. The reduction is about 10 percent of the original top angle when a hinged condition is considered and this is consistent with what is drawn in static analysis.

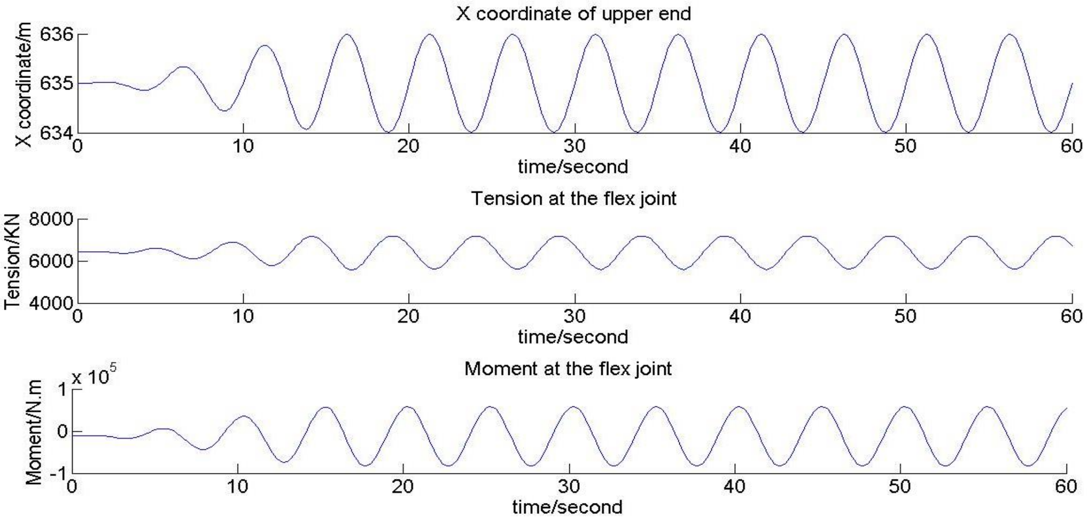

Fig. 4.25 Surge excitation with amplitude of 1m and period of 5s

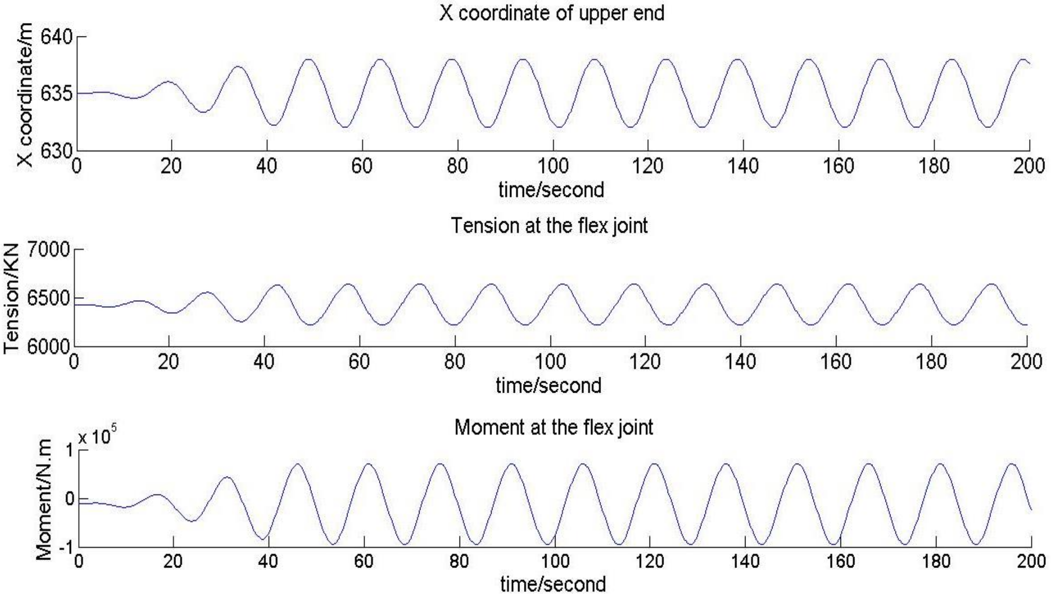

Fig. 4.26 Surge excitation with amplitude of 3m and period of 15s

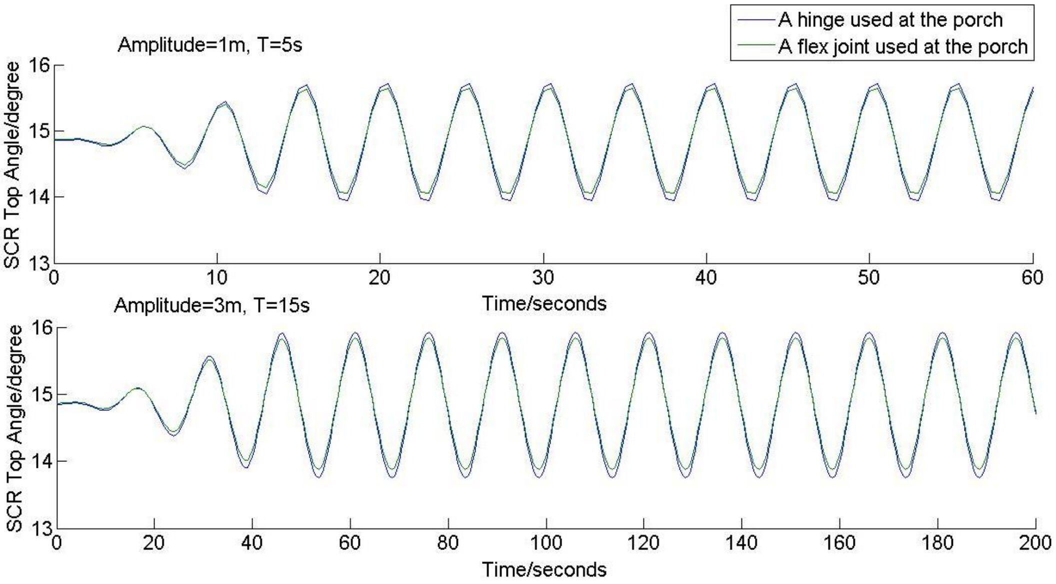

Fig. 4.27 Comparison between a hinge used at the porch and the flex-joint used there

5. APPLICATION

5.1 Analysis Background

The up-dated CABLE3D is integrated into COUPLE, making it applicable to the analysis of a floating system consisting of a Spar, its mooring system, SCRs and TTRs. The case of 'Constitution' Truss Spar is selected to be analyzed.

5.1.1 Introduction of 'Constitution' Truss Spar

Based on the information provided by Li (2012), the Anadarko 'Constitution' Spar consists of four major components: topsides, hull, moorings, and risers.

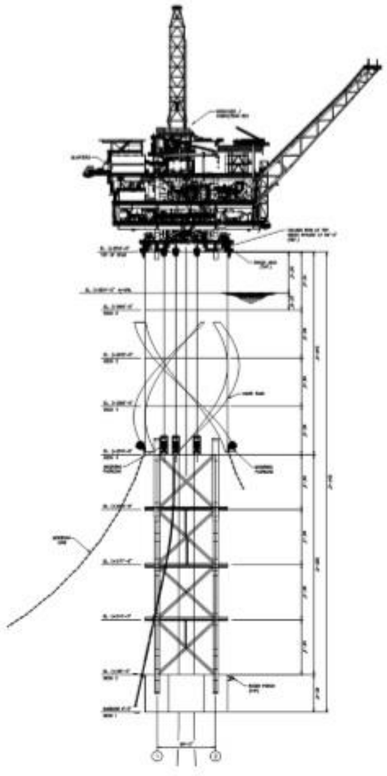

Fig. 5.1 Configuration of 'Constitution' Spar

Table 5.1 Main characteristics of the Spar

Properties	Units	Value
Water Depth	m	1524
Draft	m	154
Center of Buoyancy from Keel	m	112.34
Center of Gravity from Keel	m	91.27
Topside Payloads	ton	10770
Hull Weights	ton	14800
Total Displacement	ton	59250
Hard Tank Diameter	m	30
Length Overall	m	169
Hard Tank Length	m	74
Soft Tank Length	m	14
Truss Length	m	81
Truss Spacing	m	20
Fairlead Location from Keel	m	98

The hull consists of the three main parts from the top to the bottom: hard tank, truss, and soft tank, which have lengths of 74m, 81m, and 14m, respectively. The configuration of ‘Constitution’ is depicted in Fig. 5.1, which is cited from the drawings offered by Anadarko Corporation. The characteristics of the truss Spar are given in Table 5.1.

5.1.2 Mooring Line and Riser Properties

The mooring system of ‘Constitution’ includes three groups, each of which has three mooring lines. Each mooring line section has three segments: platform chain, mid-section cable, and ground chain. The mooring line fairleads are located at the hard tank section, which is about 55.6 meters below the sea surface. The riser system consists of 2

SCRs and 6 TTRs. The physical properties of mooring lines and SCRs are listed in Table 5.2 and Table 5.3 respectively. The distribution of mooring system and riser system is shown in Fig. 5.2, and the configuration of mooring lines and SCRs are depicted in Fig. 5.3 and Fig. 5.4 respectively. Based on drawings, the coordinates of fairleads of mooring lines, porches of SCRs and upper end of TTRs are presented in Table 5.4.

The detailed physical properties of TTR are not available to the author, but it could be concluded that double-casing risers are used in ‘Constitution’ due to the fact that only double-casing risers could be applied in this ultra-deep water condition. Thus the physical properties of TTRs are the same with TTRs described in the subsection 3.1 and in Table 3.1.

Table 5.2 Mooring line properties

	Platform Chain	Mid-section	Ground Chain	Units
Line Type	R4 Studless	Steel Wire	R4 Studless	
Equivalent Diameter	0.142	0.127	0.142	m
Jacket Thickness		0.011		m
Weight in Air	3949.4	823.2	3949.4	N/m
Weight in Water	3439.8	646.8	3439.8	N/m
EA	152,957	151,020	152,957	ton

Table 5.3 SCR properties

	SCR #1	SCR #2	Units
Length	1706.88	1706.88	m
Diameter	0.254	0.3048	m
Dry Weight	561.54	958.4	kg/m
Unit Buoyancy	511.46	736.5	kg/m

Table 5.4 The coordinates of upper ends of nine mooring lines, two SCRs and six TTRs

Mooring Line/Riser	X(m)	Y(m)	Z(m)
Mooring Line # 1	14.49	3.61	-55.6
Mooring Line # 2	14.48	-3.64	-55.6
Mooring Line # 3	12.8	-7.69	-55.6
Mooring Line # 4	-3.64	-14.48	-55.6
Mooring Line # 5	-7.69	-12.8	-55.6
Mooring Line # 6	-12.8	-7.69	-55.6
Mooring Line # 7	-12.8	7.69	-55.6
Mooring Line # 8	-7.69	12.8	-55.6
Mooring Line # 9	-3.64	14.48	-55.6
SCR #1	5.11	-14.03	-140
SCR #2	6.31	-13.54	-140
TTR #1	4.88	2.44	20
TTR #2	0	2.44	20
TTR #3	-4.88	2.44	20
TTR #4	-4.88	-2.44	20
TTR #5	0	-2.44	20
TTR #6	4.88	-2.44	20

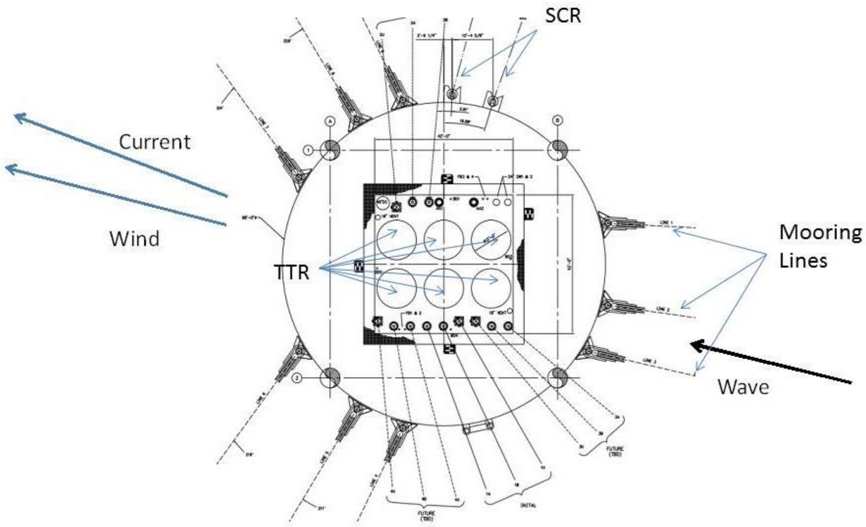

Fig. 5.2 Distribution of mooring lines and risers and headings of wave, wind and current

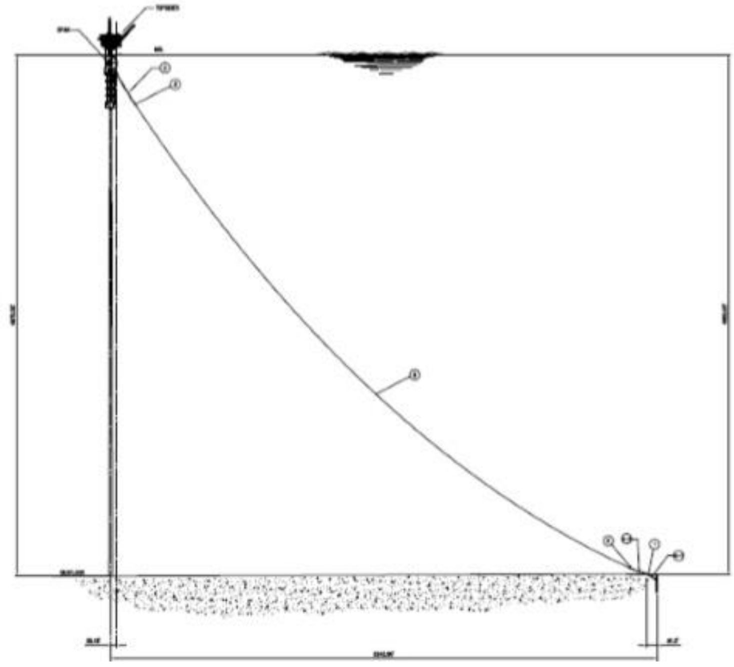

Fig. 5.3 A mooring line configuration

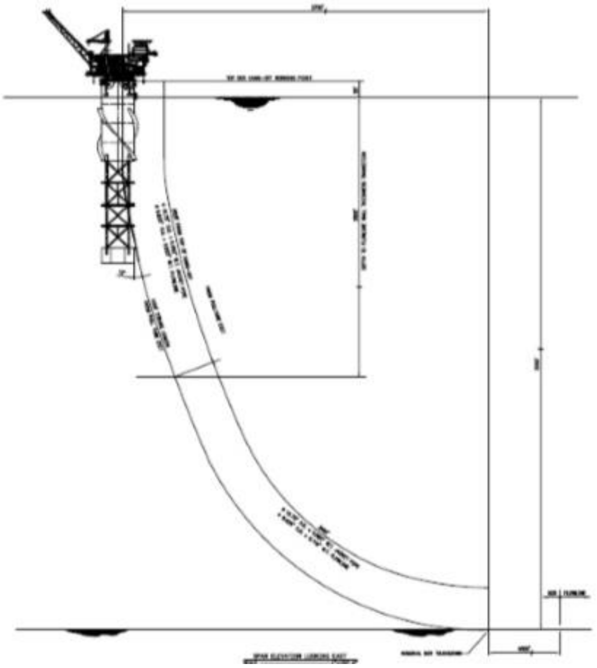

Fig. 5.4 A SCR configuration

Because no details were provided on how the TTRs of ‘Constitution’ were tensioned, we exercised both cases, that is, TTRs tensioned by tensioner systems and TTRs tensioned by buoyancy cans. For both cases, several assumptions are made. The top tension is approximated as 1.5 times of the net dry weight of individual TTR. If the top tension is provided by deck mounted hydropneumatic tensioner systems, the approximate tension of each tensioner is 1650kN. The tensioner system stiffness is exactly the same as the case in 3.1. This assumption is valid due to the same type of risers adopted in these two cases. Four tensioners are assumed to be used in a tensioner system for each TTR. If TTRs with buoyancy cans are modeled, the cans are assumed to be attached to the TTR segments within the moon pool and the buoyancy is to be distributed to every elements of this segment.

In the numerical simulation, flex joints are considered to be used at the upper ends of the two SCRs and the bottom ends of the six TTRs. The rotational stiffness of SCR flex joints is chosen as $2\times10^6\ {}^{N\cdot m}\!/_{rad}$ and stiffness of TTR bottom flex joints is also selected as $2\times10^6\ {}^{N\cdot m}\!/_{rad}$. The actual values for rotational stiffness of flex joints used on ‘Constitution’ are not available, thus stiffness values are estimated based on the information provided by Deka *et al.* (2010).

5.1.3 Estimation of Hydrodynamic Coefficients

Magee *et al.* (2000), Prislin *et al.* (2005) and Theckumprath (2006) attempted to quantify the hydrodynamic coefficients of the Spar and the other main sections. These coefficients are also used in our simulation (See Table 5.5). The drag coefficient and added-mass coefficients of the mooring system have been supplied by Anadarko Petroleum Corporation.

Table 5.5 Hydrodynamic coefficients

	Hydrodynamic Coefficient	
Spar Sections	Added-mass Coefficient	Drag Coefficient
Hard Tank	1	1.2
Truss Members	0.8	1
Soft Tank	1	1.2
Heave Plate	2	6
Mooring Chain	2	2.4
Mooring Wire	1	1.2

In computing current loads on a TTR, it is considered that the whole portion of the TTR below water surface is exposed to the current. However, when TTRs were installed inside a Spar, certain segments of TTR were inside the moon pool of hard tank and soft tank thus they were protected from the hydrodynamic loads due to relative motion between a TTR and ambient fluid. Following the Morrison Equation, the added-mass force and drag force acting on 6 TTRs are approximated and summed. This amount of extra forces caused by TTRs is then subtracted from the related forces acting on the Spar to eliminate the redundancy of computing them. In our calculations, equivalent added mass coefficient of 1.0 and equivalent drag coefficient of 1.12 for the hard tank and soft tank are adopted.

5.1.4 Met-ocean Conditions of Hurricane 'Ike'

The hurricane 'Ike' has been selected in the coupled dynamic analysis. This hurricane occurred on September 12th, 2008. According to Li (2012), the peak of 'Ike' went past 'Constitution' from 00:00am to 01:00am on September 12th, 2008. The direction and magnitude of the wind, wave and current are presented in Table 5.6 and visual expression of their headings is plotted in Fig. 5.2. The current velocity as a function of depth is shown in Table 5.6 and Fig. 5.5 (Li, 2012).

Table 5.6 Met-ocean data of hurricane 'Ike'

Load	Parameters	Units	Hurricane 'Ike'
Wave	Spectrum Type		JONSWAP
	Significant Height	meter	9.30
	Peak Period	second	14.84
	Shape Factor		2.20
	Heading	degree	170.00
Wind	Spectrum Type		API
	Speed	m/s	37.40
	Heading	degree	170.00
Current	Heading	degree	164.00
	Depth-Speed	m-m/s	0-0.8 61-0.43 92-0.1 1524-0.05

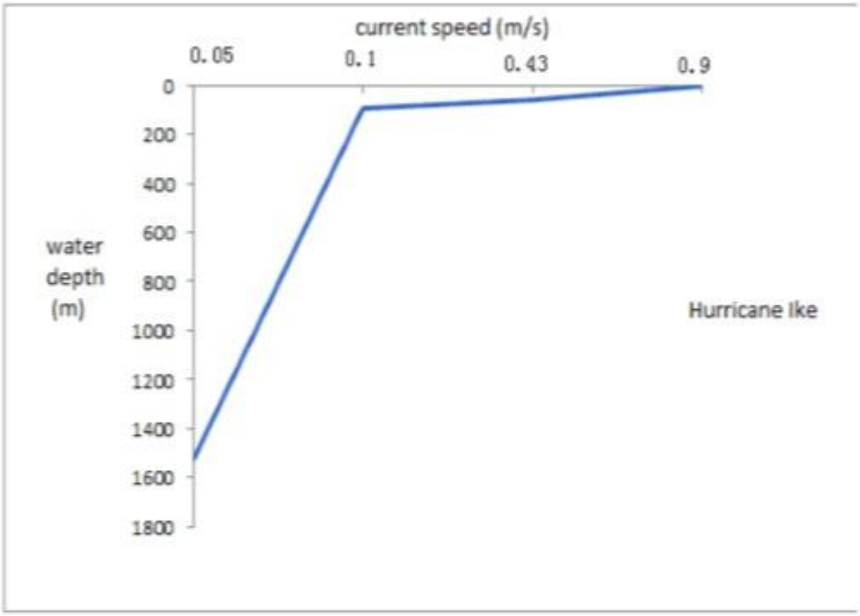

Fig. 5.5 Current profile (Li, 2012)

5.1.5 Field Measurement

Li (2012) pointed out that Environment Platform Response Measurement System (EPRMS) was utilized to record the field measurements. The available records ranged from June 2007 to June 2010 were downloaded from the BMT's Client Data Center (CDC) with the permission of Anadarko Petroleum Corporation. The data used in this study include:

- Mooring Line Tensions
- Hourly Significant Wave Height and Peak Period

- The Platform Position (GPS signals)
- Platform Surge, Sway and Heave
- Roll, Yaw, Heel and Pitch
- Current Profile and direction
- Spar Platform Draft
- Wind Speed and Direction
- Hourly Spar Riser Tension

Particular equipment was attached on the platform to take measurements of currents. The wind was recorded by an anemometer equipped at the platform crane. The mooring tensions were recorded at the chain jack. The field measurements will be presented on the subsection 5.2.1 and 5.2.2 to compare with simulation results by COUPLE.

5.2 Result and Comparison

In this section, time-domain analysis is performed for 'Constitution' Spar during one of the peak hours of hurricane 'Ike'. Three different versions of COUPLE are used in the analysis.

Version 1: TTRs are simplified as vertical constant force acting on the Spar. The results of this case are provided by Zhu (2013). The simulation lasts for 2048 seconds.

Version 2: TTRs with buoyancy cans together with the flex joints at the bottom and two riser guides for each TTR are considered. The simulation duration is also 2048 seconds.

Version 3: Specific models of TTRs tensioned by tensioner systems, riser guides and flex joints at the bottom illustrated in previous sections are integrated into COUPLE in this version. The same duration of simulation is performed.

At first, static analysis was performed to reach an equilibrium position under the combined effects of wind, wave and currents, which contributed to a mean drift force that drove the Spar to a new mean position. At the new mean position, due to the steady forces from waves, wind and current, the TTRs are experiencing the forces at the location of riser guides and tensioner system. In terms of a tensioner system, it could be simply imagined as a spring that was attached between a TTR and the Spar. The imagined “spring” contributes to an increase of total restoring force exerted on the Spar, especially in the heave. The effects of TTRs will be explored in detail in this section. Comparison will be made between three versions and field measurements (FM). All of FM data are cited from Li (2012).

In Version 1, when TTRs are simplified as steady force, the dynamic coupling effects between the TTRs and hull are neglected. In Version 2, the coupling effects at upper deck, riser guides and SCR flex joints are calculated by iterative method. In Version 3, the tensioner systems are considered. Comparison between Version 1 and 2 will be useful in investigating effects of riser guides and comparison between Version 2 and 3 may reveal the coupled effects from tensioner systems

5.2.1 Translation Motions Comparison

Fig. 5.6 compares the translation motions of the three versions. To ensure clearness, simulation that lasts 1000 seconds is presented and the ramp function is effective in the first 100 seconds.

5.2.1.1 Effects of Riser Guides

The comparison between Version 1 and Version 2 may reveal the effects of riser guides. It can be found that the motion trends in surge and sway directions are quite synchronized but between the curves of Version 1 and Version 2 there is certain discrepancy, which is attributed to the coupling effects at riser guides (See Fig. 5.6). Also, the difference of mean drift steady position gives rise to the amplitude difference of later motion.

In surge direction, comparing the results of Version 1 with those of Version 2, the maximum displacement increases about 2.47m and minimum displacement increases about 2.90m (See Table 5.7). Although the RMS value increases from 2.87m to 2.95m, it should be noted that the difference between maximum displacement and minimum displacement changes from 20.10m to 19.67m. In terms of the sway mode, RMS value decreases from 3.34m to 3.27m by about 2.1%, yet difference between maximum displacement and minimum displacement changes from 12.44m in Version 1 to 12.24m in Version 2. A shift of about 0.239m takes place at mean sway position, mainly due to the different initial positions of 2 versions. Despite of certain discrepancy of time series curves, from statistical results it can be concluded that the horizontal motions are not affected obviously by riser guides.

In heave direction, if TTRs with buoyancy cans are modeled, the heave RMS changes from 0.59m to 0.52m and the difference is not that big. Since buoyancy can TTRs are decoupled from the hull in vertical direction, this reduction may be due to coupling effect between heave and other motion modes. Overall, TTR with buoyancy cans have limited effects on heave motion.

5.2.1.2 Effects of Tensioner System

The comparison between the results of Version 2 and Version 3 reflects effects of tensioner systems. The curves of the two versions nearly overlap with each other in surge and sway modes (See Fig. 5.6). It means though riser guides play a crucial role in providing extra lateral force for the hull, tensioner system does not affect the horizontal motions substantially. This could be verified statistically that difference of maximum, minimum, mean and RMS values between Version 2 and Version 3 are mostly within 3% (See Table 5.7).

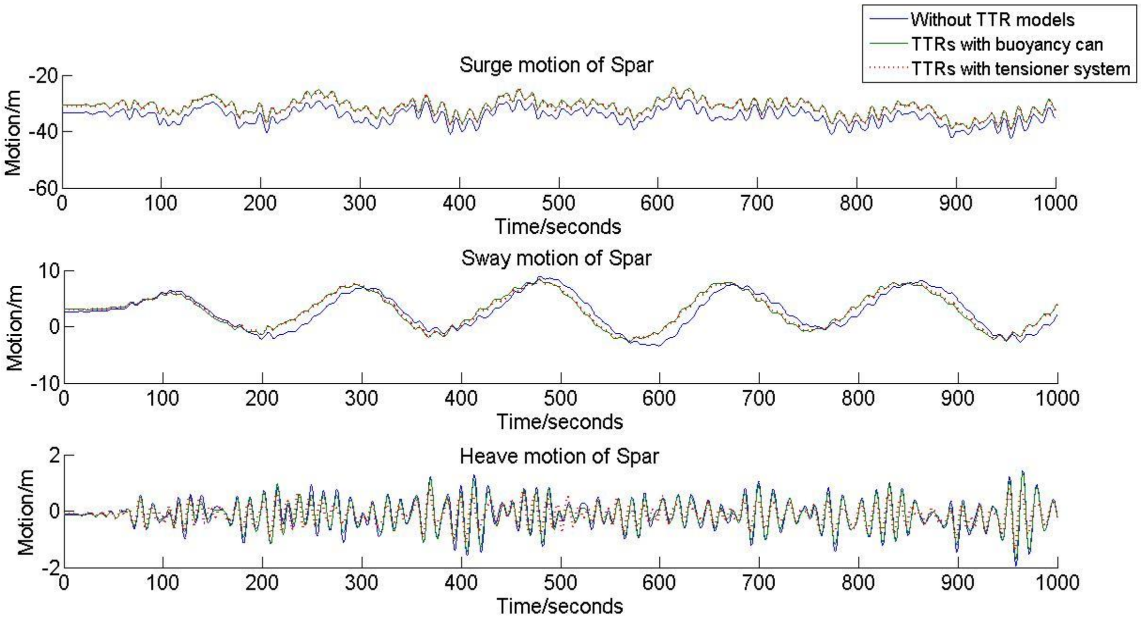

Fig. 5.6 Comparison in surge, sway and heave motions

However, the heave oscillation reduces significantly when tensioner systems are supplied. The heave statistics show that the mean position change is tiny, while the RMS value decreases from Version 1/ 2 to Version 3 (See Table 5.7). When tensioner systems replace buoyancy cans, large vertical restoring forces apply on the hull and thus heave RMS is strongly reduced. It is obvious that tensioner systems increase the vertical restoring stiffness of the floating system. The comparison between Version 2 and Version 3 indicates that maximum value decreases by about 38.1% and minimum value increase by about 27.0%. The RMS reduction rate reaches as high as 27.6% compared to Version 2 (See Table 5.7).

Table 5.7 Statistical analysis on translation motions and comparison with field measurements

Direction	Statistics	Without TTR models (Version 1)	TTRs with Buoyancy Can(Version 2)	TTRs with Tensioner System (Version 3)	Field Measurement
Surge	Mean(m)	-34.379	-31.056	-31.465	-40.000
	Max(m)	-26.724	-24.252	-24.584	-27.200
	Min(m)	-46.826	-43.922	-44.085	-54.300
	SD(m)	2.871	2.949	2.863	3.000
Sway	Mean(m)	2.854	3.093	3.117	3.000
	Max(m)	9.043	9.574	9.298	9.500
	Min(m)	-3.395	-2.669	-2.605	-4.000
	SD(m)	3.339	3.273	3.199	2.800
Heave	Mean(m)	-0.104	-0.114	-0.122	-0.100
	Max(m)	1.462	1.366	0.846	1.000
	Min(m)	-2.321	-2.097	-1.531	-1.100
	SD(m)	0.596	0.525	0.380	0.300

5.2.1.3 Comparison with the Field Measurements (FM)

Comparison with the FM may verify the reliability and robustness of the numerical codes. During the measurements, errors might exist while measuring significant wave height. This may lead to inaccuracy in numerical simulation. It is noted that before the hurricane ‘Ike’, the origin of the Spar was not locating at (0,0). The discrepancy of two origins gives rise to errors in maximum, minimum and mean values of FM data. What is more, after wave components were separated, random phases were selected to generate the wave fields, which were different from real conditions and led to mismatching between simulation results and FM data. Therefore the difference of mean, maximum and minimum values are partially due to the uncertainty of measurements, the difference of origins and randomness of wave phases. It is of more significance to focus on RMS value, which reflects statistical characteristics of Spar motion.

The RMS amplitude of surge is 2.95m or 2.86m when 6 TTRs are modeled (See Table 5.7). The difference with FM surge amplitude is within 5%. In sway motion, both simulation results from Version 2 and Version 3 are about 10% bigger than FM result but still agree reasonably well with FM. In the case of buoyancy can, heave RMS is about 50% larger than measurements. If tensioner system is modeled, heave RMS is 0.38m, which is very close to the measurements.

5.2.2 Rotation Motions Comparison

5.2.2.1 Effects of Riser Guides

The comparison between Version 1 and Version 2 indicates that the RMS value of roll decreases from 0.470 degree to 0.266 degree by about 43.4% when coupling effects at riser guides are considered. The pitch RMS angle of Version 2 is 1.552 degree, 13.4% smaller than that of Version 1. The yaw RMS value of Version 2 also reduces to 0.719 degree with a 13.79% reduction compared to Version 1. This phenomenon corresponds to the utilization of TTRs with buoyancy cans. It means that the coupled effects reduce the motion in roll/pitch/yaw modes. The system rotational stiffness is enhanced as a result of the existence of riser guides and TTRs. The changes of natural frequency will be discussed in subsection 5.2.3.

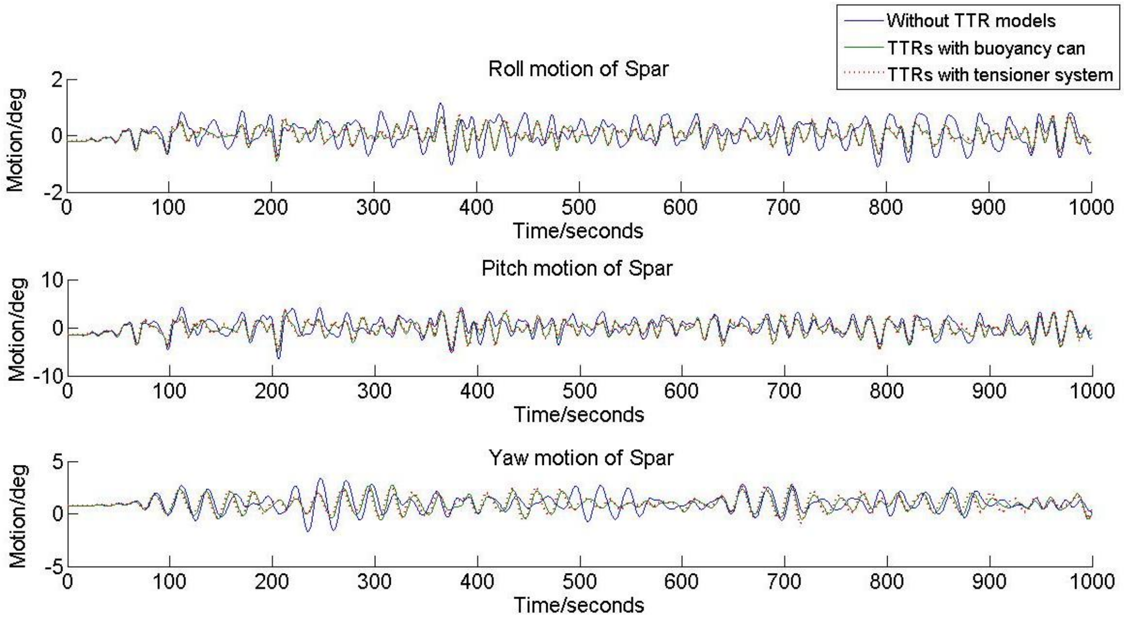

Fig. 5.7 Comparison in roll, pitch and yaw motions

5.2.2.2 Effects of Tensioner System

Turning to the comparison between Version 2 and Version 3, curves of time series mostly overlap with each other (See Fig. 5.7). Statistical results as well demonstrate that Version 3, in which TTRs with tensioner systems are adopted, show negligible discrepancy with Version 2 (See Table 5.8). According to simulation results, RMS values of roll/pitch/yaw increase within only 4%. Thus it can be concluded the rotation motion will not be affected substantially by tensioner systems.

5.2.2.3 Comparison with Field Measurements

While comparing to FM, as reasons explained in the previous subsection, discrepancy occurs while comparing the maximum, minimum and mean values. The simulated RMS results agree reasonably well with FM data especially in pitch mode, which is the dominant rotation in the case of hurricane “Ike”. The pitch RMS is only 0.052 degree larger than that of FM in case of TTRs with buoyancy can. In terms of roll and yaw rotation, the simulation results are about 30% smaller than measurements; however it should be noted that the magnitudes of roll and yaw are much smaller than that of pitch hence the magnitude of numerical error is unimportant.

Table 5.8 Statistical analysis on rotation motions and comparison with field measuements

Direction	Statistics	Without TTR models (Version 1)	TTRs with Buoyancy Can(Version 2)	TTRs with Tensioner System (Version 3)	Field Measurement
Roll	Mean(deg)	0.118	0.055	0.053	-0.100
	Max(deg)	1.316	0.766	0.843	1.200
	Min(deg)	-1.350	-0.944	-1.036	-2.100
	SD(deg)	0.470	0.266	0.271	0.400
Pitch	Mean(deg)	0.292	-0.049	-0.014	-2.000
	Max(deg)	5.798	4.823	5.128	0.400
	Min(deg)	-6.452	-6.044	-6.328	-7.000
	SD(deg)	1.794	1.552	1.581	1.500
Yaw	Mean(deg)	1.018	0.983	0.993	0.100
	Max(deg)	3.417	3.153	3.246	3.200
	Min(deg)	-1.685	-1.209	-1.279	-3.000
	SD(deg)	0.834	0.719	0.747	0.900

5.2.3 Power Spectrum Comparison

From graph (a) of Fig. 5.8, the spectrums of three versions in surge direction almost overlap with each other, in both low frequency (ω=0~0.02 Hz) and the wave frequency range (ω=0.05~0.08 Hz). The slow drift motion in low frequency is dominant in surge direction. The natural frequency of the floating system does not indicate any shifts after riser guides and tensioner systems are considered. The identical conclusions can be drawn in sway direction. The motion at wave frequencies is negligible, whilst the motion at the frequency of about 0.005Hz is quite dominant. The peak corresponds to the response of the floating system in sway natural frequency (See graph (b) of Fig. 5.8). However, this natural frequency seems not affected by riser guides and tensioner system. From both surge and sway spectrum, it can be concluded that the riser guides and tensioner system do not affect the horizontal stiffness obviously, which is the determinant factor of natural frequency.

Turning to the heave spectrum, it is revealed that the spectrum of Version 1 and Version 2 are quite similar, and that most of the heave motion energy concentrates on the wave frequency range. This implies buoyancy can TTRs do not exert much impact on the heave spectrum since they are decoupled from the Spar in vertical direction. However, after supplying tensioner systems, the heave motion is reduced, and this corresponds well to the conclusion drawn in 5.2.1.2. Though heave RMS substantially decreases, the locations of peaks do not show any shifts (See graph (c) of Fig. 5.8).

When it comes to rotation motions, the motion at wave frequency (ω=0.05~0.08 Hz) can be observed in roll and pitch modes but is negligible in yaw mode (See graph (d), (e) and (f) of Fig. 5.8). Besides, natural frequencies of roll, pitch and yaw increase as a result of riser guides and tensioner systems. The original natural frequencies of roll and pitch before including TTRs are both about 0.038 Hz, and it can be shown from several peaks appearing within this range (See graph (d) and (e) of Fig. 5.8). Yet, after riser guides and tensioner system are considered, the related peaks move to approximately 0.04 Hz. The riser guides and TTRs contribute to an enhancement of the rotational stiffness in roll and pitch, which in turn increases the rotational natural frequency in these two modes. In yaw spectrum, there are other peaks besides peaks induced by roll and pitch around 0.04 Hz. For instance, the peak at about 0.045 Hz of the spectrum of Version 1 may be related to the yaw natural frequency. The related peak also moves to higher frequency range in the spectra of Version 2 and Version 3. The phenomenon indicates that the riser guides, the tensioner systems and TTRs may also contribute to an increase of yaw natural frequency.

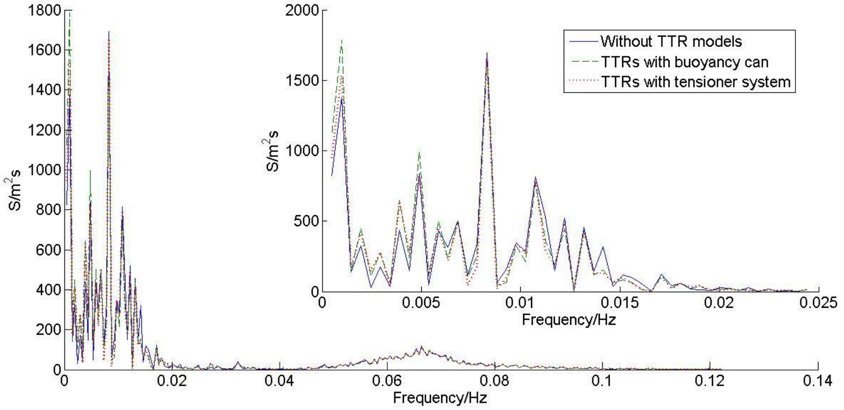

(a) Surge

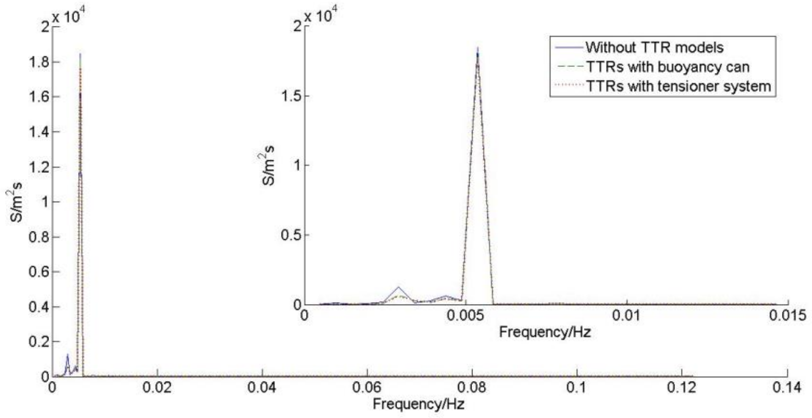

(b) Sway

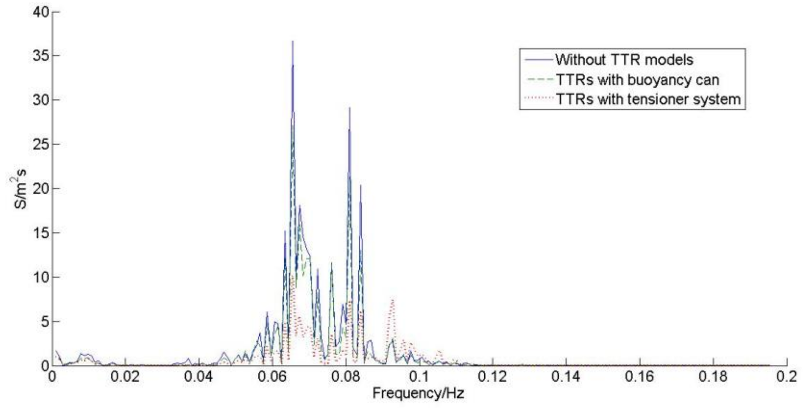

(c) Heave

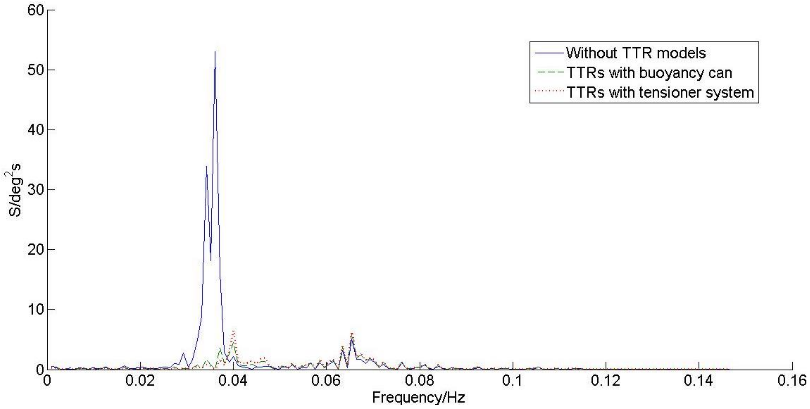

(d) Roll

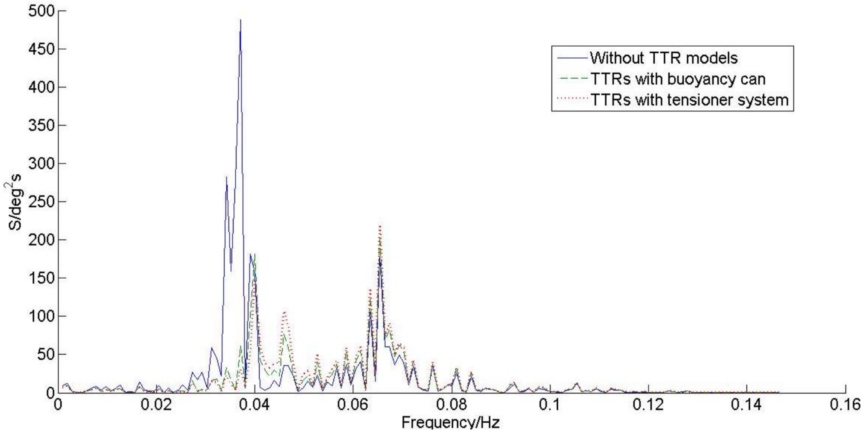

(e) Pitch

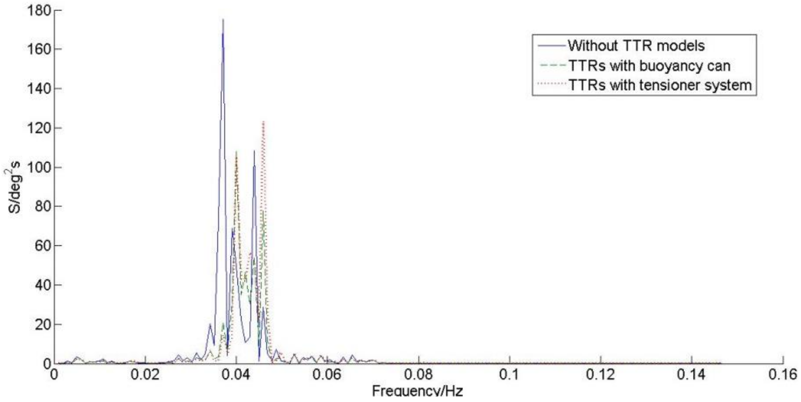

(f) Yaw

Fig. 5.8 Comparison of 6DOFs spectrum during the peak hours of ‘Ike’

5.2.4 Mooring Line/Risers Tension Comparison

5.2.4.1 Comparison among Three Versions

The statistics of the tension in each mooring line/SCR are derived, and the results are presented in Table 5.9. Overall, the RMS values of tension in each mooring line/SCR are smaller in Version 2 and Version 3 than in Version 1. It is consistent with the trends of the RMS results of the Spar translation of the three versions. Although surge and sway motions do not substantially differ with each other, there is a significant decrease in heave motion RMS in Version 2 and Version 3. Among Version 2 and Version 3, RMS tension values in Version 3 are further reduced and it is mainly due to the even smaller heave RMS in case of TTR tensioned by tensioner system. When the overall heave motion is smaller, the tension RMS at fairlead or porch is also smaller.

In terms of mean values of tension, after TTRs are considered in the simulation of Version 2 and Version 3, the mean tension of mooring line 1, 2 and 3 is reduced whilst mean tension of mooring line 4 to 9 increases. This is due to the fact that the first 3 mooring lines are in the upwind direction and other 6 lines are in the downwind. After considering TTR coupling effects, the equilibrium position will be adjusted; the existence of riser guides increases the horizontal restoring force and this leads to the change of mooring line tension in both sides of Spar.

5.2.4.2 Comparison with Field Measurement

While comparing with FM data, as discussed in the previous subsections, RMS values are the most significant. Yet it is found in all mooring lines, the numerical results in three cases are much greater than FM data, though results of Version 2 and Version 3 are closer to those of measurements. According to reasons stated in Li (2012), the large discrepancy is mainly due to the friction at the fairlead that significantly reduced the dynamic tension after the fairlead roller. The measured tension at the chain jack is related to the tension after the fairlead roller while the simulated tension is equal to the tension force before the fairlead. Similar differences were also observed in the previous study of Hurricane Ike done by Kiecke (2011).

Though considerable discrepancy between simulation and FM emerge in dynamic tension, the measured mean tension recorded at the chain-jack agreed reasonably well with the simulated mean tension in an overall view (see Table 5.9). The error between simulated results and measurements is within 10% in most mooring lines.

Table 5.9 Hurricane ‘Ike’ mooring line/riser tension comparison

Mooring Line #	Tension (kN)	Without TTR models (Version 1)	TTRs with Buoyancy Can(Version 2)	TTRs with Tensioner System (Version 3)	Field Measurement
Line 1	Max	8906.89	8672.96	8718.68	6774.64
	Min	2872.01	2579.86	2440.07	3309.47
	Mean	4766.72	4400.14	4445.23	4793.40
	RMS	823.95	784.73	772.74	474.00
Line 2	Max	8399.00	8422.10	8457.95	5960.61
	Min	2742.83	2486.81	2345.77	2815.72
	Mean	4475.39	4226.72	4265.88	4164.24
	RMS	790.18	765.41	752.73	431.00
Line3	Max	8487.35	8414.69	8445.92	6476.61
	Min	2843.22	2555.50	2416.32	3087.06
	Mean	4559.02	4248.20	4287.26	4548.75
	RMS	797.94	760.49	746.65	465.00
Line 4	Max	2616.34	2629.17	2564.41	2588.86
	Min	1957.35	1956.32	2023.04	2259.69
	Mean	2255.18	2271.87	2269.38	2432.30
	RMS	99.92	92.64	82.28	39.00
Line 5	Max	2614.50	2611.24	2610.48	2557.72
	Min	1876.33	1862.02	1919.54	2188.52
	Mean	2220.40	2238.12	2235.59	2367.52
	RMS	108.19	103.62	96.07	40.00
Line 6	Max	2694.17	2703.64	2731.58	2851.31
	Min	1786.89	1760.49	1807.64	2357.55
	Mean	2208.00	2227.37	2224.77	2593.71
	RMS	128.18	127.52	122.48	58.00
Line 7	Max	3417.13	3335.18	3281.02	3006.99
	Min	1605.75	1548.68	1585.97	2055.07
	Mean	2448.26	2444.59	2442.63	2538.91
	RMS	266.19	257.32	254.13	106.00
Line 8	Max	3227.35	3201.02	3138.54	2900.24
	Min	1666.09	1621.81	1665.85	2041.73
	Mean	2405.79	2424.32	2422.60	2479.17
	RMS	219.74	218.03	213.01	94.00
Line 9	Max	3278.10	3249.79	3176.26	2873.55
	Min	1729.06	1696.03	1749.90	2019.49
	Mean	2464.31	2486.35	2484.70	2473.03
	RMS	213.02	209.46	201.85	95.00

Table 5.9 Continued

Mooring Line #	Tension (kN)	Without TTR models (Version 1)	TTRs with Buoyancy Can(Version 2)	TTRs with Tensioner System (Version 3)	Field Measurement
SCR 1	Max	667.49	657.77	649.12	NA
	Min	522.19	526.48	539.79	NA
	Mean	592.05	591.34	591.44	NA
	RMS	25.50	22.49	18.04	NA
SCR 2	Max	1068.80	1055.53	1040.40	NA
	Min	862.08	868.71	888.94	NA
	Mean	963.38	962.12	962.29	NA
	RMS	35.92	31.86	25.79	NA

5.2.5 Effects of Flex Joints

5.2.5.1 Effects of Flex Joints on Spar

Table 5.10 Effects of flex joint on Spar motion

Direction	Statistics	Hinge	With Flex Joint
Surge	Mean(m)	-33.0616	-33.0591
	Max(m)	-24.8029	-24.7984
	Min(m)	-44.9784	-44.9792
	RMS(m)	2.7507	2.7509
Sway	Mean(m)	3.2386	3.2390
	Max(m)	7.3775	7.3812
	Min(m)	-1.0525	-1.0457
	RMS(m)	2.0153	2.0153
Heave	Mean(m)	-0.6158	-0.6157
	Max(m)	0.5561	0.5552
	Min(m)	-2.0861	-2.0854
	RMS(m)	0.3706	0.3706
Roll	Mean(deg)	0.0617	0.0616
	Max(deg)	0.9444	0.9433
	Min(deg)	-1.1727	-1.1698
	RMS(deg)	0.2982	0.2976
Pitch	Mean(deg)	0.0243	0.0239
	Max(deg)	5.0410	5.0289
	Min(deg)	-5.5504	-5.5426
	RMS(deg)	1.7543	1.7520
Yaw	Mean(deg)	1.0197	1.0203
	Max(deg)	3.2083	3.2111
	Min(deg)	-1.2660	-1.3005
	RMS(deg)	0.6583	0.6599

To analyze the effects of flex joints, another case is run in COUPLE by excluding effects of flex joints in Version 3. The connection point between a SCR and the Spar is assumed to be a hinge. Table 5.11 compares statistical results of Spar motion when a hinge is used at the porch and when a flex joint is used there. It can be seen that translation motions in both two cases virtually show no differences. For instance, in surge direction, RMS value increases by only 0.0002m.

Rotation motion shows relative bigger difference, though still very tiny, due to the moments applied by flex joints. The roll RMS amplitude decreases by about 0.2%, the pitch amplitude decrease by about 0.13% and the yaw RMS amplitude increases by about 0.24%. The mean, maximum and minimum values show negligible discrepancy, thus it can be concluded that the effects of flex joints are negligible for the global motion of Spar.

5.2.5.2 SCR Bending Moment Distribution Analysis

The flex joint can exert a bending moment at the upper end of SCR and how it affects the bending moment distribution along SCR is discussed in this subsection.

Fig. 5.9 reveals the comparison of bending moment between a hinge at the porch and a flex joint used at the porch. The porch is 140 meters below the sea surface. When a flex joint is used, there is a considerable increase of bending moment near the porch. However, the further away from the porch the node is, the smaller the bending moment magnitude at that node will be. Though amplitudes of bending moments are different at different nodes, their phases are quite synchronized.

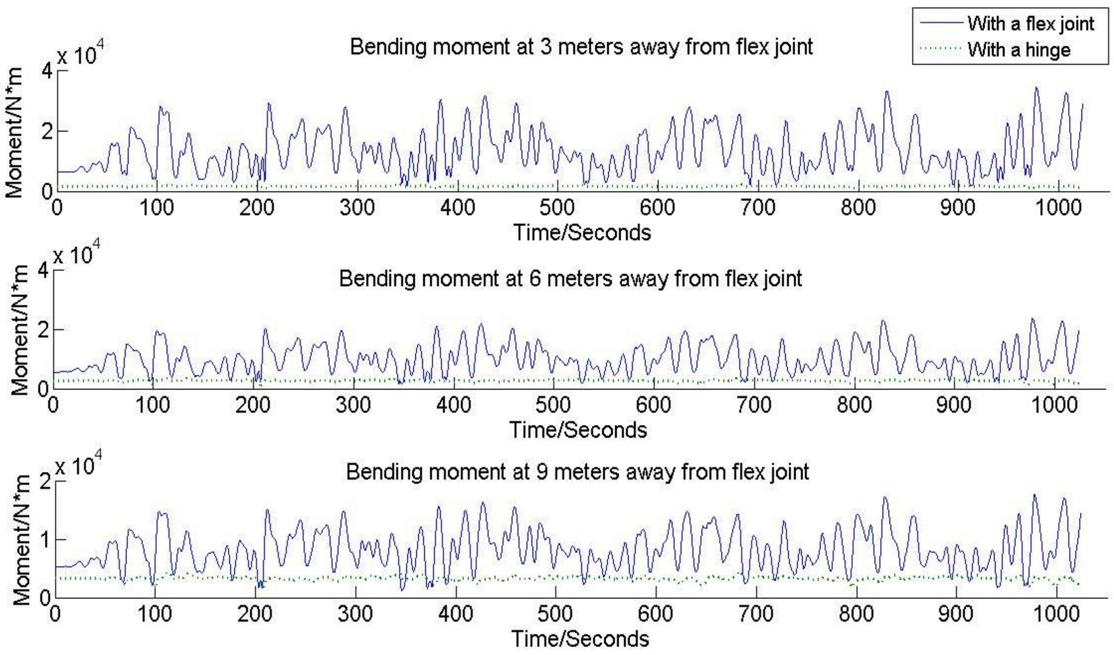

Fig. 5.9 Comparison of bending moments at the vicinity of porch

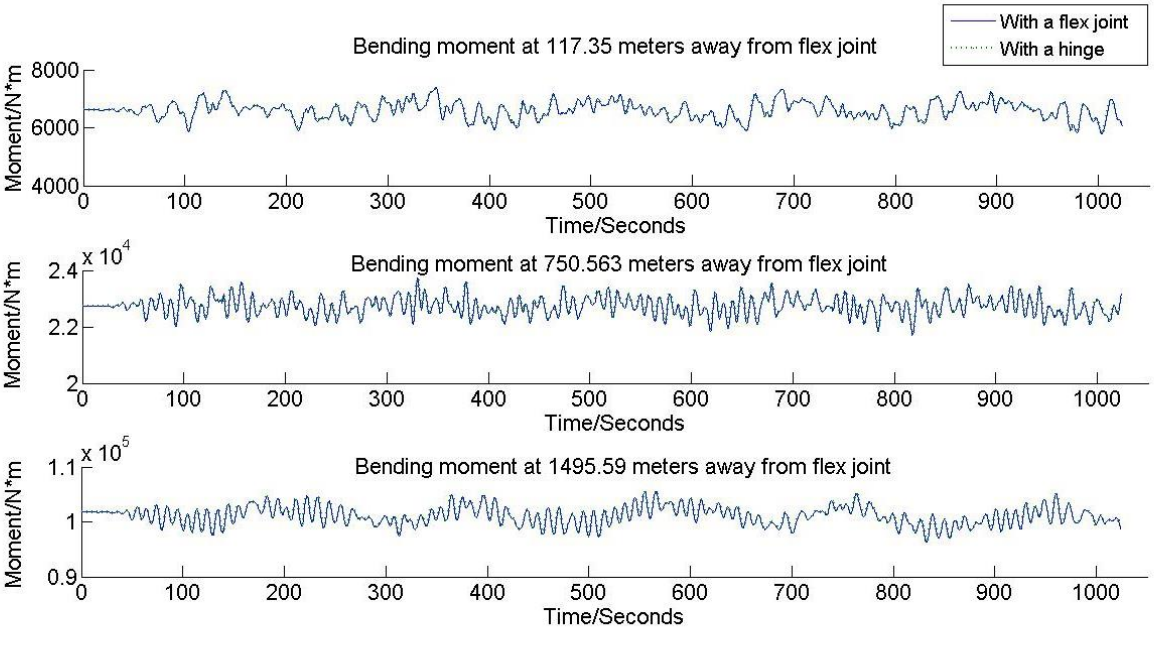

Fig. 5.10 Comparison of bending moments far away from the flex joint

At the node 117m away from the porch, the discrepancy between two cases is negligible. When the distance is 750.563m or 1495.59m, the curves of two times series nearly overlap with each other (See Fig. 5.10). However, the amplitude of bending moment becomes larger as the interested point goes further away from the porch. It is very likely that these points are near the touch-down point thus the bending moment at this place is considerable.

Table 5.11 Mean & dynamic bending moment comparison at various nodes

	Mean Bending Moment ($N \cdot m$)		Dynamic Bending Moment($N \cdot m$)	
Distance to flex joint	With Flex Joint	With a Hinge	With Flex Joint	With a Hinge
3.00	13761.53	1539.07	7082.12	190.71
6.00	10214.04	2594.88	4691.37	317.91
9.00	8378.35	3234.61	3350.05	391.65
117.35	5586.60	5544.06	386.14	377.25
222.70	6605.06	6598.66	311.15	305.22
328.05	7949.98	7948.95	277.26	272.01
433.40	9743.58	9743.21	258.85	255.31
538.75	11848.86	11848.44	268.89	265.68
750.54	18083.58	18083.12	304.00	301.60
856.97	22730.99	22730.62	334.82	333.58
963.41	29270.72	29270.42	365.53	363.81
1069.84	38725.07	38724.91	519.02	516.15
1176.28	52683.65	52684.02	649.18	650.51
1282.72	73175.16	73177.07	1010.38	1009.06
1389.15	101065.17	101069.39	1732.05	1732.72
1495.59	131189.53	131195.19	2363.42	2363.42
1602.02	89191.87	89188.79	1354.29	1354.81

Statistical results give a quantitative view of bending moments along SCR (See Table 5.11). For both mean and dynamic bending moment, the difference between 2 cases diminishes as the distance from the porch increases. At the nearest node, which is 3m away from flex joint, the mean bending moment is 8.9 times the bending moment when a hinge is adopted and the dynamic bending moment is nearly 37 times that of hinged condition. However, at the node 117.35m away from the porch, the mean and RMS bending moment only increases by about 0.78% and 2.9%, respectively. Thus it can be concluded that when the distance is larger than 100 meters, bending moments of two cases are almost similar, thus effects of flex joints can be negligible.

Dynamic bending moment is crucial to the fatigue life of SCRs; therefore the flex joint with large rotational stiffness will contribute to an increase of the amplitude of cyclic stress in the vicinity of flex joint. The number of cycles to failure is reduced in accordance with S-N curve. Soft flex joints are recommended in engineering applications to reduce cyclic loading, or thick pipes or stress joints are to be used near the porch, thus prolonging the fatigue life of the materials near flex joint.

6. CONCLUSIONS

In this study, the existing code CABLE3D is extended to include the models of top tension system of TTRs, riser guide and flex joint. Individual tensioner cylinder in a tensioner system is modeled as a linear spring that applies concentrated force on TTR. Linear rotational spring is adopted to represent a flex joint. The up-dated CABLE3D is proved to be robust, convergent and stable in performing static and dynamic analysis of selected cases for a TTR and a SCR. After verification of CABLE3D, all these modules are integrated into COUPLE, making COUPLE capable of analyzing a floating system with TTRs and SCRs with flex joints. The 'Constitution' Spar is used as an example. Using the up-dated COUPLE, it is simulated under hurricane 'Ike' met-ocean conditions and further analysis on effects of the tensioner system, riser guides and flex joints are conducted. The main conclusions based on this study are summarized below.

1. While riser guides are considered, the maximum curvature takes place in the vicinity of the lowest guide (keel guide), meaning the maximum bending moment occurs at this place. Thus the amplitude of cyclic stress increases as a result, and due to S-N curve the number of cycles to failure and the corresponding fatigue life decreases.

2. While analyzing ‘Constitution’ Spar, TTRs with buoyancy cans and TTRs with tensioner systems are integrated into the floating system, respectively, and flex joints are modeled at the porch of SCR. The riser guides do not affect the surge and sway motion substantially. The heave motion RMS amplitude decreases significantly in the case of tensioner systems installed on TTRs.
3. For roll, pitch and yaw modes, their RMS are significantly reduced compared to those without consideration of TTRs. The reduction is mainly due to the extra horizontal loads at riser guides. The system rotational stiffness and rotation natural frequencies are enhanced as a result of the existence of riser guides. On the other hand, tensioner systems have very limited impact on rotation motions.
4. Flex joint does not affect the global performance of the Spar, as expected. The moments exerted by flex joints are tiny compared to total moments applied on the hull by wave, current and winds.
5. The utilization of flex joints will contribute to an increase in bending moment on the vicinity of SCR porch. The further a node is away from the porch, the smaller the effects of a flex joint will be. To reduce cyclic loading near porch, a flex joint with relative small rotational stiffness is recommended.

In summary, with the newly up-dated modules, the applications of CABLE3D have been significantly widened. The integration of up-dated CABLE3D into COUPLE has allowed the analysis of floating production system with TTRs tensioned by either buoyancy cans or tensioner systems and SCRs connecting flex joints at the porches. The simulation results have been compared to field measurements and show better consistency with the measurements. More accurate analysis can be performed if detailed configuration of TTRs and mooring system is obtained. The nonlinear approach of modeling tensioner cylinders and flex joints and how it differs with linear approach may require further research efforts.

REFERENCES

API Recommended Practice 2RD, 2006. Design of Risers for Floating Production Systems (FPSs) and Tension-Leg Platforms (TLPs). American Petroleum Institute, Washington, DC.

Cao, P.M., Zhang, J., 1997. Slow motion responses of compliant offshore structures. International Journal of Offshore and Polar Engineering 7(2), 119-126.

Chen, C.Y., Kang, C,H., Mills, T., 2008, Coupled Spar Response with Buoyancy Cans vs. Tensioners. Proceedings of the Eighteenth (2008) International Offshore and Polar Engineering Conference, Vancouver.

Chen, C.Y., Nurtjahyo, P., 2004, Numerical Prediction of Spar Motions Considering Top Tension Riser Stiffness. Proceedings of OMAE04, 23rd International Conference on Offshore Mechanics and Arctic Engineering, Vancouver.

Chen, X.H., 2002, Studies on dynamic interaction between deep-water floating structure and their mooring/tendon systems. PhD thesis, Texas A&M University, College Station.

Deka, D., Campbell, M., and Kaka, K., 2H Offshore Inc; Hays, P.R., Chevron ETC, 2010. Gulf of Mexico Wet Tree Deepwater Riser Concepts with Sure Service. OTC 20437-PP.

FloaTEC, RPSEA CTR 1402, Ultra Deepwater Dry Tree System for Drilling and Production in GOM, Stage 1 Study Report, June 19 2009, FloaTEC project# 08110.

Garrett, D.L., 1982. Dynamic analysis of slender rods. Journal of Energy Resources Technology, Transaction of ASME 104, 302-307.

Kiecke, A.F., 2011. Simulated fatigue damage index on mooring lines of a Gulf of Mexico truss Spar determined from recorded field data. MS Thesis, Ocean Engineering Program, Civil Engineering Department, Texas A&M University, College Station.

Kim, M.H., Chen, W., 1994. Slender-body approximation for slowly-varying wave loads in multi-direction waves. Proceeding of the 6th Offshore and Polar Engineering Conference, I, 262-272.

Li, C.X., 2012. Coupled Analysis of The Motion and Mooring Loads of a Spar ‘Constitution’. MS Thesis, Ocean Engineering Program, Civil Engineering Department, Texas A&M University, College Station.

Ma, W., Webster, W.C., 1994. An Analytical Approach to cable Dynamics: Theory and User Manual. Sea Grant Project R/OE-26.

Magee A., Sablock A., Maher J., Halkyard J., Finn L., Dutta Indra., 2000. Heave Plate Effectiveness in the performance of the Truss Spar. Proceeding of the

ETCE/OMAE2000 Joint Conference on Energy for the New Millennium, New Orleans. pp. 367-371.

Morison, J.R., O'Brien, M.P., Johonson, J.W. and Shaaf, S.A., 1950. The forces exerted by surface waves on plies. Petrol. Trans. AIME 189, 149-154.

Murray, J., Tahar, A., and Yang, C.K., 2007, Hydrodynamics of Dry Tree Semisubmersible. Proceedings of the ISOPE'07, Lisbon.

Murray, J., Tahar, A., and Eilertsen, T., 2006, A Comparative Assessment of Spar, Tension Leg Platform and Semisubmersible Floaters for Deepwater Application. Proceedings of the DOT International Conference and Exhibition.

Perryman, S., Gebara, J., Botros, F., Yu, A., 2005. Holstein Truss Spar and Top Tensioned Riser System Design Challenges and Innovations. OTC 17292.

Prislin, I., R. Rainford, S. Perryman and R. Schilling, 2005. Use of Field Monitored Data for Improvement of Existing and Future Offshore Facilities. SNAME Paper D5.

Webster, R.L., 1975. Non-linear static and dynamic response of underwater cable structures using finite element approach. In: Proceeding of the 7th Offshore Technology Conference, Houston, OTC 2322, pp753-764.

Webster, W.C., 1995. Mooring-induced damping. Ocean Engineering, Volume 22, Issue 6, pp 571-591.

Yang, C.K, Kim, M.H, 2010. Linear and Nonlinear Approach of Hydropneumatic Tensioner Modeling for Spar Global Performance, Journal of Offshore Mechanics and Arctic Engineering, Vol.132, pp 1-9.

Zhu, L.Y, 2013. Report for the project ‘CFD Based Multiple Moored Floater/Riser Analysis System Applicable to Highly Non- linear and Large Amplitude Motion Simulations’. Unpublished Report from Ocean Engineering Program, Civil Engineering Department, Texas A&M University, College Station.

APPENDIX A

NUMERICAL MODEL OF FLEX JOINT

The bending moment at aflex joint is denoted by $\tilde{\mathbf{M}}(\vec{\boldsymbol{r}}'(t)+\boldsymbol{\delta}\vec{\boldsymbol{r}}'(t))$. It is induced by the angle θ between $\vec{\boldsymbol{r}}'(t)+\boldsymbol{\delta}\vec{\boldsymbol{r}}'(t)$ and $\vec{\boldsymbol{r}}'_0$, where $\vec{\boldsymbol{r}}'(t)+\boldsymbol{\delta}\vec{\boldsymbol{r}}'(t)$ represents the direction vector at the upper end of riser at time step *(t)* and $\vec{\boldsymbol{r}}'_0$ the direction vector when no moment is applied at the flex joint (equilibrium position for most cases). θ can be calculated if $\vec{\boldsymbol{r}}'(t)+\boldsymbol{\delta}\vec{\boldsymbol{r}}'(t)$ and $\vec{\boldsymbol{r}}'_0$ are known. The direction of $\tilde{\mathbf{M}}$ can also be determined by $(\vec{r}\,'(t)+\delta\vec{r}\,'(t))\times\vec{r}\,'_0$.

At first, the magnitude of the moment is calculated by,

$$\tilde{\mathbf{M}} = M_0\boldsymbol{\theta} \tag{A.1}$$

where M_0 represents the linear rotational stiffness of the flex joint, which should be provided by the user based on the types of the flex joint used in the design. The magnitude of $\boldsymbol{\theta}$ is given by

$$\theta = \arcsin\left[1-\left(\frac{(\vec{\boldsymbol{r}}'+\delta\vec{\boldsymbol{r}}')\cdot\vec{\boldsymbol{r}}'_0}{|\vec{\boldsymbol{r}}'+\delta\vec{\boldsymbol{r}}'||\vec{\boldsymbol{r}}'_0|}\right)^2\right]^{\frac{1}{2}} \tag{A.2}$$

Assuming that the elongation of the riser can be ignored, both $|\vec{\boldsymbol{r}}'+\delta\vec{\boldsymbol{r}}'|$ and $|\vec{\boldsymbol{r}}'_0|$ are equal to 1. The Taylor expansion of $\arcsin\left[1-\left(\frac{(\vec{\boldsymbol{r}}'+\delta\vec{\boldsymbol{r}}')\cdot\vec{\boldsymbol{r}}'_0}{|\vec{\boldsymbol{r}}'+\delta\vec{\boldsymbol{r}}'||\vec{\boldsymbol{r}}'_0|}\right)^2\right]^{\frac{1}{2}}$ is given by:

$$\theta = \sum_{n=0}^{+\infty} \frac{(2n)!}{4^n (n!)^2 (2n+1)} x^{2n+1} \text{ and } x = \left[1 - \left(\frac{(\vec{\mathbf{r}}' + \delta\vec{\mathbf{r}}') \cdot \vec{\mathbf{r}}'_0}{|\vec{\mathbf{r}}' + \delta\vec{\mathbf{r}}'| |\vec{\mathbf{r}}'_0|} \right)^2 \right]^{\frac{1}{2}} \tag{A.3}$$

The calculation of θ is divided into two parts, the first depends on $\vec{\mathbf{r}}'(t)$ only, which is up-dated at each time step; the second depends on $\delta\vec{\mathbf{r}}'(t)$, which is unknown and solved in the global matrix equation **A**δ**X**=**B.**

$$\theta = \theta_0 - R_1 \delta r_1' - R_2 \delta r_2' - R_3 \delta r_3' \tag{A.4}$$

where $\theta_0 = \arccos(\vec{r}' \cdot \vec{r}'_0)$,

$$R_1 = \left[\sum_{n=0}^{+\infty} \frac{(2n)!}{4^n (n!)^2 (2n+1)} C_{2n+1}^1 \left(\sqrt{1 - (\vec{r}' \cdot \vec{r}_0')^2}\right)^{2n-1} \vec{r}' \cdot \vec{r}_0' \right] r'_{01}$$

$$R_2 = \left[\sum_{n=0}^{+\infty} \frac{(2n)!}{4^n (n!)^2 (2n+1)} C_{2n+1}^1 \left(\sqrt{1 - (\vec{r}' \cdot \vec{r}_0')^2}\right)^{2n-1} \vec{r}' \cdot \vec{r}_0' \right] r'_{02}$$

$$R_3 = \left[\sum_{n=0}^{+\infty} \frac{(2n)!}{4^n (n!)^2 (2n+1)} C_{2n+1}^1 \left(\sqrt{1 - (\vec{r}' \cdot \vec{r}_0')^2}\right)^{2n-1} \vec{r}' \cdot \vec{r}_0' \right] r'_{03} \tag{A.5}$$

From Chen (2002),

$$\tilde{\mathbf{M}} = \vec{\mathbf{r}}' \times (B\vec{\mathbf{r}}'') + H\vec{\mathbf{r}}' \tag{A.6}$$

where H is the torque and B is the bending stiffness. $H=0$ is assumed in this case. According to headings of $\vec{\mathbf{r}}'(t) + \delta\vec{\mathbf{r}}'(t)$, $\vec{r}'_0$ and $\vec{r}''$ (See Fig. 2.4), it could be shown that the direction of $\tilde{\mathbf{M}}$ can be obtained by $\vec{r}_0' \times (\vec{r}' + \delta\vec{r}')$, which is denoted as vector $\vec{t}$:

$$\vec{t} = [r_{02}'(r_3' + \delta r_3') - r_{03}'(r_2' + \delta r_2')]\vec{i} + [r_{03}'(r_1' + \delta r_1') - r_{01}'(r_3' + \delta r_3')]\vec{j} + [r_{01}'(r_2' + \delta r_2') - r_{02}'(r_1' + \delta r_1')]\vec{k} \tag{A.7}$$

where $\vec{i}$, $\vec{j}$, $\vec{k}$ represent the unit vector in x, y, and z direction. And, assuming $|\vec{t}| = |\vec{r}_0'||\vec{r}'+\delta\vec{r}'|\sin\theta = \sin\theta$, hence

$$\frac{1}{|\vec{t}|} = \left[1-(\vec{r}'\cdot\vec{r}_0'+r_{01}'\delta r_1'+r_{02}'\delta r_2'+r_{03}'\delta r_3')^2\right]^{-1/2} = \frac{1}{\sqrt{1-(\vec{r}'\cdot\vec{r}_0')^2}\left[1-\frac{2\vec{r}'\cdot\vec{r}_0'}{1-(\vec{r}'\cdot\vec{r}_0')^2}(r_{01}'\delta r_1'+r_{02}'\delta r_2'+r_{03}'\delta r_3')\right]^{\frac{1}{2}}}$$

(A.8)

The higher order terms, $O(\delta r'^2)$, are discarded. Based on the approximation $(1+x)^{-\frac{1}{2}} \cong 1-\frac{1}{2}x$ when $x << 1$. Equation (2.51) is simplified to

$$\frac{1}{|t|} = \frac{1}{\sqrt{1-(\vec{r}'\cdot\vec{r}_0')^2}}\left[1+\frac{\vec{r}'\cdot\vec{r}_0'}{1-(\vec{r}'\cdot\vec{r}_0')^2}(r_{01}'\delta r_1'+r_{02}'\delta r_2'+r_{03}'\delta r_3')\right] \qquad \text{(A.9)}$$

So the moment in x direction could be derived as the following:

$$M_x = M_0\theta\frac{r_{02}'(r_3'+\delta r_3')-r_{03}'(r_2'+\delta r_2')}{|\vec{t}|} = M_{x0}+P_1\delta r_1'+P_2\delta r_2'+P_3\delta r_3' \qquad \text{(A.10)}$$

where $M_{x0} = M_0\theta_0\cos\alpha_1$, $P_1 = M_0[\theta_0 A_1 - \cos\alpha_1 R_1]$, $P_2 = M_0[\theta_0 A_2 - \cos\alpha_1 R_2]$, and $P_3 = M_0[\theta_0 A_3 - \cos\alpha_1 R_3]$. In these expressions,

$$\cos\alpha_1 = \frac{r_{02}'r_3'-r_{03}'r_2'}{\sqrt{1-(r'\cdot r_0')^2}},$$

$$A_1 = \frac{(r_{02}'r_3'-r_{03}'r_2')(\vec{r}'\cdot\vec{r}_0')}{\left[1-(\vec{r}'\cdot\vec{r}_0')^2\right]^{\frac{3}{2}}}r_{01}',$$

$$A_2 = \frac{(r_{02}'r_3'-r_{03}'r_2')(\vec{r}'\cdot\vec{r}_0')}{\left[1-(\vec{r}'\cdot\vec{r}_0')^2\right]^{\frac{3}{2}}}r_{02}'-\frac{r_{03}'}{\sqrt{1-(\vec{r}'\cdot\vec{r}_0')^2}},$$

$$A_3 = \frac{(r_{02}'r_3'-r_{03}'r_2')(\vec{r}'\cdot\vec{r}_0')}{\left[1-(\vec{r}'\cdot\vec{r}_0')^2\right]^{\frac{3}{2}}}r_{03}'+\frac{r_{02}'}{\sqrt{1-(\vec{r}'\cdot\vec{r}_0')^2}}$$

Following the same procedure,

$$M_y = M_0\theta \frac{r_{03}'(r_1'+\delta r_1') - r_{01}'(r_3'+\delta r_3')}{|\vec{t}|} = M_{y0} + Q_1\delta r_1' + Q_2\delta r_2' + Q_3\delta r_3' \qquad \text{(A.11)}$$

where $M_{y0} = M_0\theta_0\cos\alpha_2$, $Q_1 = M_0[\theta_0 B_1 - \cos\alpha_2 R_1]$, $Q_2 = M_0[\theta_0 B_2 - \cos\alpha_2 R_2]$, and $Q_3 = M_0[\theta_0 B_3 - \cos\alpha_2 R_3]$. In these expressions,

$$\cos\alpha_2 = \frac{r_{03}'r_1' - r_{01}'r_3'}{\sqrt{1-(\vec{r}'\cdot\vec{r}_0')^2}},$$

$$B_1 = \frac{(r_{03}'r_1' - r_{01}'r_3')(\vec{r}'\cdot\vec{r}_0')}{\left[1-(\vec{r}'\cdot\vec{r}_0')^2\right]^{\frac{3}{2}}} r_{01}' + \frac{r_{03}'}{\sqrt{1-(\vec{r}'\cdot\vec{r}_0')^2}},$$

$$B_2 = \frac{(r_{03}'r_1' - r_{01}'r_3')(\vec{r}'\cdot\vec{r}_0')}{\left[1-(\vec{r}'\cdot\vec{r}_0')^2\right]^{\frac{3}{2}}} r_{02}',$$

$$B_3 = \frac{(r_{03}'r_1' - r_{01}'r_3')(\vec{\boldsymbol{r}}'\cdot\vec{\boldsymbol{r}}_0')}{\left[1-(\vec{\boldsymbol{r}}'\cdot\vec{\boldsymbol{r}}_0')^2\right]^{\frac{3}{2}}} r_{03}' - \frac{r_{01}'}{\sqrt{1-(\vec{\boldsymbol{r}}'\cdot\vec{\boldsymbol{r}}_0')^2}}$$

The moment in z direction:

$$M_z = M_0\theta \frac{r_{01}'(r_2'+\delta r_2') - r_{02}'(r_1'+\delta r_1')}{|\vec{t}|} = M_{z0} + T_1\delta r_1' + T_2\delta r_2' + T_3\delta r_3' \qquad \text{(A.12)}$$

where $M_{Z0} = M_0\theta_0\cos\alpha_3$, $T_1 = M_0[\theta_0 C_1 - \cos\alpha_3 R_1]$, $T_2 = M_0[\theta_0 C_2 - \cos\alpha_3 R_2]$, and $T_3 = M_0[\theta_0 C_3 - \cos\alpha_3 R_3]$. In these expressions,

$$\cos\alpha_3 = \frac{r_{01}'r_2' - r_{02}'r_1'}{\sqrt{1-(\vec{\boldsymbol{r}}'\cdot\vec{\boldsymbol{r}}_0')^2}},$$

$$C_1 = \frac{(r_{01}'r_2' - r_{02}'r_1')(\vec{\boldsymbol{r}}'\cdot\vec{\boldsymbol{r}}_0')}{\left[1-(\vec{\boldsymbol{r}}'\cdot\vec{\boldsymbol{r}}_0')^2\right]^{\frac{3}{2}}} r_{01}' - \frac{r_{02}'}{\sqrt{1-(\vec{\boldsymbol{r}}'\cdot\vec{\boldsymbol{r}}_0')^2}},$$

$$C_2 = \frac{(r_{01}'r_2' - r_{02}'r_1')(\vec{\boldsymbol{r}}'\cdot\vec{\boldsymbol{r}}_0')}{\left[1-(\vec{\boldsymbol{r}}'\cdot\vec{\boldsymbol{r}}_0')^2\right]^{\frac{3}{2}}} r_{02}' + \frac{r_{01}'}{\sqrt{1-(\vec{\boldsymbol{r}}'\cdot\vec{\boldsymbol{r}}_0')^2}},$$

$$C_3 = \frac{(r_{01} r_2' - r_{02}' r_1')(\vec{\boldsymbol{r}}'\cdot\vec{\boldsymbol{r}}_{\boldsymbol{0}}')}{\left[1-(\vec{\boldsymbol{r}}'\cdot\vec{\boldsymbol{r}}_{\boldsymbol{0}}')^2\right]^{\frac{3}{2}}}\, r_{03}'$$

Thus the total moment $\tilde{\mathbf{M}} = (M_x, M_y, M_z)$ is obtained.

After Galerkin Method is used to get a series of ordinary differential equations, the generalized force is calculated by,

$$\mathbf{f}_2 = -\frac{1}{L}B\mathbf{r}''(0) = \frac{1}{L}(\boldsymbol{r}'+\delta\boldsymbol{r}')\times\tilde{\mathbf{M}}(0) \tag{A.13}$$

At the upper end of SCR, $\mathbf{f}_2$ represents the moment exerted by the flex joint on the riser at the porch. Substituting the expression for $\boldsymbol{r}'+\delta\boldsymbol{r}'$ and (M_x, M_y, M_z), the expressions for f_{21}, f_{22}, f_{23} could be obtained. Adding this boundary conditions to the global system of equations **A**δ**X**=**B,** the analysis considering the effects of flex joint could be performed.

$$\begin{aligned} f_{21} &= \frac{1}{L}(M_{z0} r_2' - M_{y0} r_3') \\ &+ \frac{1}{L}\left(T_1 r_2' - Q_1 r_3'\right)\delta r_1' + \frac{1}{L}\left(T_2 r_2' - Q_2 r_3' + M_{z0}\right)\delta r_2' + \frac{1}{L}(T_3 r_2' - Q_3 r_3' - M_{y0})\delta r_3' \end{aligned} \tag{A.14}$$

$$\begin{aligned} f_{22} &= \frac{1}{L}(M_{x0} r_3' - M_{z0} r_1') \\ &+ \frac{1}{L}\left(P_1 r_3' - T_1 r_1' - M_{z0}\right)\delta r_1' + \frac{1}{L}\left(P_2 r_3' - T_2 r_1'\right)\delta r_2' + \frac{1}{L}(P_3 r_3' - T_3 r_1' + M_{x0})\delta r_3' \end{aligned} \tag{A.15}$$

$$\begin{aligned} f_{23} &= \frac{1}{L}(M_{y0} r_1' - M_{x0} r_2') \\ &+ \frac{1}{L}\left(Q_1 r_1' - P_1 r_2' + M_{y0}\right)\delta r_1' + \frac{1}{L}\left(Q_2 r_1' - P_2 r_2' - M_{x0}\right)\delta r_2' + \frac{1}{L}(Q_3 r_1' - P_3 r_2')\delta r_3' \end{aligned} \tag{A.16}$$

Add the first term of f_{21}, f_{22}, f_{23} onto the right hand side of vector **B,** while other terms are moved to the left hand side of the global system of equation. Necessary changes are to be made on corresponding entries of left matrix **A.**